NORTHWESTERN UNIVERSITY

Fluid-Structure Interaction

A DISSERTATION

SUBMITTED TO THE GRADUATE SCHOOL
IN PARTIAL FULFILLMENT OF THE REQUIREMENTS

for the degree

DOCTOR OF PHILOSOPHY

Field of Mechanical Engineering

By

Hongwu Wang

EVANSTON, ILLINOIS

June 2007

© Copyright by Hongwu Wang 2007

All Rights Reserved

Abstract

Fluid-Structure Interaction

Hongwu Wang

Spectral elements are p-type element which can provide better accuracy and faster convergence. However, applications of these elements make conformation to discontinuities in the function or its derivative difficult. The eXtended Finite Element Method (XFEM) recently developed at Northwestern University can easily treat the arbitrarily aligned discontinuities, i.e. independent of the mesh, for both the function and its derivative. A spectral finite element with arbitrary discontinuities is developed. We show an optimal convergence rate of the spectral element for straight discontinuities and slightly suboptimal convergence rate for curved discontinuity in the energy norm error.

A variational principle is developed for fluid-structure interaction of bodies. The variational principle is applicable to models where the fluid is described by Eulerian coordinates while the solid is described by Lagrangian coordinates, which suits their intrinsic characteristics. The momentum equation and the coupling are unified in one weak form. This weak form is in accord with the standard Finite Element Method (FEM) and is easy to implement. The method enables the fluid and solid meshes to be arbitrary and there is no

limit on the extent of the deformation of the solid. Although a compressible viscous fluid formulation is implemented here, the method can be extended to incompressible fluids. Both explicit and implicit time integration can be used with this method.

The constraint method for fluid-structure interaction is further developed. As for the variationally consistent method for the fluid-structure interaction problem, the meshes for the fluid and solid are independent. Eulerian coordinates are used for the fluid and Lagrangian coordinates for the solid. The coupling is furnished through the enforcement of the continuity equation on the interface by a constraint method. The momentum balance on the interface is supplied by the weak form. The interface integration required by the coupling is regularized by a window function. This avoids the awkward line integration in 2D and surface integration in 3D.

Acknowledgements

I would like to first express my sincere gratitude to my advisor Professor Ted Belytschko for his guidance, support, encouragement and inspiration in research during my graduate studies in the Department of Mechanical Engineering at Northwestern University. It has been a great and fruitful experience to work with him. I would also like to thank Professors Brian Moran and David Chopp who serve as members of my qualifying and defense committees, and their instructions.

I have had a lot of interesting discussions and gotten a lot of help from my current and former colleagues, Dr. Jack Chessa, Dr. Antoine Legay, Dr. Shaoping Xiao, Dr. Sulin Zhang, Dr. Pedro Areias, Dr. Hao Chen, Dr. Jingxiao Xu, Dr. Samaniego, Dr. Chandu Parimi, Jeong-Hoon Song, Robert Gracie, Roopam Khare. Many thanks to them.

Finally I would like to thank my parents, Qingsen and Guixian, and my wife Lingyun for their consistent support and love. They have shared all the bad and good times together with me in my life.

Contents

Abstract 3

Acknowledgements 5

List of Figures 8

List of Tables 13

Chapter 1. Introduction 14

Chapter 2. Strong and Weak Arbitrary Discontinuities In Spectral Finite Elements 17

2.1. INTRODUCTION 17

2.2. METHODOLOGY 19

2.3. GALERKIN WEAK FORM 26

2.4. NUMERICAL RESULTS 34

2.5. CONCLUSIONS 44

Chapter 3. A Variationally Consistent Immersed Element Method For Fluid-Structure Interaction 46

3.1. INTRODUCTION 46

3.2. NOTATION 48

3.3. FLUID SOLVER 50

3.4. GOVERNING EQUATIONS 56

3.5. FORMULATION OF THE FLUID-STRUCTURE INTERACTION PROBLEM 57

Chapter 4. Fluid-Structure Interaction By The Constraint Method 67

4.1. INTRODUCTION 67

4.2. WEAK FORM 74

4.3. DISCRETIZATION 76

Chapter 5. Comparisons And Numerical Examples 86

5.1. SOLID OBSTACLE IN THE FLUID CHANNEL 86

5.2. SOFT SOLID IN THE FLUID CHANNEL 94

5.3. FALLING BALL IN FLUID 98

Chapter 6. Conclusions 104

Appendix . Solving Parent Coordinates In An Element From The Physical Coordinates For A Node 105

Bibliography 107

Appendix. Bibliography 107

List of Figures

2.1 Domains with a discontinuity Γ_D surrounded by a local partition of unity domain Ω_{LPU} and a blending domain Ω_B. 20

2.2 Implicit function description of discontinuities for the two cases in Figure 2.1. 21

2.3 Spectral mesh for local partition of unity showing elements in Ω_{LPU} and Ω_B, the enriched elements and blending elements, respectively. A structured mesh is shown but the application to unstructured meshes is similar. 22

2.4 Nodes in the third order spectral element and node repartition. 29

2.5 Integration of a third order enriched spectral element by rectilinear triangular sub-domains; $\circ$ denotes the quadrature points. 30

2.6 Element subdivision and quadrature points for the 6-node quadratic and 10-node cubic triangles. 32

2.7 Element subdivision and quadrature points for the 3rd order spectral element mesh around a circular inclusion. $*$ denotes the nodes for spectral elements; $\circ$ denotes the quadrature points; $\blacksquare$ denotes the nodes for 6-node triangles. 33

2.8	Integration points in quadrilaterals for triangles; ∘ denotes the quadrature points.	34
2.9	Tangential discontinuities.	35
2.10	Displacement mode corresponding to the lowest eigenvalue; * denotes the nodes of the spectral element.	36
2.11	Bi-material plate problem with mesh.	37
2.12	Convergence of the error in energy norm for bi-material plate problem; cr = rate of convergence, std = standard.	38
2.13	Convergence of the error in energy norm for manufactured bimaterial problem with discontinuity (a) not coincident with element edges and (b) coincident with element edges; cr=rate of convergence; no enrichment is used here.	40
2.14	Convergence of the error in energy norm for manufactured bimaterial problem with XFEM; cr=rate of convergence.	41
2.15	Convergence rates of energy norm error for circular inclusion problem with the rectilinear triangular subdomains for quadrature; cr=rate of convergence, std=standard.	42
2.16	Convergence rates of energy norm error for circular inclusion problem with curved 6-node triangular subdomains for quadrature; cr=rate of convergence, std=standard.	43
3.1	Fluid solid system with solid domain Ω^{S} and fluid domain Ω^{F}.	49

3.2 Conceptual depiction of the model: energetically, the total system consists of $\delta W^{\mathrm{F}} + \delta W^{\mathrm{S}} - \delta W^{\mathrm{FS}}$. 60

3.3 Example of a solid in a structured fluid mesh showing that only that portion of some elements that contribute to integrals of the form $\int_\Omega H(\phi) f(\boldsymbol{x}) \, \mathrm{d}\Omega$. 64

4.1 Curve integration in 2D. 74

4.2 Cubic spline functions for the regularization of the Dirac delta function. 77

4.3 Regularized Dirac delta function. 82

4.4 Adaptive quadrature for a fluid element 85

5.1 Solid obstacle in the fluid channel. 86

5.2 Prescribed pressure on the left end of the fluid channel for the solid obstacle problem. 87

5.3 A typical mesh m1 for the solid obstacle problem. 88

5.4 Snapshots of pressure contours and deformations for the solid obstacle problem. 89

5.5 Snapshots of the velocities for the fluid and solid in the solid obstacle problem. 90

5.6 Snapshots of the velocities for the fluid and solid in the solid obstacle problem. 90

5.7 Snapshots of the velocities for the fluid and solid in the solid obstacle problem. 91

5.8 Velocity and displacement evolutions for nodes A and B in the solid obstacle problem by the immersed element method (lumped mass used). 92

5.9 Velocity and displacement evolutions for nodes A and B in the solid obstacle problem by the immersed element method (consistent mass used). 93

5.10 Velocity and displacement evolutions for nodes A and B in the solid obstacle problem by the constraint Lagrange multiplier method. 94

5.11 Comparisons of velocity and displacement time histories for nodes A and B in the solid obstacle problem by the immersed element lumped mass method (denoted as "Var-Con-Lump"), the immersed element consistent mass method (denoted as "Var-Con-Consis") and the Lagrange multiplier method (denoted as "Lag-Mul"),. 95

5.12 Solid floating in the fluid. 96

5.13 Snapshots of pressure and deformation for the floating solid problem. 98

5.14 Velocities of nodes A and B by mesh ms2 for the floating solid problem by the consistent and lumped mass immersed element method and the Lagrange multiplier method. 99

5.15 Velocities of nodes A and B by the consistent mass immersed element method for meshes ms1 and ms2 for the floating solid problem. 99

5.16 Velocities of nodes A and B by lumped mass immersed element method for meshes ms1 and ms2 for the floating solid problem. 100

5.17 Velocities of nodes A and B by the Lagrange multiplier method for meshes ms1 and ms2 for the floating solid problem. 100

5.18 Problem setup for the freely falling ball problem. 101

5.19 Numerical results for the falling ball problem. 102

5.20 Velocity of falling ball; "exact" is the exact terminal velocity. 103

List of Tables

2.1	Condition numbers for the stiffness matrix of the circular inclusion problem.	44
4.1	Switches for choice of constraint method.	68
5.1	Meshes used for the solid obstacle problem.	88
5.2	Meshes used for the floating solid problem.	97
5.3	Mesh used for the falling ball problem.	102

CHAPTER 1

Introduction

In chapter 2, methods for constructing arbitrary discontinuities within spectral finite elements are described and studied. We use the concept of the eXtended Finite Element Method (XFEM), which introduces the discontinuity through a local partition of unity, so there is no requirement for the mesh to be aligned with the discontinuities. A key aspect of the implementation of this method is the treatment of the blending elements adjacent to the local partition of unity. We found that a partition constructed from spectral functions one order lower than the continuous approximation is optimal and no special treatment is needed for higher order elements. For the quadrature of the Galerkin weak form, since the integrand is discontinuous, we use a strategy of subdividing the discontinuous elements into 6-node and 10-node triangles; the order of the element depends on the order of the spectral method for curved discontinuities. Several numerical examples are solved to examine the accuracy of the methods. For straight discontinuities, we achieved the optimal convergence rate of the spectral element. For the curved discontinuity, the convergence rate in the energy norm error is suboptimal. We attribute the sub-optimality to the approximations in the quadrature scheme. We also found that modification of the adjacent elements is only needed for lower order spectral elements.

For the fluid-structure interaction problem, there are basically two approaches we have taken to the coupling. They are

(1) the variationally consistent immersed element method which gives a uniform weak form for the coupling and the momentum equation.
(2) the constraint method which enforces the continuity condition along the interface by a constraint method.

In Chapter 3, the variationally consistent immersed element method is developed and in Chapter 4, the constraint method is further developed. Both of the methods share these common features

(1) the fluid is described by Eulerian coordinates while the solid is described by Lagrangian coordinates.
(2) the fluid and solid meshes are arbitrarily aligned.
(3) there is no limit on the extent of the deformation of the solid.
(4) both explicit and implicit time integration can be used.
(5) both compressible and incompressible fluids can be used.
(6) the solution procedure for the coupling is concurrent instead of sequential, i.e. no transformations of physical variables between the fluid and solid.
(7) both of the methods are equivalent to the strong form.

However, the two methods demonstrate distinct aspects in consideration of the coupling between the fluid and solid.

(1) in the variationally consistent immersed element method, the continuity condition is implicit in the weak form, i.e. a uniform velocity field is provided.
(2) in the constraint method, the continuity condition is explicitly supplied by the constraint method.

(3) by using Lagrange multipliers, the constraint method augments system unknowns which may become costly in computation.

(4) lumped mass can be used for the variationally consistent immersed element method.

(5) a line integration in 2D and a surface integration in 3D along the interface are necessary for the constraint method.

In Chapter 5, some numerical examples are presented for both methods. The variationally consistent immersed element method is implemented by both the lumped and consistent mass. Comparisons between them are displayed. Finally, the conclusions are drawn in Chapter 6.

CHAPTER 2

Strong and Weak Arbitrary Discontinuities In Spectral Finite Elements

2.1. INTRODUCTION

Spectral elements offer substantial accuracy advantages over conventional elements for smooth problems. However, for problems with interior discontinuities in the functions or their gradients that arise, for example, from discontinuous changes in the coefficients of the partial differential equation, spectral elements can become quite awkward. Discontinuities in the function arise between unlinked subdomains, such as the surfaces of a crack. Generally, such discontinuities are treated in finite element methods by aligning the element interfaces with the discontinuity. However, when the interface between the subdomains with different coefficients in the partial differential equation is curved, it would be necessary to use curved spectral elements, which degrades their accuracy. Furthermore for the modeling of thin layers of materials in solid mechanics problems, conforming the mesh to the discontinuities entails the use of small spectral elements, which is often awkward. The difficulties are compounded for moving interface problems, where the approach of making element interfaces coincident with the discontinuity requires continuous remeshing.

Therefore, it is quite desirable to have techniques for modeling discontinuities in functions and their gradients that are not coincident with element interfaces by allowing them

within an element. Such techniques have already been developed for standard finite elements by Moes et al [**69**] and Belytschko et al [**13**] based on the earlier work by Belytschko and Black [**6**], but their studies were limited to low order elements; the method was called the extended finite element method (XFEM) [**25, 7, 86**]. The method is based on a local partition of unity, which is an extension of the partition of unity methods proposed by Babuska et al [**2**], Babuska and Melenk [**68, 3**] and Duarte and Oden [**38**]; a study of local partitions of unity is reported in Chessa et al [**26**]. It is shown here that the application of these techniques to higher order elements requires some additional considerations, such as improved quadrature methods of the Galerkin weak form and careful design of the elements adjacent to the local partition of unity. Remarkably, with the methods given here, one can develop methods for constructing higher order elements with interior function discontinuities or gradient discontinuities that almost maintain the optimal convergence properties.

We will see that the modeling of discontinuities in functions is substantially simpler than the modeling of discontinuities in gradients. For the treatment of discontinuities in the functions themselves, there is no need for special treatment of the domain adjacent to the local partition of unity, called the blending domain. On the other hand, for discontinuities in the gradients, a blending partition must be constructed in the blending domain from functions at least one order lower than those used for the basic approximation. Since a blending approximation that is one order lower cannot be constructed for linear and bilinear elements, these elements require a special treatment in the blending subdomain to eliminate extraneous functions. This situation for low order elements has already been treated by Chessa et al [**26**] where special enhanced blending element were developed. The

interesting finding here is that enhanced blending elements are unnecessary for higher order elements for rectilinear discontinuities and that the blending partition for order p elements should be constructed from order $p-1$ spectral functions for optimal accuracy.

In the following, we will describe these methods in the context of the Poisson equation and linear elasticity, but the methods are applicable to any partial differential equations, including nonlinear partial differential equations. We will formulate the methods in terms of implicit functions, i.e. level sets, but this specialization is not necessary. The level set approach simplifies the notation and provides benefits in implementation since it enables the location of the discontinuity to be described entirely in terms of nodal data.

The method is here formulated in the context of level sets. XFEM was first combined with level sets to treat cracks by Stolarska et al [**84**], Belytschko et al [**13**], Chessa et al [**23, 24**], Ji, Chopp and Dolbow [**57**] and Chopp et al [**27**].

In the next Section, we describe the approximations for discontinuous functions and functions with discontinuous gradients. In Section 3, we describe the Galerkin weak form and its discretization, with particular emphasis on the quadrature issues that are unique to this method. Some implementation issues are also remarked upon. In Section 4, results are given for a variety of problems where closed form solutions or information about the solution is available, which enables us to judge the accuracy of the method. Section 5 discusses this approach and gives some conclusions.

2.2. METHODOLOGY

Consider a domain Ω with boundary Γ and a discontinuity on a surface (a line in two dimensions) Γ_D as shown in Figure 2.1. For clarity, we consider a single discontinuity but

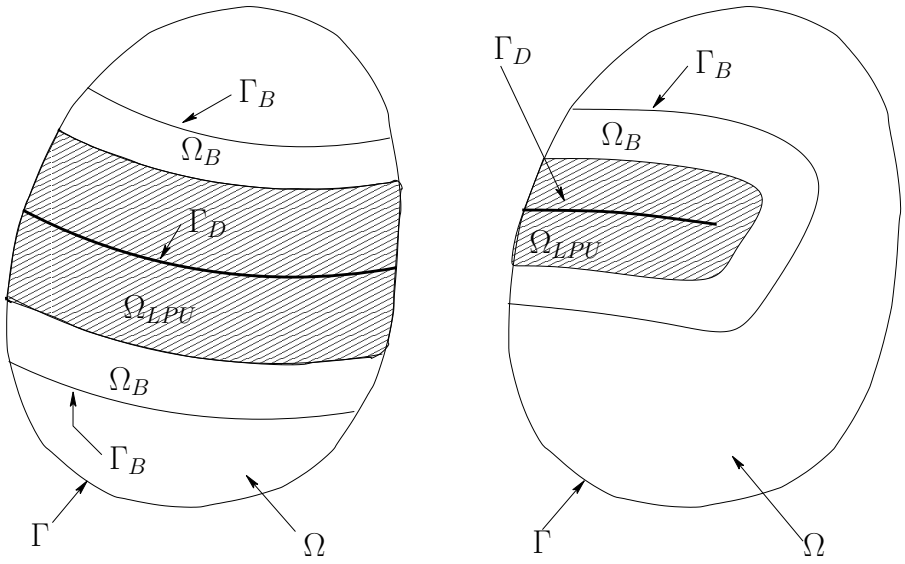

(a) A domain cut by the discontinuity.

(b) A discontinuity that ends in the domain.

Figure 2.1. Domains with a discontinuity Γ_D surrounded by a local partition of unity domain Ω_{LPU} and a blending domain Ω_B.

the method is also applicable to multiple discontinuities. The discontinuity may be either in the function or its gradient. In Figure 2.1, we have shown two cases:

(1) where the discontinuity bisects the domain Ω.

(2) where the discontinuity ends within the domain.

The former could be the interface between two materials, the latter a crack. Around the discontinuity, we define a domain Ω_{LPU}, which we call the local partition of unity domain; adjacent to that domain are blending partition domains Ω_B.

We define the location of the discontinuity Γ_D implicitly by

$$\forall \mathbf{x} \in \Omega \mid f(\mathbf{x}) = 0 \tag{2.1}$$

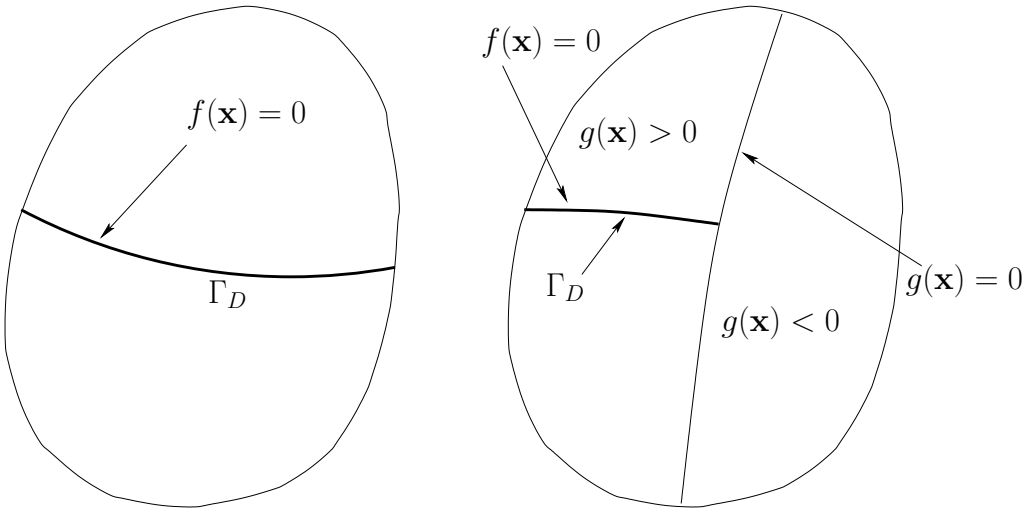

(a) A domain cut by the discontinuity.

(b) A discontinuity that ends in the domain.

Figure 2.2. Implicit function description of discontinuities for the two cases in Figure 2.1.

For the case where the discontinuity ends within the domain, we define the location by constructing another function $g(\mathbf{x})$ such that $g(\mathbf{x}) > 0$ in the subdomain cut by Γ_D as shown in Figure 2.2(b). The location of the discontinuity is then given by

$$\forall \mathbf{x} \in \Omega \mid f(\mathbf{x}) = 0 \ \wedge \ g(\mathbf{x}) > 0 \tag{2.2}$$

On the domain Ω_{LPU} we construct a local partition of unity, Babuska and Melenk [**3**], Chessa et al [**26**]. The domain $\Omega_{LPU} \cup \Omega_B$ is covered by overlapping subdomains Ω_I and a set of functions ϕ_I is selected so that the supports of ϕ_I correspond to Ω_I. These functions are required to satisfy

$$\sum \phi_I = 1 \quad \text{in} \quad \Omega_{LPU} \tag{2.3}$$

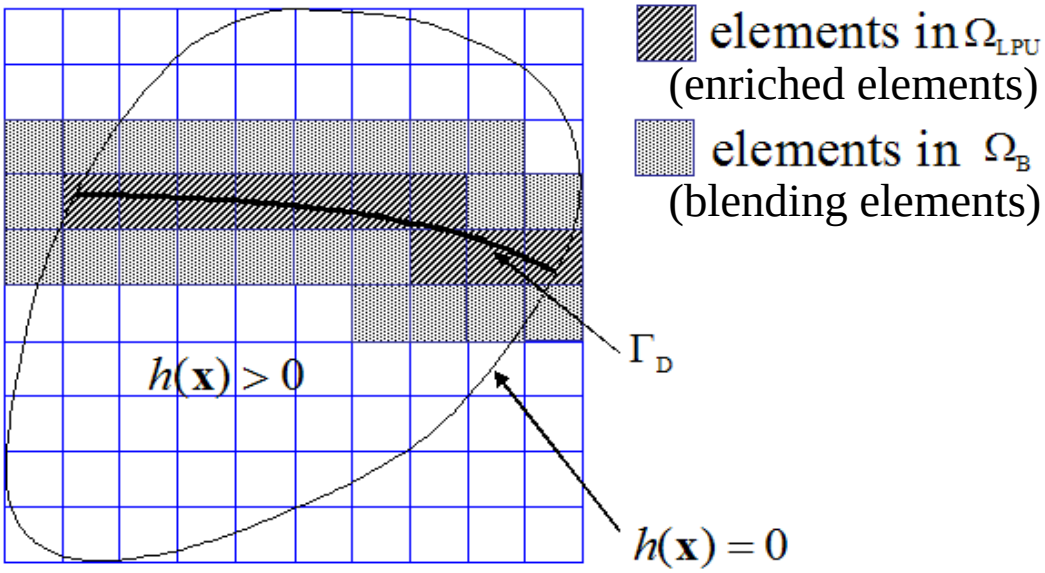

Figure 2.3. Spectral mesh for local partition of unity showing elements in Ω_{LPU} and Ω_B, the enriched elements and blending elements, respectively. A structured mesh is shown but the application to unstructured meshes is similar.

$$\sum \phi_I = 0 \quad \text{on} \quad \Gamma_B \tag{2.4}$$

The construction of the discontinuous approximation for $u(\mathbf{x})$ is based on an additive decomposition of the function into its continuous and discontinuous parts

$$u(\mathbf{x}) = u^{cont}(\mathbf{x}) + u^{disc}(\mathbf{x}) \tag{2.5}$$

We have chosen to illustrate the procedure first for a scalar function; in some cases, we generalize the results to vector functions.

To develop the spectral element approximation, the domain Ω is subdivided into elements Ω^e, as shown in Figure 2.3. Figure 2.3 shows a Cartesian mesh, but the concept applies equally to unstructured meshes; the outside boundary is defined by $h(\mathbf{x}) = 0$, the interior by $h(\mathbf{x}) > 0$. The local partition of unity is then constructed from the shape functions $N_I(\mathbf{x})$. The choice of the domain Ω_{LPU} is governed by the location of the discontinuity; all elements that are crossed by the discontinuity must be in Ω_{LPU}. The selection of Ω_B is then dictated by the fact that the functions ϕ_I vanish on Γ_B, (2.4). Moreover, it is advantageous to make Ω_B as small as possible. For an element shape function partition, these conditions are met by including all elements that are crossed by the discontinuity in Ω_{LPU}; Γ_B is then the boundary of the next layer of elements.

Let the set of nodes in the model be $\mathbb{S}$ and the subset of $\mathbb{S}$ of nodes in Ω_{LPU} be $\mathbb{S}_P$. We now approximate the continuous part of $u(\mathbf{x})$ by the standard spectral shape functions and the discontinuous part by the local partition of unity

$$u(\mathbf{x}) = \sum_{I \in \mathbb{S}} N_I^P(\mathbf{x}) u_I + \sum_{I \in \mathbb{S}_P} \phi_I(\mathbf{x}) \psi(\mathbf{x}) q_I \tag{2.6}$$

where $N_I^P(\mathbf{x})$ are the spectral shape functions of order p, u_I are the nodal values, $\psi(\mathbf{x})$ is an enrichment function, and q_I are additional parameters. We will next describe how we construct the enrichment separately for discontinuous functions and discontinuous gradients. In both cases, we let the partition of unity functions be the spectral shape functions; the domains Ω_I therefore correspond to the union of the elements that share node I.

2.2.1. Gradient discontinuity

The enrichment for a gradient discontinuity that cuts the entire domain is given by

$$u(\mathbf{x}) = \sum_{I \in \mathbb{S}} N_I^P(\mathbf{x}) u_I + \sum_{I \in \mathbb{S}_P} N_I^{P-1}(\mathbf{x}) \left(|f(\mathbf{x})| - |f(\mathbf{x}_I)| \right) q_I \tag{2.7}$$

The construction of the enrichment in terms of $N^{P-1}(\mathbf{x})$, i.e. spectral functions one order lower than those used for the continuous approximation, is crucial in achieving optimal convergence. This is an extension of an enrichment proposed in Belytschko et al [**13**] and Sukumar et al [**85**]. Approaches of this type were previously proposed for meshless methods by Krongauz and Belytschko [**59**].

2.2.2. Discontinuity in function

We next consider strong discontinuities [**47**] for vector functions. To approximate a discontinuity in a function for a discontinuity that cuts the domain completely, as in Figure 2.1(a), we let

$$\psi(\mathbf{x}) = H\left(f\left(\mathbf{x}\right)\right) \tag{2.8}$$

where $H(\bullet)$ is the Heaviside step function. For a partial cut, such as shown in Figure 2.1(b), we let

$$\psi(\mathbf{x}) = \sin\left(\frac{\theta}{2}\right) H\left(f\left(\mathbf{x}\right)\right) H\left(g\left(\mathbf{x}\right)\right) \tag{2.9}$$

$$\theta = \tan^{-1} \frac{f}{\sqrt{f^2 + g^2}} \tag{2.10}$$

The approximation is then given by

$$\mathbf{u}(\mathbf{x}) = \sum_{I \in \mathbb{S}} N_I^P(\mathbf{x})\mathbf{u}_I + \sum_{I \in \mathbb{S}_P} N_I^1(\mathbf{x}) \left(\psi(\mathbf{x}) - \psi(\mathbf{x}_I)\right) \mathbf{q}_I \tag{2.11}$$

where $\psi(\mathbf{x})$ is given by (2.8) or (2.9). Note that we use the first order (bilinear or linear) shape functions for the enrichment for function discontinuities.

For tangential discontinuities, we use [**13**]

$$\mathbf{u}(\mathbf{x}) = \sum_{I \in \mathbb{S}} N_I^P(\mathbf{x})\mathbf{u}_I + \sum_{I \in \mathbb{S}_P} \mathbf{e}_t(\mathbf{x}) N_I^1(\mathbf{x}) \left(H(f(\mathbf{x})) - H(f(\mathbf{x}_I))\right) q_I \tag{2.12}$$

where $\mathbf{e}_t$ is a vector in the tangential direction. Note that the above enrichment function (the second term) automatically vanishes in the blending elements since $H(f(\mathbf{x}))$ is constant in the blending elements. The gradient ∇f provides the normal direction as

$$\mathbf{e}_n = \frac{\nabla f}{\|\nabla f\|} \tag{2.13}$$

the tangent plane is then defined by any two unit vectors orthogonal to $\mathbf{e}_n$. In two dimensions, we have $\mathbf{e}_t = \mathbf{e}_z \times \mathbf{e}_n$.

Remark: As noted in [**13**], we subtract $\psi(\mathbf{x}_I)$ from $\psi(\mathbf{x})$ in (2.11) so that implementation is easier; in this way, $\mathbf{u}(\mathbf{x}_I) = \mathbf{u}_I$ which simplifies the imposition of essential boundary conditions. Furthermore, the step function enrichment then vanishes in elements not cut by the discontinuity.

Remark: We can use several functions to improve the enrichment around the end of the discontinuity, i.e. we can use

$$\mathbf{u}^{disc}(\mathbf{x}) = \sum_{I \in \mathbb{S}_P} \sum_{\alpha} N_I(\mathbf{x}) \psi_\alpha(\mathbf{x}) \mathbf{q}_{\alpha I} \tag{2.14}$$

$$[\psi_\alpha] = \sin\left(\frac{\theta}{2}\right) \left(H\left(f(\mathbf{x})\right) H\left(g(\mathbf{x})\right) - H\left(f(\mathbf{x}_I)\right) H\left(g(\mathbf{x}_I)\right)\right) [r \quad r^2 \quad r^3] \tag{2.15}$$

$$r^2 = f^2 + g^2 \tag{2.16}$$

Remark: Approximations for intersecting and branching discontinuities can be constructed in the same way by adding additional functions as described for low order elements by Belytschko et al [**13**] and Daux et al [**34**].

2.3. GALERKIN WEAK FORM

In most cases, we will consider the Poisson equation in domain Ω with boundary Γ.

$$\nabla\left(k\left(\mathbf{x}\right)\nabla u\right) + b = 0$$

$$\text{with } u = \bar{u} \text{ on } \Gamma_u, \quad k(\mathbf{x})\mathbf{n} \cdot \nabla u = \bar{g} \text{ on } \Gamma_g, \quad \Gamma_u \cup \Gamma_g = \Gamma \quad \Gamma_u \cap \Gamma_g = \emptyset \tag{2.17}$$

Note that $k(\mathbf{x})$ may be discontinuous. The weak form is

$$\text{for } u \in \mathbb{U}, \int_\Omega \nabla \delta u \; k(\mathbf{x}) \; \nabla u \; \mathrm{d}\Omega = \int_\Omega \delta u \; b \; \mathrm{d}\Omega + \int_{\Gamma_g} \delta u \; \bar{g} \; \mathrm{d}\Gamma \quad \forall \delta u \quad \in \mathbb{U}_0 \tag{2.18}$$

where $\mathbb{U}$ is the space of trial functions, $\mathbb{U} = \{u | u \in \mathbb{H}^1, \, u = \bar{u} \text{ on } \Gamma_u\}$; $\mathbb{U}_0$ is the space of test functions, $\mathbb{U}_0 = \{\delta u | \delta u \in \mathbb{H}^1, \, \delta u = 0 \text{ on } \Gamma_u\}$ with $\mathbb{H}^1$ denoting the Hilbert space. The introduction of enrichments with discontinuities introduces certain difficulties into

the quadrature of the weak form since the integrand on the left hand side is not continuous. Consider an element Ω^e that is cut by the line Γ^e where the gradient of $u(\mathbf{x})$ is discontinuous. If we define this line by an implicit function $f(\mathbf{x}) = 0$, then the integrand can be split into two subdomains within which the integrand is continuous, i.e.

$$\int_\Omega \nabla\delta u \; k(\mathbf{x}) \; \nabla u \;\; \mathrm{d}\Omega = \int_\Omega H\left(f(\mathbf{x})\right) \nabla\delta u \; k(\mathbf{x}) \; \nabla u \;\; \mathrm{d}\Omega + \int_\Omega H\left(-f(\mathbf{x})\right) \nabla\delta u \; k(\mathbf{x}) \; \nabla u \;\; \mathrm{d}\Omega \tag{2.19}$$

In our implementation we approximate $f(\mathbf{x})$ by the spectral interpolants of the same order as for $u(\mathbf{x})$, i.e.

$$f(\mathbf{x}) = \sum_{I \in \mathbb{S}} f_I N_I^P(\mathbf{x}) \tag{2.20}$$

The interpolation is only constructed in Ω_{LPU}.

2.3.1. Spectral approximation

We used the spectral elements [**50**] of Patera [**76**] with a formulation based on Karniadakis and Sherwin [**58**]. The element employs variably spaced nodes corresponding to the zeros of the Chebyshev or Legendre polynomials, called a Chebyshev-Gauss point repartition [**76**]. The P-th order Chebyshev polynomial is:

$$T_P(x) = \cos\left(P\theta\right) \quad \text{with} \quad \theta = \arccos\left(x\right) \quad \text{and} \quad x \in \left[\begin{array}{cc} -1 & 1 \end{array} \right] \tag{2.21}$$

Nodal coordinates in the element are chosen such that:

$$T_P'(x_I) = 0\,, \;\; I = 1,\, 2,\, \ldots,\, P-1 \;\text{ and } x_0 = -1\,, \;\; x_P = 1. \tag{2.22}$$

where the prime denotes differentiation with respect to the argument. One can then show that:

$$x_I = -\cos\frac{I\pi}{P}\,,\ I = 0, 1, 2, \ldots\ P \tag{2.23}$$

Note that this repartition of nodes allows us to write the shape functions in terms of Chebyshev polynomials [**21**]:

$$N_I^{1D}(x) = \frac{(-1)^{I+P}\ (x^2-1)\ T_P'(x)}{c_I\ P^2\ (x-x_I)} = \frac{2}{P}\sum_{J=0}^{P}\frac{1}{c_I c_J}T_J(x_I)T_J(x) \tag{2.24}$$

where $c_I = 2$ if I is 0 or P, $c_I = 1$ otherwise. In two dimensions, the same nodal distribution is taken in each direction. The following notation is used for node IJ:

$$\mathbf{x}_{IJ} = (x_I, y_J) = \left(-\cos\left(\frac{I\pi}{P}\right), -\cos\left(\frac{J\pi}{P}\right)\right) \tag{2.25}$$

where I and J vary from 0 to P. The shape functions are obtained by a tensor product of the one dimensional shape functions N_I^{1D}:

$$N_{IJ}(\mathbf{x}) = N_{IJ}(x, y) = N_I^{1D}(x)N_J^{1D}(y) \tag{2.26}$$

Figure 2.4 shows a 3rd order spectral element and its nodes.

2.3.2. Blending elements

The elements adjacent to the enriched elements, see Figure 2.3, have some nodes enriched and some nodes unenriched. We call them blending elements [**26**]. When the enrichment is activated for the discontinuous gradient enrichment, higher order terms appear in the blending elements which must be canceled by the continuous field. When $p = 1$, the

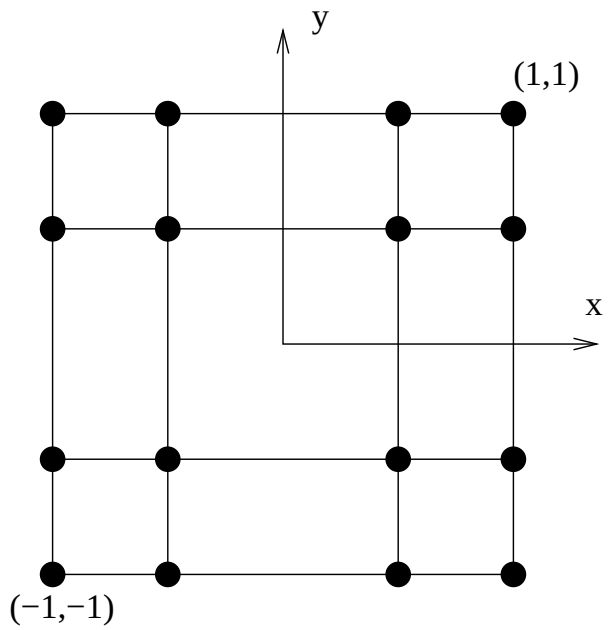

Figure 2.4. Nodes in the third order spectral element and node repartition.

blending element fields are not constant when the enrichment is activated. Consequently, the method then cannot exactly match solutions consisting of two constant gradient fields. We have found that this shortcoming drastically curtails the rate of convergence. To eliminate the effects of those enriched terms in the blending elements, we use the assumed strain method to project out these strains as in [**26**]. We find that while for the 1st order spectral elements we do need this assumed strain projection for good convergence, for spectral elements of order greater than 1, the proposed method can give good convergence without the assumed strain projection. This is due to the fact that the polynomial basis of higher order spectral elements can provide the polynomial terms needed to eliminate the extraneous enriched terms in blending element.

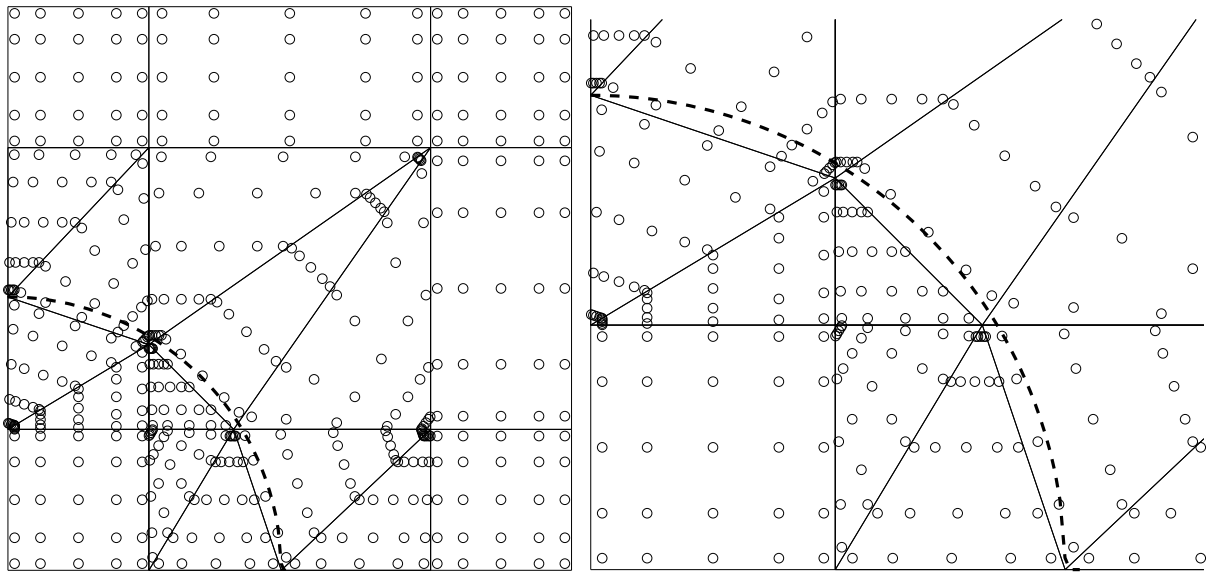

(a) Whole domain. (b) Zoom in.

Figure 2.5. Integration of a third order enriched spectral element by rectilinear triangular sub-domains; ∘ denotes the quadrature points.

2.3.3. Element subdivision for quadrature

For elements cut by the discontinuity, the quadrature of the weak form needs to be modified. For this purpose, we need to approximate Ω^{e+} and Ω^{e-} where

$$\Omega^{e+} = \Omega^e \cap (f(\mathbf{x}) > 0)$$

$$\Omega^{e-} = \Omega^e \cap (f(\mathbf{x}) < 0)$$

While in our previous work with low order elements [**26**], we have found approximations of the domains Ω^{e+} and Ω^{e-} by simple patterns of straight sided triangles sufficient; for higher order spectral elements, to exploit their innate accuracy, better approximations of the shape are needed. An approach to extending this 'cutting' method to higher order

element is to consider those small rectangles Ω_R^f formed by a repartition of a higher order element, see Figure 2.4, i.e. $\Omega^e = \bigcup_f \Omega_R^f$. Figure 2.5 shows one 3rd order spectral element subdivided into rectilinear quadrature subdomains. In each sub-rectangle Ω_R^f, if it contains the discontinuity, we split it into triangles according to the values of the signed distance function for the corner nodes of this rectangle, so that $\Omega_R^f = \bigcup_g \Omega_T^g$. The small circles indicate the quadrature points (the quadrature order, which determines the number of the quadrature points needed, is explained in the next section). The dotted line indicates the location of the discontinuity. If we zoom in, we can see from Figure 2.5(b) that this method introduces some errors, which impairs the convergence of the method, as shown later.

Our studies show that for curved discontinuities, a better technique is to subdivide the quadrilateral into isoparametric triangles with curved sides. We have used 6-node quadratic and 10-node cubic triangles for subdivision of a spectral element as shown in Figure 2.6. Figure 2.7 shows the domain subdivision for a 4 element mesh around a circular inclusion.

2.3.4. Quadrature order

For the p-th order spectral element in 1D without enrichment, the continuous approximation field is p-th order, the derivative is $p-1$, so the stiffness matrix is order $2\,(p-1)$. In the enriched elements, the enrichment function ψ is approximated through the interpolation by the same spectral element as in (2.20). For a $p=1$ local partition of unity, the polynomial order is then $p+1$ since the enriched part is the product of the linear shape function and the enrichment function $\psi\,(\mathbf{x})$ approximated by the spectral interpolation.

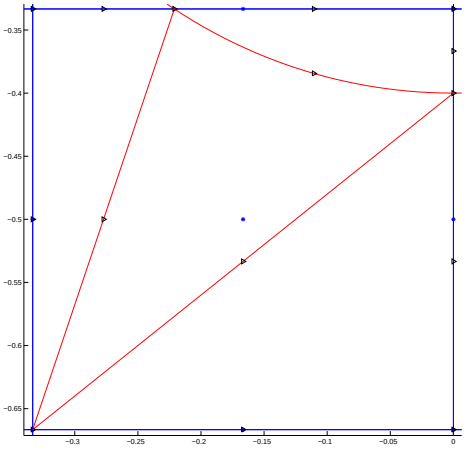

(a) 6-node triangle subdivision for a 2nd order spectral element. $*$ denotes the nodes for spectral elements; $\triangleright$ denotes the nodes for 6-node triangles.

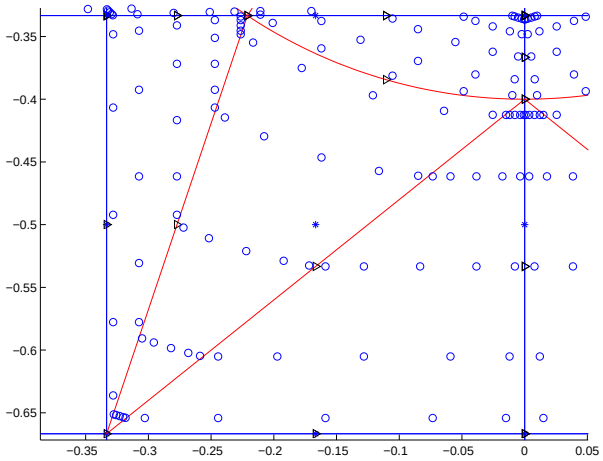

(b) Quadrature points obtained from the 6-node triangle subdivision for a 2nd order spectral element. $*$ denotes the nodes for spectral elements; $\circ$ denotes the quadrature points; $\triangleright$ denotes the nodes for 6-node triangles.

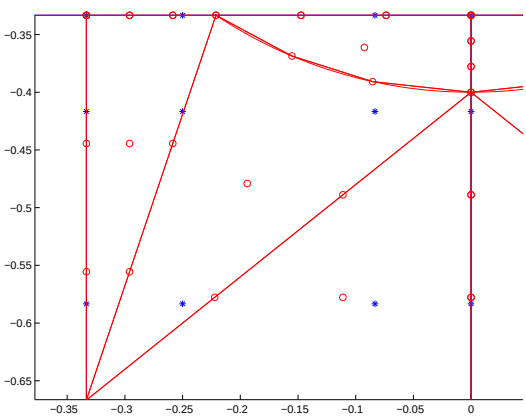

(c) 10-node triangle subdivision for a 3rd order spectral element. $*$ denotes the nodes for spectral elements; $\circ$ denotes the nodes for 6-node triangles.

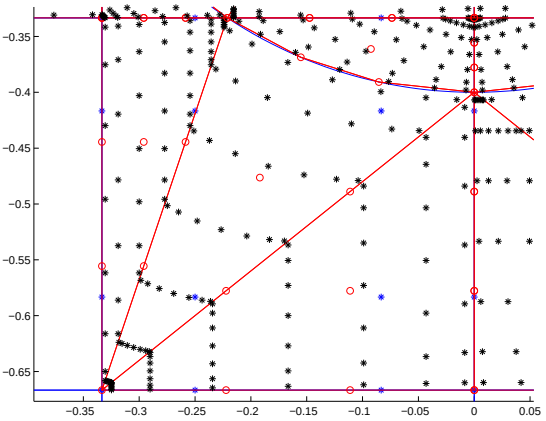

(d) Quadrature points obtained from the 10-node triangle subdivision for a 3rd order spectral element. Blue $*$ denotes the nodes for spectral elements; black $*$ denotes the quadrature points; $\circ$ denotes the nodes for 6-node triangles.

Figure 2.6. Element subdivision and quadrature points for the 6-node quadratic and 10-node cubic triangles.

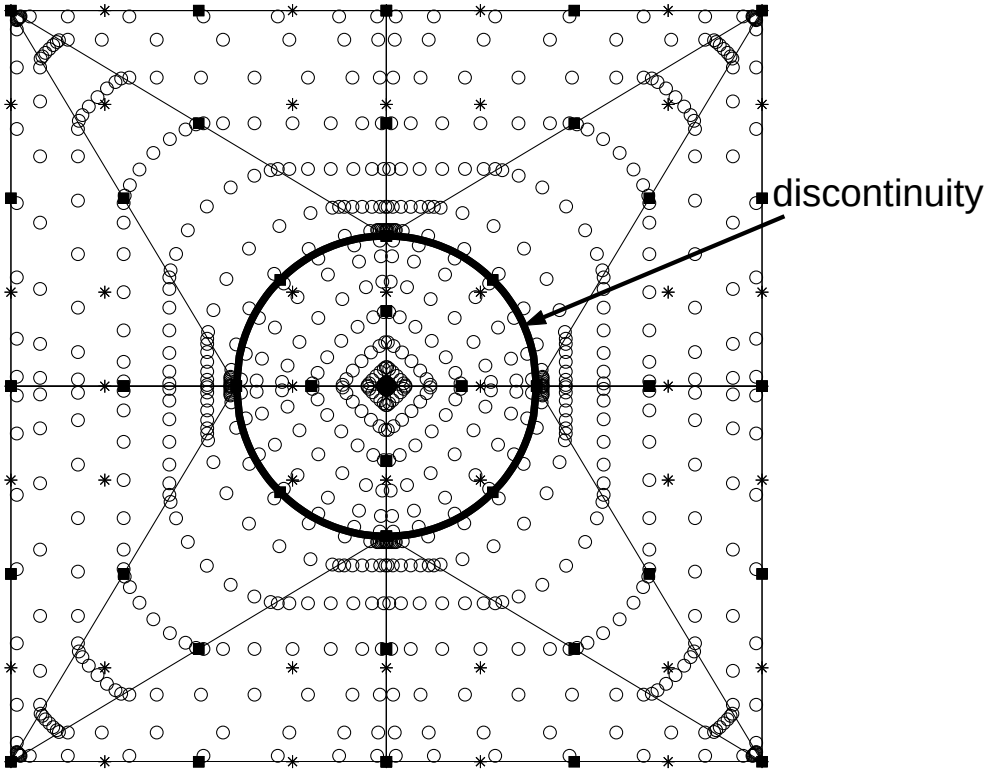

Figure 2.7. Element subdivision and quadrature points for the 3rd order spectral element mesh around a circular inclusion. $*$ denotes the nodes for spectral elements; $\circ$ denotes the quadrature points; $\blacksquare$ denotes the nodes for 6-node triangles.

In 2D, the stiffness matrix is integrated by $n_Q \times n_Q$ Gauss quadrature, where n_Q is the number of quadrature points. Gauss quadrature gives exact integration for polynomials up to order $(2n_Q - 1)$. The polynomial is of order $p+1$, so the stiffness is of order $2(p+1)$. Therefore, we need at least $n_Q = integer([2(p+1)+1]/2)$ quadrature points along one direction. Here, $integer()$ is the next highest integer.

In order to integrate the weak form for higher order spectral elements, we map quadrilateral to a triangle as shown in Figure 2.8. Note that this method doesn't distribute the

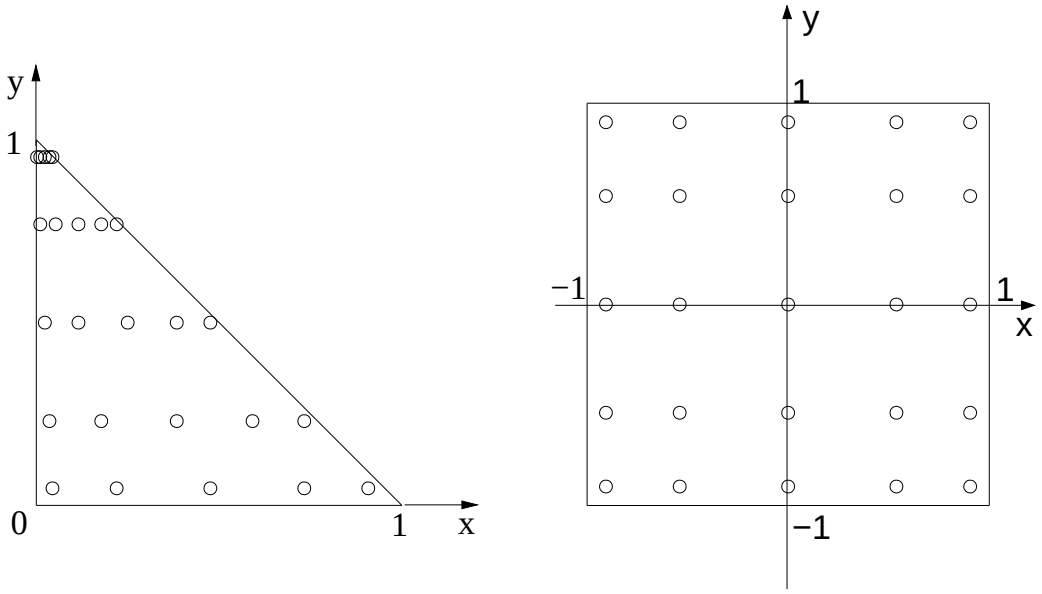

Figure 2.8. Integration points in quadrilaterals for triangles; ∘ denotes the quadrature points.

quadrature points evenly, their distribution is not symmetric, and the quadrature points depend on the node numbering, but these effects are minor.

2.4. NUMERICAL RESULTS

In the following, we examine the performance of our method. The enrichment function $\psi(\mathbf{x})$ is chosen to be the function of the signed distance.

2.4.1. Analysis of eigenmodes

Consider the problem of two bodies smoothly contacting with relative sliding as shown in Figure 2.9, which is a strong discontinuity problem. These problems were proposed in Ref. [**13**] as checks on methods for discontinuities. Rectangular meshes not aligned with the discontinuities as shown in Figure 2.10 are used. One eigenvalue should equal

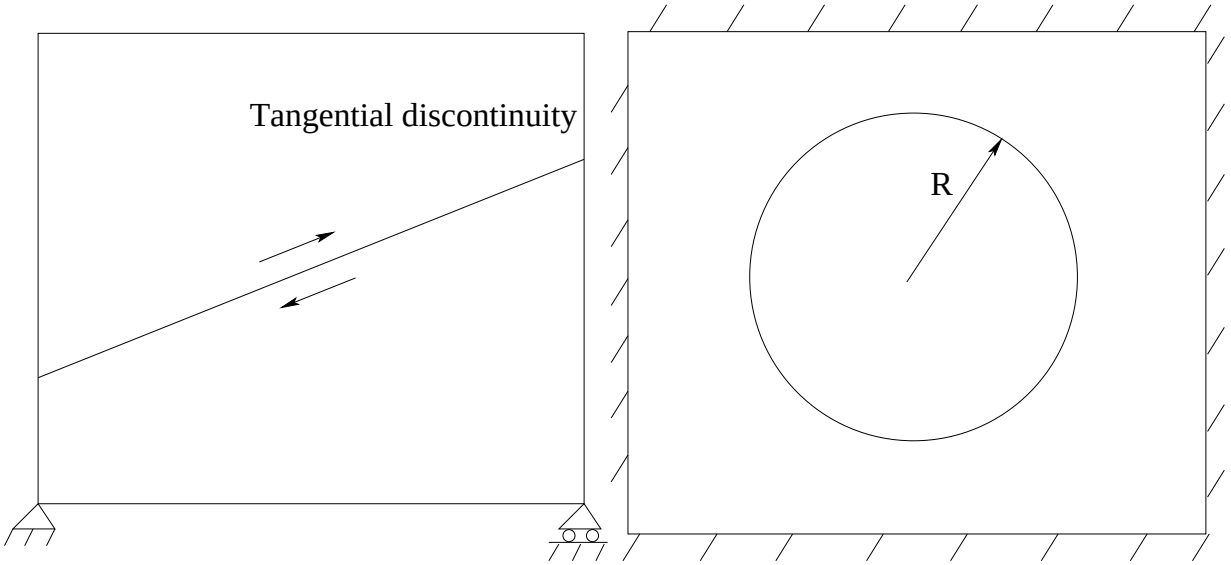

(a) Tangential discontinuity of a square black. (b) Tangential discontinuity of the journal bearing.

Figure 2.9. Tangential discontinuities.

exactly zero, corresponding to the rigid body mode of the top body in Figure 2.9(a). The enrichment given in equation (2.12) is used.

Figure 2.10(a) shows the eigenvector corresponding to the rigid-body mode for the straight discontinuity problem of Figure 2.9(a). The mark "*" denotes the nodes for the spectral elements. The lowest eigenvalues are -1.094×10^{-16}, 2.233×10^{-16}, -1.045×10^{-15}, 2.252×10^{-15} for the 1st, 2nd, 3rd and 4th order spectral elements, respectively. Figure 2.10(a) gives the results for $p = 4$.

Figure 2.9(b) shows an inclusion in an elastic body; relative tangential displacement is permitted between the bodies, so the problem represents a frictionless journal bearing. Figure 2.10(b) gives the results for the journal bearing with $p = 1$. The lowest eigenvalues for the journal bearing problem are 1.224×10^{-4}, 1.813×10^{-6}, 8.222×10^{-7} for the 1st,

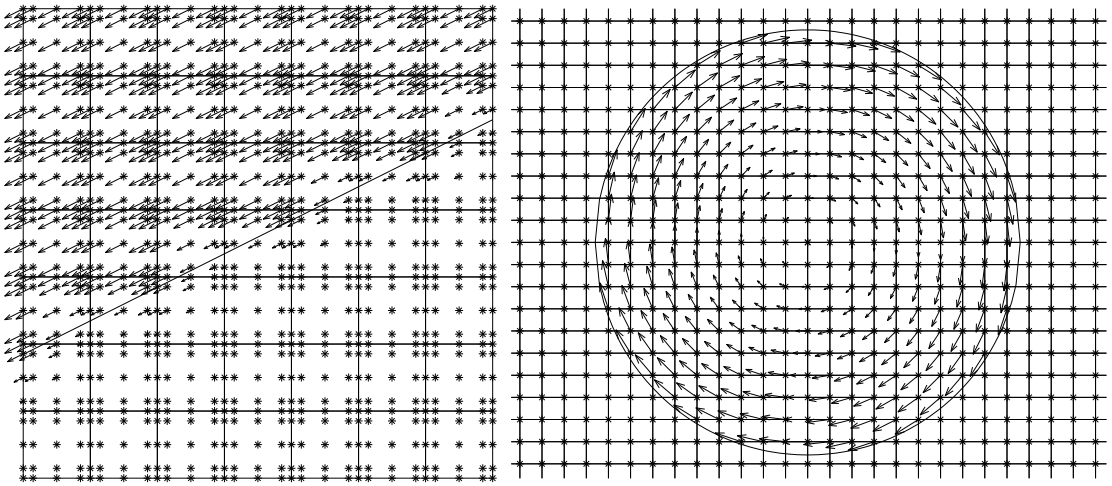

(a) Sliding blocks. (b) Journal bearing.

Figure 2.10. Displacement mode corresponding to the lowest eigenvalue; * denotes the nodes of the spectral element.

2nd and 3rd order spectral elements, respectively. In both problems the eigenvalues are within machine precision of zero.

2.4.2. Poisson equation with discontinuous coefficients

The configuration of this problem is illustrated by Figure 2.11. The material parameters are $k_1 = 1, k_2 = 10$. We generate the meshes so that the interface is not coincident with the element edges. The governing equation is

$$\nabla \cdot (k \nabla u) + b = 0 \quad \text{where} \quad \begin{cases} k(\mathbf{x}) = k_1 = 1 & \text{for} \quad 0 \leq x < 5 \\ k(\mathbf{x}) = k_2 = 10 & \text{for} \quad 5 \leq x \leq 10. \end{cases} \tag{2.27}$$

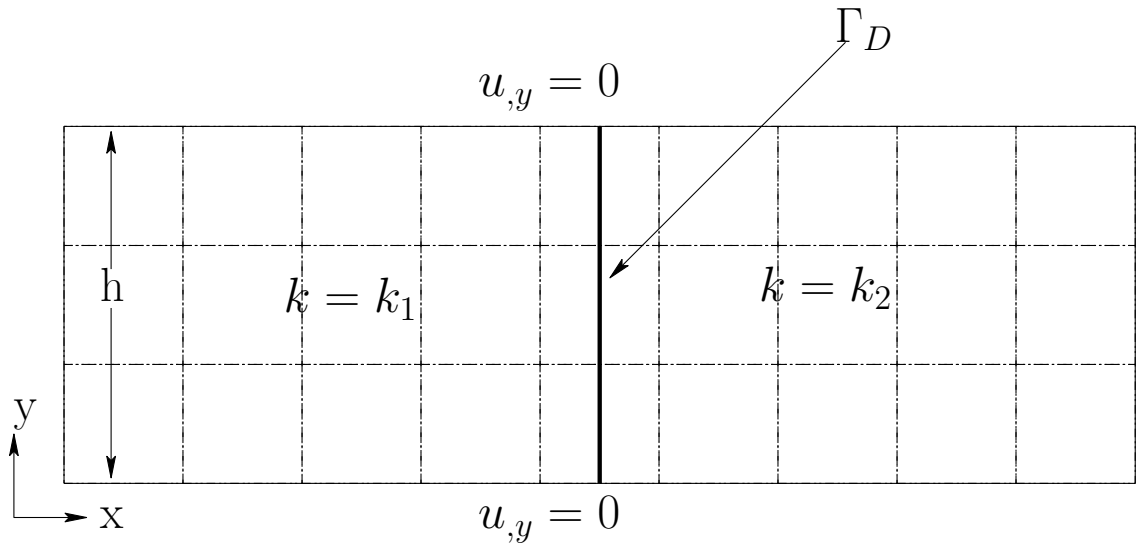

Figure 2.11. Bi-material plate problem with mesh.

with boundary conditions

$$\begin{aligned} u_{,y}|_{y=0} = 0 \quad \text{and} \quad u_{,y}|_{y=h} = 0 \\ u|_{x=0} = 0 \\ k_2 u_{,x}|_{x=10} = 1 \end{aligned} \tag{2.28}$$

The exact solution to this problem for $b = 0$ is

$$u(x,y) \;=\; \begin{cases} \frac{q}{k_1} x & 0 \le x < 5 \\ q\left(\frac{x-5}{k_2} + \frac{5}{k_1}\right) & 5 \le x \le 10 \end{cases} \tag{2.29}$$

The enrichment given in equation (2.7) is used. Figure 2.12 shows the convergence of the energy norm error. In these results, only $N_I^1(\mathbf{x})$ was used for the local partition of unity.

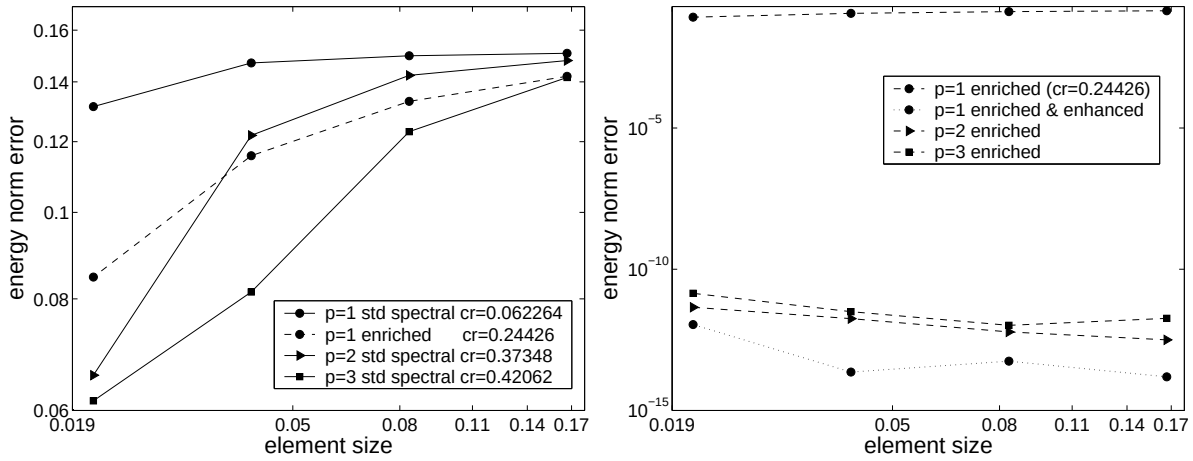

(a) Standard spectral element.

(b) Enriched and enhanced spectral element.

Figure 2.12. Convergence of the error in energy norm for bi-material plate problem; cr = rate of convergence, std = standard.

As can be seen from Figure 2.12(a), the performance of standard spectral elements is very poor in the presence of the discontinuity. For the enriched element with $p = 1$, the results are improved over the standard solution without enrichment but still quite poor and the convergence rate is suboptimal, cr= 0.2443. The convergence rate reported in this and the next problems are regression fits to the data. When the blending elements are enhanced as in Chessa et al [**26**] by the assumed strain method, the results improve tremendously for $p = 1$ and are almost exact (the slight error can be attributed to roundoff errors). For $p = 2$ or $p = 3$, the assumed strain method is not needed and excellent results can be obtained by just enrichment.

2.4.3. Manufactured bimaterial problem

The previous problem does not provide a good picture of the accuracy of various methods since the results are converged within machine precision for $p \geq 2$. Therefore we have "manufactured" a problem with a discontinuity for which the solution is not spanned by the enriched basis. The problem is identical to the previous problem except that $k_1 = 1,\ k_2 = 2$ and

$$b(x) = \begin{cases} 4k_1 \sin 2x & \text{for} \quad -0.4 \leq x < 0 \\ k_2 \sin x & \text{for} \quad 0 \leq x \leq 0.5. \end{cases} \tag{2.30}$$

The exact solution is

$$u(x,y) = \begin{cases} \sin 2x & \text{for} \quad -0.4 \leq x < 0 \\ \sin x & \text{for} \quad 0 \leq x \leq 0.5. \end{cases} \tag{2.31}$$

We apply the exact solution on left and right sides as Dirichlet boundary conditions. For comparison, Figure 2.13(a) gives the energy norm error versus the element size for standard spectral elements. The meshes considered here are $3, 6, 12, 24$ elements along x direction for up to 4th order spectral elements. Figure 2.13(b) shows the same results but with the discontinuity residing on the edge. As can be see in Figure 2.13(a), the accuracy for the standard spectral element is very poor when the discontinuity occurs within the element. Comparison with Figure 2.13(b) shows that accuracy is many orders of magnitude less than when the discontinuity occurs at an edge, and the rate is only about 0.5, regardless of the order of the spectral interpolant.

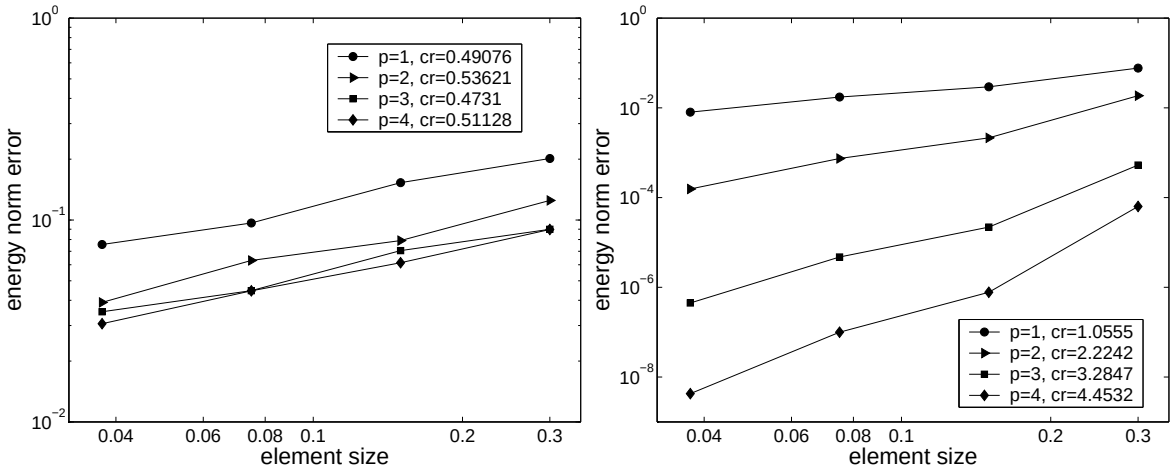

(a) Not coincident with element edges.

(b) Coincident with element edges.

Figure 2.13. Convergence of the error in energy norm for manufactured bi-material problem with discontinuity (a) not coincident with element edges and (b) coincident with element edges; cr=rate of convergence; no enrichment is used here.

Figure 2.14 shows the results for the enriched spectral elements. The accuracy is nearly as good as when the discontinuity is on an edge and the rates of convergence are nearly optimal. For $p = 1$, assumed strain blending elements are needed to recover the optimal rate of convergence. On the other hand, for $p \geq 2$, we found that assumed strain blending elements have little effect.

2.4.4. Circular inclusion

We consider next the elastostatic problem of a circular inclusion; it was previously considered in [**85**]. The Lamé constants for the inclusion with the radius R and the outside matrix with the radius b are different (λ_1, μ_1) and (λ_2, μ_2). The exact solution for this

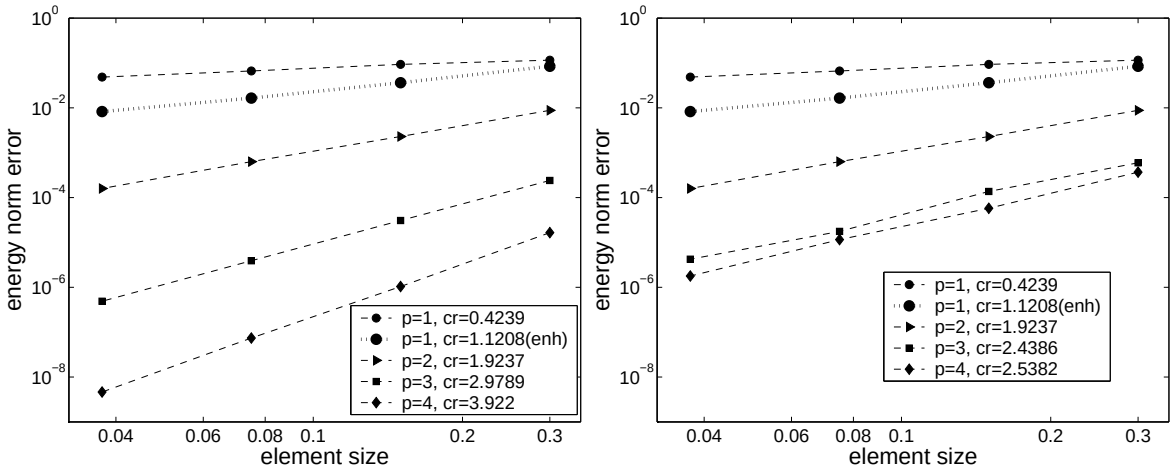

(a) N^{P-1} for partition of unity.

(b) N^1 for partition of unity.

Figure 2.14. Convergence of the error in energy norm for manufactured bimaterial problem with XFEM; cr=rate of convergence.

problem is

$$\begin{aligned} u_r &= \left[\left(1-\tfrac{b^2}{R^2}\right)\alpha + \tfrac{b^2}{R^2}\right] r \qquad & u_\theta &= 0 \\ \epsilon_{rr} &= \left(1-\tfrac{b^2}{R^2}\right)\alpha + \tfrac{b^2}{R^2} & \epsilon_{\theta\theta} &= \left(1-\tfrac{b^2}{R^2}\right)\alpha + \tfrac{b^2}{R^2} \\ \epsilon_{r\theta} &= 0 \end{aligned} \tag{2.32}$$

inside the inclusion ($0 \le r \le R$) and

$$\begin{aligned} u_r &= \left(r-\tfrac{b^2}{r}\right)\alpha + \tfrac{b^2}{r} \qquad & u_\theta &= 0 \\ \epsilon_{rr} &= \left(1+\tfrac{b^2}{r^2}\right)\alpha - \tfrac{b^2}{r^2} & \epsilon_{\theta\theta} &= \left(1-\tfrac{b^2}{r^2}\right)\alpha + \tfrac{b^2}{r^2} \\ \epsilon_{r\theta} &= 0 \end{aligned} \tag{2.33}$$

outside the inclusion ($R \le r \le b$) where

$$\alpha = \frac{(\lambda_1+\mu_1+\mu_2)b^2}{(\lambda_2+\mu_2)R^2 + (\lambda_1+\mu_1)(b^2-R^2) + \mu_2 b^2}. \tag{2.34}$$

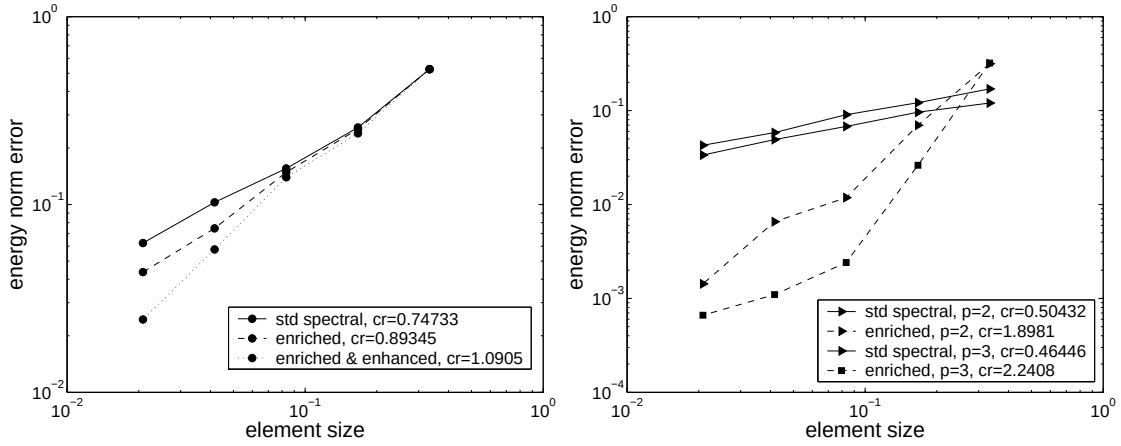

(a) 1st order element. (b) 2nd and 3rd order element.

Figure 2.15. Convergence rates of energy norm error for circular inclusion problem with the rectilinear triangular subdomains for quadrature; cr=rate of convergence, std=standard.

and R is the radius of the material interface and b is the outer radius. We use the following parameters: $R = 0.4$, $b = 2.0$, $\lambda_1 = 0.4$, $\mu_1 = 0.4$, $\lambda_2 = 5.769$, $\mu_2 = 3.846$. The radial (σ_{rr}) and hoop ($\sigma_{\theta\theta}$) stresses are

$$\begin{aligned} \sigma_{rr} &= 2\mu\epsilon_{rr} + \lambda(\epsilon_{rr} + \epsilon_{\theta\theta}) \\ \sigma_{\theta\theta} &= 2\mu\epsilon_{\theta\theta} + \lambda(\epsilon_{rr} + \epsilon_{\theta\theta}) \end{aligned} \tag{2.35}$$

We studied the convergence rate of the energy norm error for this problem. In these studies, we used a local partition of unity based on $N^1(\mathbf{x})$. We have found that for curved boundaries, there is no improvement for an $N^{P-1}(\mathbf{x})$ local partition of unity. For comparison, we also show the results with the subdomain quadrature method illustrated in Figure 2.7. From Figure 2.15 we see that integration on rectilinear subdomains impairs

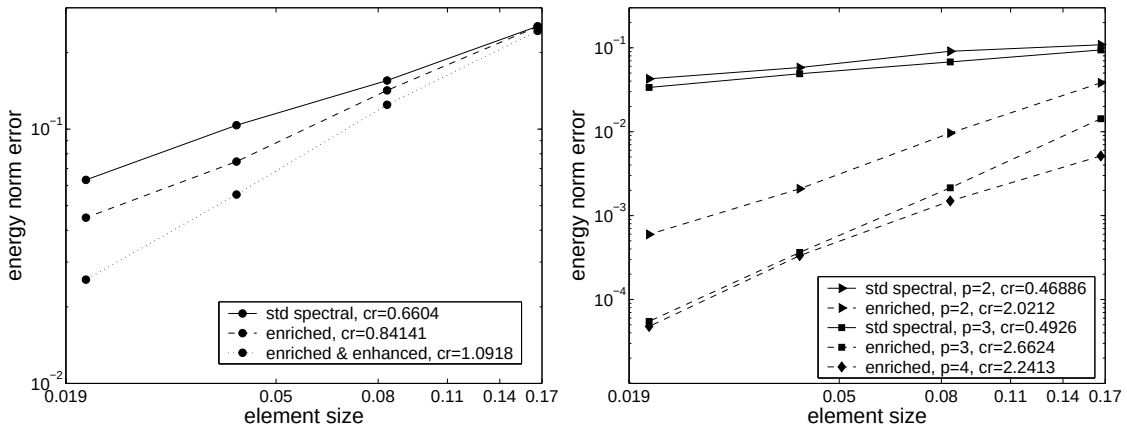

(a) 1st order element. (b) 2nd, 3rd and 4th order element.

Figure 2.16. Convergence rates of energy norm error for circular inclusion problem with curved 6-node triangular subdomains for quadrature; cr=rate of convergence, std=standard.

the results for the spectral element with order greater than 1. In Figure 2.16, we show the results obtained by the 6-node triangular subdivision quadrature method. The 2nd and 3rd order spectral methods give convergence rates around 2 and 2.6, respectively. But for the 4th order spectral elements, the convergence rate is impaired. We believe this is due to the effects of quadrature again although the accuracy of the results is slightly higher than for order 3.

The condition numbers for the stiffness matrix for different orders of the spectral element and different meshes are shown in Table 2.1. We can see the condition numbers increase exponentially with the orders of the spectral element. For a specific order, the condition numbers become bigger as the meshes get finer.

Table 2.1. Condition numbers for the stiffness matrix of the circular inclusion problem.

mesh used	6×6	12×12	24×24
$p = 1$, enriched	5.56×10^2	4.25×10^3	2.66×10^4
$p = 1$, enriched and enhanced	1.82×10^3	1.11×10^4	2.23×10^5
$p = 2$, enriched	1.43×10^5	7.04×10^5	2.15×10^7
$p = 3$, linear enriched	6.89×10^6	2.00×10^8	2.79×10^8
$p = 3$, quadratic enriched	1.00×10^8	8.85×10^7	2.63×10^8

2.5. CONCLUSIONS

An enrichment method for treating arbitrary discontinuities in functions and their gradients in the context of spectral elements has been presented. With this method, the edges of the elements do not need to be coincident with the discontinuity. This is particularly useful in moving discontinuity problems, where maintaining coincidence between element edges and the discontinuity entails remeshing.

The methodology is based on a local partition of unity technique and is similar to the developments for low order elements in Belytschko et al [**13**], and Chessa et al [**26**]. However, we found that for spectral elements with $p > 1$, there is no need to employ special blending elements in the blending domain. Similarly, for discontinuities in functions, the blending domain treatment is not important. On the other hand, care must be taken in the quadrature of the weak form. For curved interfaces, approximation of the subdomains of the element with the discontinuity by rectilinear triangles severely impairs the accuracy of the method.

We have studied local partitions of unity that employ $p = 1$ elements and $p - 1$ elements for the construction of the local partition of unity (where p is the order of the continuous approximation.) We found that for straight discontinuities, the $p-1$ partition

of unity elements provides optimal convergence. For curved discontinuities, $p = 1$ was somewhat more accurate than $p - 1$, but neither recovered the optimal convergence rate of the spectral element. We are still not clear why the optimal convergence rate cannot be recovered for curved discontinuities.

The methodology is promising for a wide variety of applications involving partial differential equations with discontinuous coefficients. The implementation of these techniques in a finite element program is quite straightforward since only the element is modified.

CHAPTER 3

A Variationally Consistent Immersed Element Method For Fluid-Structure Interaction

3.1. INTRODUCTION

The immersed boundary (IB) method [**89**], pioneered by Peskin [**77, 78**], is widely used in the simulation of the fluid-structure interactions (FSI) for biomechanical problems such as the heart. In this method, the interaction between the fluid and the solid is accomplished by smoothed Dirac delta functions which transfer forces from the volumeless solid and enforce velocity continuity across the fluid-structure interface. A variational basis for the method has not been given. Wang et al. [**92**] extended this method to finite element methods. Zhang et al. [**95, 94**] have developed the immersed finite element method (IFEM) based on this work. Liu et al. [**65**] have proposed a mathematical basis for this method. Their method is sequential [**96**], i.e. the fluid and the solid are solved separately and they use an incompressible fluid.

Legay et al. [**61**] developed an Eulerian-Lagrangian method using level sets [**13**] based on the work by Chessa and Belytschko [**24, 23, 22**] for solving two-phase flow problems by eXtended Finite Element Method (XFEM) [**69**]. Independent Lagrangian description for the solid and Eulerian description for the fluid are used, which enables arbitrary alignments between the solid and the fluid meshes. The continuity of velocities of the solid and fluid on the interface must be imposed by penalty or Lagrange multiplier

methods. The irregular interface is regularized by the zero level set. The characteristic Galerkin method [**37, 97, 98**] is used for the fluid solver. However, the method needs the interface integration for the coupling which is a line integration in 2D and a surface integration in 3D. Wagner et al. [**91**] applied XFEM on particulate flow for rigid particles. They enriched the finite element space by the asymptotic solutions for particles floating in Stokes flow [**51**].

The ghost fluid method [**42, 41**] captures the interface continuity conditions by defining ghost cells on the other side of the interface. An Eulerian description is employed for the fluid for this method. The interface conditions are captured by constructing ghost cells with the velocity and the pressure of the real fluid and the entropy on the other side of the interface. In combination with the level sets [**70, 87, 81**] and the isobaric fix technique [**43**], they have treated multi dimensional problems. Radovitzky et al. [**29, 88**] implemented the ghost fluid method with the finite volume method to calculate shell-fluid coupling problems in which a Lagrangian description is used for the shell. A priori knowledge of the interface location is used to extrapolate fields into the ghost cells. Manipulation of the fields in the ghost cells to enforce the interface conditions is crucial in this method.

Glowinski et al [**44, 45**] and Patankar et al. [**75**] have developed the fictitious domain method to treat the coupling of fluid and the rigid body particles. The rigid solid is filled with a fictitious fluid with the same density and viscosity as the surrounding fluid. Some of the mass and inertia is assigned to the fictitious fluid. Compatibility between the fluid and solid is imposed by Lagrange multiplier in the solid region [**46**].

The mortar method [**93**] is originally developed as a domain decomposition method for coupling nonconforming subdomains modeled for spectral elements [**62**]. In this method, the interface continuity conditions are realized by Lagrange multipliers [**74**]. Baaijens developed the fictitious domain/mortar element method for incompressible fluid-structure interaction [**1**]. Slender solids are coupled to the fluid by Lagrange multipliers for the velocities. His work is applied to the computations of aortic valve in [**48**].

Belytschko and Kennedy [**9, 4**] exploited the advantages of Lagrangian meshes for fluid formulations for fluid-structure interaction problems. Radovitzky and Ortiz [**80**] developed fully Lagrangian finite element analysis for Newtonian flows. Although Lagrangian description for fluid can easily treat the problems as free surface flow and interfaces between two phases, unavoidable continuous remeshing has to be carried on for large deformation problems. Belytschko et al. [**10, 5, 11, 15**] developed Arbitrary Lagrangian-Eulerian method (ALE). ALE [**73, 83, 56, 60, 40, 39, 63, 19, 67, 18**] adopts an intermediate mesh between the initial and the current configuration. By specifying the mesh velocity, it can ameliorate the severe mesh distortion but can not completely resolve the problem for extreme large deformations.

3.2. NOTATION

We consider a fluid-structure problem such as that shown in Figure 3.1 along with our nomenclature. We show only a single solid domain for simplicity, but the method can be applied to any number of solids. Superscripts "F" and "S" indicate whether the variables pertain to the fluid or solid. The fluid domain is denoted by Ω^{F} and the solid by Ω^{S}. External traction forces $\boldsymbol{\tau}^{\mathrm{F}}$ are applied on the fluid on the boundary $\Gamma_{\tau}^{\mathrm{F}}$ and on the

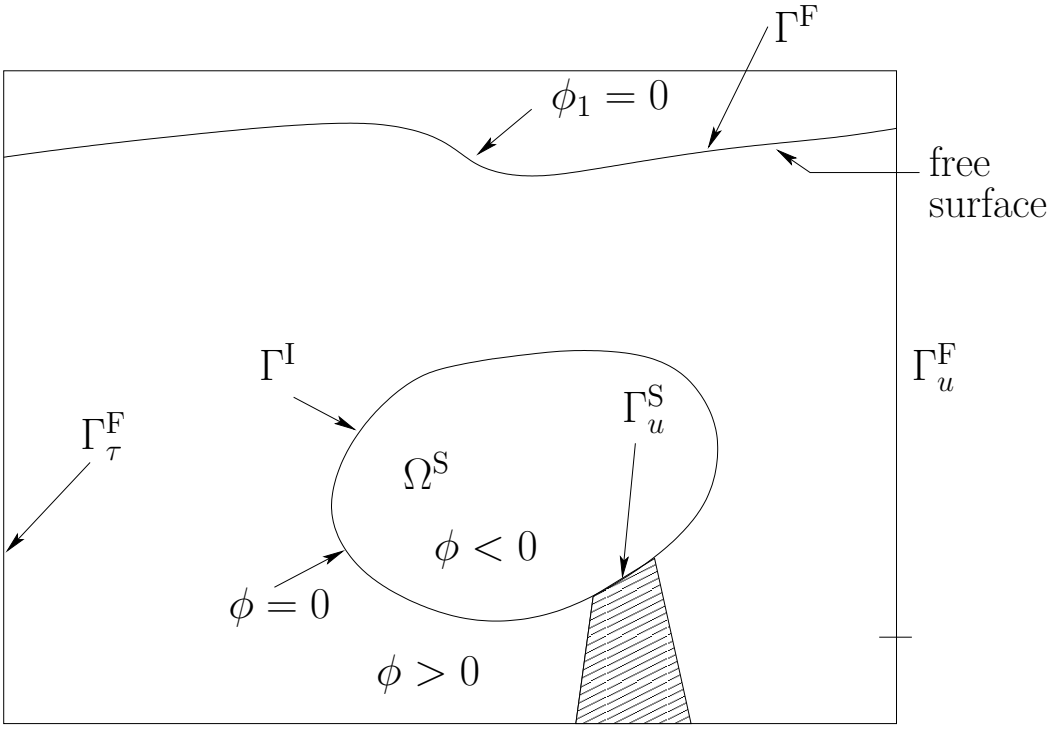

Figure 3.1. Fluid solid system with solid domain Ω^{S} and fluid domain Ω^{F}.

structure by $\boldsymbol{\tau}^{\mathrm{S}}$ on Γ^{S}_τ. Note that this boundary Γ^{F}_τ does not include the fluid-structure interface. In addition we have the body forces on the fluid and solid, which are denoted by $\boldsymbol{b}^{\mathrm{F}}$ and $\boldsymbol{b}^{\mathrm{S}}$, respectively, which are in units of force per unit mass. We assume that the material constants, such as density and bulk modulus are smooth within the domain, except on some interfaces Γ^{D}_i, which may occur either within the fluid or solid. We assume that these discontinuities move with the material. The surfaces of discontinuity include the fluid-structure interface, so the totality of surfaces of discontinuity is

$$\Gamma^{\mathrm{D}} = \Gamma^{\mathrm{I}} \cup \sum_i \Gamma^{\mathrm{D}}_i \tag{3.1}$$

Note that the fluid-solid interface moves with the material.

The spatial coordinates are denoted by $\boldsymbol{x}$, the material coordinates by $\boldsymbol{X}$. The motion of the solid is given by

$$\boldsymbol{x} = \boldsymbol{x}^{\mathrm{S}}(\boldsymbol{X}, t) \tag{3.2}$$

for $\boldsymbol{X} \in \Omega^{\mathrm{S}_0}$. The velocity field of the structure is given by the material time derivative of the above:

$$\boldsymbol{v}^{\mathrm{S}}(\boldsymbol{X}, t) = \frac{\partial \boldsymbol{x}^{\mathrm{S}}(\boldsymbol{X}, t)}{\partial t} \tag{3.3}$$

The kinematics of the fluid is described by a velocity field $\boldsymbol{v}^{\mathrm{F}}(\boldsymbol{x}, t)$. Note that the description of the fluid is Eulerian (spatial).

The Cauchy stress is denoted by $\boldsymbol{\sigma}$, the density by ρ, and a superposed dot is material time derivative.

3.3. FLUID SOLVER

3.3.1. Momentum equation

The momentum equation is

$$\rho \dot{\boldsymbol{v}} = \nabla \cdot \boldsymbol{\sigma} + \rho \boldsymbol{b} \tag{3.4}$$

in Lagrangian description. If an Eulerian description is used, we have

$$\rho \frac{\partial \boldsymbol{v}}{\partial t} = -\rho \boldsymbol{v} \cdot \nabla \boldsymbol{v} + \nabla \cdot \boldsymbol{\sigma} + \rho \boldsymbol{b} \tag{3.5}$$

The additional term on the right hand side is from the material time derivative of the velocity. It is this term that brings the advection effect. Here the reference frame is the spatial coordinate instead of material coordinate. We define the right hand side of (3.5)

as the spatial residual

$$\boldsymbol{r} = -\rho \boldsymbol{v} \cdot \nabla \boldsymbol{v} + \nabla \cdot \boldsymbol{\sigma} + \rho \boldsymbol{b} \tag{3.6}$$

So (3.5) becomes

$$\rho \frac{\partial \boldsymbol{v}}{\partial t} = \boldsymbol{r} \tag{3.7}$$

As far as solving fluid problem by FEM, it is well known that we must overcome the instability problem caused by the convection term [**36**]. Various stabilization methods have been developed to solve fluid problems since 1970s such as SUPG[**20, 52**], GLS[**53**], and ENO[**49, 82**]. Taylor-Galerkin [**35**], [**66**] and Characteristic-Galerkin [**37**], [**79**], [**66**] are also two methods to stabilize fluid problems in Finite Element Method. Codina gave some comparisons of finite element methods used in fluid problems [**31, 33, 32**] . In [**97**], [**98**], they are combined with the projection method due to Chorin [**28**]. The Characteristic-Galerkin method can overcome the two major problems when solving fluid problem by FEM, i.e. violation of the BB condition and the instability caused by the convection term in Eulerian description. We follow this method to solve fluid problems. Instead of using the two step version of this method, we use the one step method which will not give us another Poisson equation for the mid-step velocity. The method is briefly reviewed here.

In the Characteristic Galerkin method, the term $\frac{\Delta t}{2}\mathbf{v} \cdot \nabla \mathbf{r}$ is added to the equation (3.7). This term can be explained as the gradient of the spatial residual projected onto the direction of streamline and also the time step as an parameter. It is similar to the Galerkin Least Square method [**53**]. The stabilized momentum equation becomes

$$\rho \frac{\partial \boldsymbol{v}}{\partial t} = \boldsymbol{r} - \frac{\Delta t}{2}\mathbf{v} \cdot \nabla \mathbf{r} \tag{3.8}$$

The weak form is obtained by multiplying (3.8) with the test function and integrate on the computational domain.

$$\int_\Omega \delta \boldsymbol{v} \cdot \rho \frac{\partial \boldsymbol{v}}{\partial t} \mathrm{d}\Omega = \int_\Omega \delta \boldsymbol{v} \cdot \boldsymbol{r} \mathrm{d}\Omega - \int_\Omega \delta \boldsymbol{v} \cdot \frac{\Delta t}{2} \mathbf{v} \cdot \nabla \mathbf{r} \mathrm{d}\Omega \tag{3.9}$$

Integrate by parts the second term on the right hand side and ignore the boundary term

$$\int_\Omega \delta \boldsymbol{v} \cdot \rho \frac{\partial \boldsymbol{v}}{\partial t} \mathrm{d}\Omega = \int_\Omega \delta \boldsymbol{v} \cdot \boldsymbol{r} \mathrm{d}\Omega - \int_\Omega \left(\nabla \delta \boldsymbol{v} \cdot \boldsymbol{v} + \delta \boldsymbol{v} \nabla \cdot \boldsymbol{v} \right) \cdot (-\mathbf{r}) \, \mathrm{d}\Omega \tag{3.10}$$

For clarity, the Cartesian component form for the tensor is written out as

$$\int_\Omega \delta v_i \rho v_{i,t} \mathrm{d}\Omega = \int_\Omega \delta v_i r_i \mathrm{d}\Omega - \frac{\Delta t}{2} \int_\Omega (\delta v_i v_k)_{,k} (-r_i) \mathrm{d}\Omega \tag{3.11}$$

Here comma "," means the partial derivative. The final form for the momentum equation is

$$\begin{aligned} \int_\Omega \delta v_i \rho v_{i,t} \mathrm{d}\Omega \;\; = \;\; & - \int_\Omega \delta v_i \rho v_j v_{i,j} \mathrm{d}\Omega + \int_\Gamma \delta v_i t_i \mathrm{d}\Gamma - \int_\Omega \delta v_{i,j} \sigma_{ij} \mathrm{d}\Omega \\ & + \int_\Omega \delta v_i \rho b_i \mathrm{d}\Omega - \frac{\Delta t}{2} \int_\Omega (\delta v_i v_k)_{,k} (\rho v_j v_{i,j} - \sigma_{ij,j} - \rho b_i) \mathrm{d}\Omega \end{aligned} \tag{3.12}$$

where $\boldsymbol{t}$ is the traction on the boundary.

3.3.2. Constitutive relation of fluid

We use the following constitutive law for the fluid.

$$\boldsymbol{\sigma} = -p\boldsymbol{I} + \boldsymbol{\tau} \tag{3.13}$$

where $\boldsymbol{I}$ is the second order isotropic tensor and $\boldsymbol{\tau}$ is the viscous stress which is considered as a linear function of the rate of deformation tensor $\boldsymbol{D}$ here. For an isotropic Newtonian fluid, $\boldsymbol{\tau}$ and $\boldsymbol{D}$ are related by a fourth order isotropic tensor which has only two independent parameters. As the two Lamé parameters for the linear elastic solid, if λ^* and μ^* are introduced, the viscous stress can be expressed as

$$\boldsymbol{\tau} = \lambda^* \text{trace}\left(\boldsymbol{D}\right) \boldsymbol{I} + 2\mu^* \boldsymbol{D} \tag{3.14}$$

The viscous stress can also be written as

$$\boldsymbol{\tau} = \left(\lambda^* + \frac{2}{3}\mu^*\right) \text{trace}\left(\boldsymbol{D}\right) \boldsymbol{I} + 2\mu^* \left(\boldsymbol{D} - \frac{1}{3}\text{trace}\left(\boldsymbol{D}\right) \boldsymbol{I}\right) \tag{3.15}$$

$$\boldsymbol{\tau} = k^* \text{trace}\left(\boldsymbol{D}\right) \boldsymbol{I} + 2\mu^* \boldsymbol{D}' \tag{3.16}$$

where $k^* = \left(\lambda^* + \frac{2}{3}\mu^*\right)$ is the bulk viscosity and $\boldsymbol{D}'$ is the deviatoric rate of deformation tensor. Considering the Stokes condition, $k^* = 0$, which comes from the evidence of rare observation of the bulk viscosity in experiments, the first term in (3.16) is dropped

$$\boldsymbol{\tau} = 2\mu^* \boldsymbol{D}' \tag{3.17}$$

We also mention that for incompressible fluid, $\boldsymbol{D}' = \boldsymbol{D}$, so that the viscous stress is

$$\boldsymbol{\tau} = 2\mu^* \boldsymbol{D} \tag{3.18}$$

For convenience, we list the Cartesian component forms

$$\tau_{ij} = \lambda^* D_{kk} \delta_{ij} + 2\mu^* D_{ij} \tag{3.19}$$

$$\tau_{ij} = \lambda^* v_{k,k}\delta_{ij} + \mu^* \left(v_{i,j} + v_{j,i}\right) \tag{3.20}$$

$$\tau_{ij} = k^* D_{kk}\delta_{ij} + 2\mu^* D'_{ij} \tag{3.21}$$

$$\tau_{ij} = k^* v_{k,k}\delta_{ij} + \mu^* \left(v_{i,j} + v_{j,i} - \frac{2}{3} v_{k,k}\delta_{ij}\right) \tag{3.22}$$

3.3.3. Continuity equation

The mass conservation equation in Eulerian description is

$$\dot{\rho} + \rho\nabla \cdot \boldsymbol{v} = 0 \tag{3.23}$$

It is equivalent to the following two forms

$$\frac{\partial \rho}{\partial t} + \boldsymbol{v} \cdot \nabla\rho + \rho\nabla \cdot \boldsymbol{v} = 0 \tag{3.24}$$

$$\frac{\partial \rho}{\partial t} + \nabla \cdot (\rho \boldsymbol{v}) = 0 \tag{3.25}$$

Similar to the momentum equation, we also need to stabilize this equation. We will use the Characteristic-Galerkin method [**97, 98**]. The stabilized continuity equation becomes

$$\frac{\partial \rho}{\partial t} + \nabla \cdot (\rho \boldsymbol{v}) - \Delta t\theta_1 \nabla^2 p = 0 \tag{3.26}$$

where ∇^2 is the Laplacian. The weak form is obtained by multiplying the test function to the above equation and integrate on the computational domain.

$$\int_\Omega \delta\rho \left(\frac{\partial \rho}{\partial t} + \nabla \cdot (\rho \boldsymbol{v}) - \Delta t\theta_1 \nabla^2 p\right) \mathrm{d}\Omega = 0 \tag{3.27}$$

Also, if we integrate by parts on the stabilization term and ignore the boundary term, we get

$$\int_{\Omega} \delta\rho \left(\frac{\partial \rho}{\partial t} + \nabla \cdot (\rho \boldsymbol{v}) \right) \mathrm{d}\Omega + \Delta t \theta_1 \int_{\Omega} \nabla \delta\rho \cdot \nabla p \mathrm{d}\Omega = 0 \tag{3.28}$$

3.3.4. Equation of state

We use the following equation as equation of state to update the pressure.

$$\Delta p = c^2 \Delta \rho = \frac{k}{\rho} \Delta \rho \tag{3.29}$$

where c is the sound velocity in the media and k is the bulk modulus.

3.3.5. Shock capturing

For hyperbolic equations, if there are strong and weak discontinuities, it is known that around those discontinuities, there will be some wiggles appearing in the numerical solution. And also the shock waves are likely to appear in compressible materials. Shock capturing method can suppress these wiggles and give smoother numerical solutions. For the sake of capturing potential shocks, many shock capturing methods have been developed [**71**]. Considering that the streamline direction is already stabilized by some viscosity, an anisotropic diffusion tensor is adopted to smooth the results as in [**97**], [**30**]. With the addition of the anisotropic term, equation (3.8) becomes

$$\rho v_{i,t} = r_i - \frac{\Delta t}{2} v_k r_{i,k} + \sum_{e=1}^{Nel} \int_{\Omega^e} \left(\nu_{sc} \delta_{kj} v_{i,j} + (\nu_{sl} - \nu_{sc}) \left(\frac{v_k v_j}{v^2} \right) v_{i,j} \right)_{,k} \mathrm{d}\Omega \tag{3.30}$$

where ν_{sc} is the shock capturing viscosity and ν_{sl} is streamline viscosity. The viscosity parameters are listed below

$$\begin{aligned} \nu_{sc} &= \beta h \frac{|r_i|}{|\nabla v_i|} \\ \nu_{sl} &= \max(0, \nu_{sc} - \nu_{sg}) \\ \nu_{sg} &= \frac{\Delta t}{4} v^2 \end{aligned} \tag{3.31}$$

where h is the size of element and β is 0.3 for linear elements and 0.15 for quadratic elements. v^2 is the magnitude of the velocity. For example, in one dimension, the system will be

$$\begin{aligned} \rho v_{,t} &= r - \frac{\Delta t}{2} v r_{,x} + \sum_{e=1}^{Nel} \int_{\Omega^e} \left(\nu_{sc} v_{,x} + (\nu_{sl} - \nu_{sc})\, v_{,x}\right)_{,x} \mathrm{d}\Omega \\ \nu_{sc} &= \beta h \frac{|r|}{|v_{,x}|} \\ \nu_{sl} &= \max(0, \nu_{sc} - \nu_{sg}) \\ \nu_{sg} &= \frac{\Delta t}{4} v^2 \end{aligned} \tag{3.32}$$

3.4. GOVERNING EQUATIONS

We denote a unit normal to a surface by $\boldsymbol{n}$. The governing equations for the fluid/solid system are

$$\rho^{\mathrm{F}} \dot{\boldsymbol{v}}^{\mathrm{F}} = \nabla \cdot \boldsymbol{\sigma}^{\mathrm{F}} + \rho^{\mathrm{F}} \boldsymbol{b}^{\mathrm{F}} \quad \text{in} \quad \Omega^{\mathrm{F}} \tag{3.33}$$

$$\rho^{\mathrm{S}} \dot{\boldsymbol{v}}^{\mathrm{S}} = \nabla \cdot \boldsymbol{\sigma}^{\mathrm{S}} + \rho^{\mathrm{S}} \boldsymbol{b}^{\mathrm{S}} \quad \text{in} \quad \Omega^{\mathrm{S}} \tag{3.34}$$

$$\boldsymbol{\sigma}^{\mathrm{F}} \cdot \boldsymbol{n}^{\mathrm{F}} = \boldsymbol{\tau}^{\mathrm{F}} \quad \text{on} \quad \Gamma_{\tau}^{\mathrm{F}} \tag{3.35}$$

$$\boldsymbol{\sigma}^{\mathrm{S}} \cdot \boldsymbol{n}^{\mathrm{S}} = \boldsymbol{\tau}^{\mathrm{S}} \quad \text{on} \quad \Gamma_{\tau}^{\mathrm{F}} \tag{3.36}$$

$$\dot{\rho}^{\mathrm{F}} + \rho^{\mathrm{F}} \nabla \cdot \boldsymbol{v} = 0 \quad \text{in} \quad \Omega^{\mathrm{F}} \tag{3.37}$$

$$\rho^{\mathrm{S}}(\boldsymbol{X})\, J(\boldsymbol{X}) = \rho_0^{\mathrm{S}}(\boldsymbol{X}) \quad \text{in} \quad \Omega^{\mathrm{S}} \tag{3.38}$$

$$\sigma^{\mathrm{F}} \cdot \boldsymbol{n}^{\mathrm{F}} + \sigma^{\mathrm{S}} \cdot \boldsymbol{n}^{\mathrm{S}} = 0 \quad \text{on} \quad \Gamma^{\mathrm{I}} \tag{3.39}$$

$$\boldsymbol{v}^{\mathrm{F}} = \boldsymbol{v}^{\mathrm{S}} \quad \text{on} \quad \Gamma^{\mathrm{I}} \tag{3.40}$$

The first two are the momentum equations for the fluid and solid. Equations (3.35) and (3.36) are the traction boundary conditions. Equations (3.37) and (3.38) enforce mass conservation in the fluid and solid, respectively; note that since we anticipate a Lagrangian description for the solid, we use an algebraic equation for mass balance, see Belytschko et al [**12**]. The equations (3.39) and (3.40) give the continuity of momentum balance and velocities on the fluid-solid interface Γ^{I}. In the above, $J = \det(\mathbf{F})$, $F_{ij} = \frac{\partial x_i}{\partial X_j}$.

3.5. FORMULATION OF THE FLUID-STRUCTURE INTERACTION PROBLEM

3.5.1. Weak form

The material in the entire domain is governed by the momentum equation

$$\rho \dot{\boldsymbol{v}} = \nabla \cdot \boldsymbol{\sigma} + \rho \boldsymbol{b} \quad \text{on} \quad \Omega / \Gamma^{\mathrm{D}} \tag{3.41}$$

$$[\![\boldsymbol{n} \cdot \boldsymbol{\sigma}]\!] = 0 \quad \text{on} \quad \Gamma^{\mathrm{D}} \tag{3.42}$$

where $[\![\,]\!]$ is the jump function. The above momentum equations hold whether the fluid is treated by Eulerian or Lagrangian formulations. The weak form is: for $\sigma \in C^{-1}$ (i.e. the space of piecewise continuous integrable functions).

$$\int_{\Omega} \boldsymbol{w} \cdot \left(\rho \dot{\boldsymbol{v}} - \nabla \cdot \boldsymbol{\sigma}\left(\boldsymbol{v}\right) - \rho \boldsymbol{b}\right) \mathrm{d}\Omega = 0 \quad \forall w \in \mathscr{U} \quad \text{on}\, \Omega \tag{3.43}$$

where

$$\mathscr{U} = \left\{\boldsymbol{w} \in H^1\left(\Omega^{\mathrm{F}}\right), \boldsymbol{w} = 0 \quad \text{on} \quad \Gamma_u^{\mathrm{F}} \cup \Gamma_u^{\mathrm{S}}\right\} \tag{3.44}$$

The strong form corresponding to (3.43) is (3.41) and (3.42). Note that the jump condition (3.42) on the fluid-solid interface is identical to that on any other material interface. Equations (3.43) must be supplemented by a constitutive equation. The constitutive equations can be of two forms:

$$\text{either} \qquad \boldsymbol{\sigma} = \boldsymbol{\sigma}^{\mathrm{F}}\left(\nabla \boldsymbol{v}\right) \tag{3.45}$$

$$\text{or} \qquad \boldsymbol{\sigma} = \bar{\boldsymbol{\sigma}}^{\mathrm{S}}\left(\boldsymbol{F}\right) \tag{3.46}$$

where $\boldsymbol{F}$ is the deformation gradient. We have given the stress in the fluid as a function of the velocity gradient and in the solid as a function of the deformation gradient, which is customary but not essential. Examples of relevant constitutive equations are given later. It is assumed that the stresses are at lest C^0 functions of the strain measures.

We consider the development of discrete momentum equation for a formulation where the fluid is solved throughout the computational domain Ω, the solid is solved separately

and the two are combined to obtain the solution of the coupled problem. For this purpose, we let

$$\delta W^{\mathrm{F}} = \int_{\Omega^{\mathrm{F}}} \left(\nabla \boldsymbol{w} \cdot \boldsymbol{\sigma} \left(\boldsymbol{v}^{\mathrm{F}} \right) + \boldsymbol{w} \cdot \left(\rho^{\mathrm{F}} \dot{\boldsymbol{v}} - \rho^{\mathrm{F}} \boldsymbol{b} \right) \right) \mathrm{d}\Omega \tag{3.47}$$

$$\delta W^{\mathrm{S}} = \int_{\Omega^{\mathrm{S}}} \left(\nabla \boldsymbol{w} \cdot \boldsymbol{\sigma} \left(\boldsymbol{v}^{\mathrm{S}} \right) + \boldsymbol{w} \cdot \left(\rho^{\mathrm{S}} \dot{\boldsymbol{v}} - \rho^{\mathrm{S}} \boldsymbol{b} \right) \right) \mathrm{d}\Omega \tag{3.48}$$

$$\delta W^{\mathrm{FS}} = \int_{\Omega^{\mathrm{S}}} \left(\nabla \boldsymbol{w} \cdot \boldsymbol{\sigma} \left(\boldsymbol{v}^{\mathrm{FS}} \right) + \boldsymbol{w} \cdot \left(\rho^{\mathrm{F}} \dot{\boldsymbol{v}} - \rho^{\mathrm{F}} \boldsymbol{b} \right) \right) \mathrm{d}\Omega \tag{3.49}$$

It is easy to verify that equation (3.43) becomes

$$\delta W^{\mathrm{F}} + \delta W^{\mathrm{S}} - \delta W^{\mathrm{FS}} = 0 \tag{3.50}$$

Equation (3.50) is an alternative weak form for the coupled system.

The strong form, i.e. the Euler-Lagrange equations, is extracted by integrating (3.50) by parts, taking into account the discontinuities of the stress $\boldsymbol{\sigma}$ on Γ^{D}. This gives (after a change of sign)

$$\begin{aligned}
&\int_{\Omega^{\mathrm{S}}} \left(\boldsymbol{w} \cdot \left(\nabla \cdot \boldsymbol{\sigma}^{\mathrm{S}} \left(\boldsymbol{v}^{\mathrm{S}} \right) \right) - \boldsymbol{w} \cdot \left(\rho^{\mathrm{S}} \dot{\boldsymbol{v}} - \rho^{\mathrm{S}} \boldsymbol{b} \right) \right) \mathrm{d}\Omega \\
&+ \int_{\Omega^{\mathrm{F}}} \boldsymbol{w} \cdot \left(\nabla \cdot \boldsymbol{\sigma}^{\mathrm{F}} \left(\boldsymbol{v}^{\mathrm{F}} \right) \right) \mathrm{d}\Omega - \int_{\Omega^{\mathrm{F}}} \boldsymbol{w} \cdot \left(\rho^{\mathrm{F}} \dot{\boldsymbol{v}} - \rho^{\mathrm{F}} \boldsymbol{b} \right) \mathrm{d}\Omega \\
&- \int_{\Omega^{\mathrm{S}}} \boldsymbol{w} \cdot \left(\nabla \cdot \boldsymbol{\sigma}^{\mathrm{FS}} \left(\boldsymbol{v}^{\mathrm{FS}} \right) \right) \mathrm{d}\Omega + \int_{\Omega^{\mathrm{S}}} \boldsymbol{w} \cdot \left(\rho^{\mathrm{F}} \dot{\boldsymbol{v}} - \rho^{\mathrm{F}} \boldsymbol{b} \right) \mathrm{d}\Omega \\
&- \int_{\Gamma^{\mathrm{D}}} \boldsymbol{w} \cdot [\![\boldsymbol{\sigma} \cdot \boldsymbol{n}]\!] \mathrm{d}\Gamma \;=\; 0
\end{aligned} \tag{3.51}$$

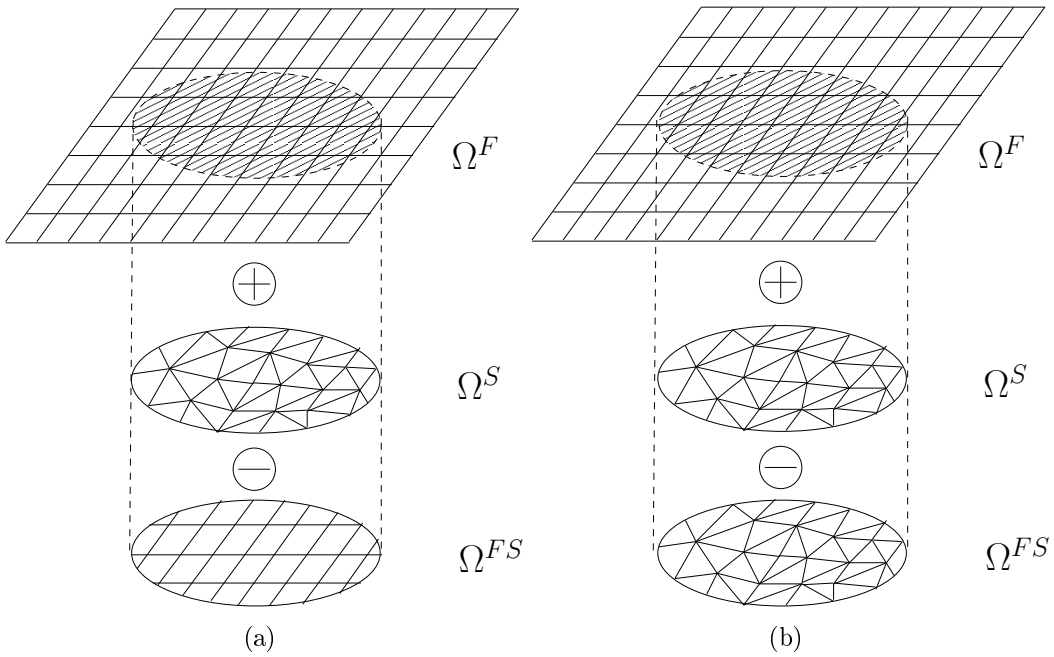

Figure 3.2. Conceptual depiction of the model: energetically, the total system consists of $\delta W^{\mathrm{F}} + \delta W^{\mathrm{S}} - \delta W^{\mathrm{F}S}$.

From the arbitrariness of the test function and the density theorem, it follows that

$$\nabla \cdot \boldsymbol{\sigma}\left(\boldsymbol{v}^{\mathrm{F}}\right) + \rho \boldsymbol{b} = \rho \dot{\boldsymbol{v}} \quad \text{in} \quad \Omega^{\mathrm{F}} \tag{3.52}$$

$$\nabla \cdot \boldsymbol{\sigma}\left(\boldsymbol{v}^{\mathrm{S}}\right) + \rho \boldsymbol{b} = \rho \dot{\boldsymbol{v}} \quad \text{in} \quad \Omega^{\mathrm{S}} \tag{3.53}$$

$$[\![\boldsymbol{\sigma} \cdot \boldsymbol{n}]\!] = 0 \quad \text{in} \quad \Gamma^{\mathrm{I}} \tag{3.54}$$

Note the tractions on Γ_τ^{F} and Γ_τ^{S} are omitted for simplicity .

The resulting conceptual model is illustrated in Figure 3.2. As is shown there, the total system consists of the fluid covering the entire domain, plus the solid, minus the fluid on the domain occupied by the solid. It is important to note that the velocities in

the three integrals in (3.47), (3.48) and (3.49) are identical fields

$$\boldsymbol{v} = \boldsymbol{v}^{\mathrm{F}} = \boldsymbol{v}^{\mathrm{S}} = \boldsymbol{v}^{\mathrm{FS}} \tag{3.55}$$

Therefore, in constructing the approximation, this identity should be observed. However, the independent variables for the velocity fields may differ. Thus it is possible to use $\boldsymbol{v}^{\mathrm{F}}(\boldsymbol{x},t)$, $\boldsymbol{v}^{\mathrm{S}}(\boldsymbol{X},t)$, $\boldsymbol{v}^{\mathrm{FS}}(\boldsymbol{x},t)$, i.e. to use an Eulerian description for the fluid and the overlaid fluid and Lagrangian descriptions for the solid .

The mass conservation equations are

$$\frac{\partial \rho}{\partial t} + \nabla \cdot (\rho \boldsymbol{v}) = 0 \qquad \text{on } \Omega/\Gamma_{\mathrm{D}} \tag{3.56}$$

$$[\![\boldsymbol{v} \cdot \boldsymbol{n}]\!] = 0 \qquad \text{on } \Gamma_{\mathrm{D}} \tag{3.57}$$

3.5.2. Discretization

We now construct a discretization with a Lagrangian description for the solid and an Eulerian description for the fluid, so we let

$$\boldsymbol{v}^{\mathrm{F}}(\boldsymbol{x},t) = \boldsymbol{v}_I(t)\, N_I^{\mathrm{F}}(\boldsymbol{x}) \tag{3.58}$$

$$\boldsymbol{v}^{\mathrm{S}}(\boldsymbol{x},t) = \boldsymbol{v}_I^{\mathrm{S}}(t)\, N_I^{\mathrm{S}}(\boldsymbol{X}) \tag{3.59}$$

where repeated indices are summed over the relevant nodes. We have now distinguished the fluid and solid velocities, but bear in mind they must be equal for the equivalence of (3.50) with the strong form to hold. There are several approaches that can be taken to construct the weight functions and enforce the equality of the velocity field.

To enforce the equality (3.55), though only approximately, we compute the solid velocities at the nodes from the fluid velocity field, so

$$\boldsymbol{v}_K^{\mathrm{S}}(t) = \boldsymbol{v}_I^{\mathrm{F}}(t) N_I^{\mathrm{F}}(\boldsymbol{x}_K) \tag{3.60}$$

Substituting (3.60) into (3.59), we obtain

$$\boldsymbol{v}^{\mathrm{S}}(\boldsymbol{x}, t) = \boldsymbol{v}_I^{\mathrm{F}}(t) N_I^{\mathrm{F}}(\boldsymbol{x}_K) N_K^{\mathrm{S}}(\boldsymbol{X}) \tag{3.61}$$

Let

$$w = \begin{cases} w_I N_I^{\mathrm{F}}(\boldsymbol{x}) & \text{in } \Omega^{\mathrm{F}} \\ w_I N_I^{\mathrm{F}}(\boldsymbol{x}_K) N_K^{\mathrm{S}}(\boldsymbol{X}) & \text{in } \Omega^{\mathrm{S}} \end{cases} \tag{3.62}$$

Substituting into (3.50) and taking advantage of the arbitrariness of w_I gives

$$\begin{aligned} \int_{\Omega^{\mathrm{F}}} \nabla N_I^{\mathrm{F}} \cdot \boldsymbol{\sigma}^{\mathrm{F}} + \int_{\Omega^{\mathrm{F}}} \left(\rho^{\mathrm{F}} N_I^{\mathrm{F}} \dot{\boldsymbol{v}} - N_I^{\mathrm{F}} \rho^{\mathrm{F}} \boldsymbol{b}\right) \mathrm{d}\Omega - \int_{\Gamma_\tau^{\mathrm{F}}} N_I^{\mathrm{F}} \boldsymbol{\tau} \mathrm{d}\Gamma \\ + N_I^{\mathrm{F}}(\boldsymbol{x}_K) \int_{\Omega^{\mathrm{S}}} \nabla N_K^{\mathrm{S}} \cdot \boldsymbol{\sigma}^{\mathrm{S}} - N_I^{\mathrm{F}}(\boldsymbol{x}_K) \int_{\Gamma_\tau^{\mathrm{S}}} N_K^{\mathrm{S}} \boldsymbol{\tau} \mathrm{d}\Gamma \\ + N_I^{\mathrm{F}}(\boldsymbol{x}_K) \int_{\Omega^{\mathrm{S}}} \rho^{\mathrm{S}} N_K^{\mathrm{S}} N_L^{\mathrm{S}} \mathrm{d}\Omega N_J^{\mathrm{F}}(\boldsymbol{x}_L) \dot{\boldsymbol{v}}_J^{\mathrm{F}} - N_I^{\mathrm{F}}(\boldsymbol{x}_K) \int_{\Omega^{\mathrm{S}}} N_K^{\mathrm{S}} \rho^{\mathrm{S}} \boldsymbol{b} \mathrm{d}\Omega \\ - \int_{\Omega^{\mathrm{S}}} \nabla N_I^{\mathrm{F}} \cdot \boldsymbol{\sigma}^{\mathrm{F}} \mathrm{d}\Omega - \int_{\Omega^{\mathrm{S}}} \left(\rho^{\mathrm{F}} N_I^{\mathrm{F}} \dot{\boldsymbol{v}} - N_I^{\mathrm{F}} \rho^{\mathrm{F}} \boldsymbol{b}\right) \mathrm{d}\Omega &= 0 \end{aligned} \tag{3.63}$$

where the nodal material fluid velocity $\dot{\boldsymbol{v}}_J^{\mathrm{F}}$ is given by

$$\begin{aligned} \dot{\boldsymbol{v}}_J^{\mathrm{F}} &= \dot{\boldsymbol{v}}^{\mathrm{F}}(\boldsymbol{x}_J, t) = N_I^{\mathrm{F}}(\boldsymbol{x}_J) \boldsymbol{v}_{I,t}^{\mathrm{F}}(t) + N_I^{\mathrm{F}}(\boldsymbol{x}_J) \boldsymbol{v}_I^{\mathrm{F}}(t) \cdot \nabla N_I^{\mathrm{F}}(\boldsymbol{x}_J) \boldsymbol{v}_I^{\mathrm{F}}(t) \\ \dot{\boldsymbol{v}}_J^{\mathrm{F}} &= \boldsymbol{v}_{J,t}^{\mathrm{F}}(t) + \boldsymbol{v}_J^{\mathrm{F}}(t) \cdot \nabla N_I^{\mathrm{F}}(\boldsymbol{x}_J) \boldsymbol{v}_I^{\mathrm{F}}(t) \end{aligned} \tag{3.64}$$

To evaluate the last two terms in (3.63), we use the technique developed in [**13**] of approximating the fluid-solid interface by an implicit function (often called a level set)

$$\phi(\boldsymbol{x}, t) = 0 \tag{3.65}$$

where $\phi(\boldsymbol{x})$ is the signed distance function and

$$\phi(\boldsymbol{x}, t) > 0 \qquad \text{in}\, \Omega^{\mathrm{F}}/\Omega^{\mathrm{S}} \tag{3.66}$$

$$\phi(\boldsymbol{x}, t) < 0 \qquad \text{in}\, \Omega^{\mathrm{S}} \tag{3.67}$$

The construction of this function is described in section 4.1.2.

Then the integrals can be written as

$$\int_{\Omega^{\mathrm{S}}} \left(\nabla N_I^{\mathrm{F}} \cdot \boldsymbol{\sigma}^{\mathrm{F}} + \rho^{\mathrm{F}} N_I^{\mathrm{F}} \dot{\boldsymbol{v}} - N_I^{\mathrm{F}} \rho^{\mathrm{F}} \boldsymbol{b}\right) \mathrm{d}\Omega = \int_{\Omega^{\mathrm{F}}} H(-\phi) \left(\nabla N_I^{\mathrm{F}} \cdot \boldsymbol{\sigma}^{\mathrm{F}} + \rho^{\mathrm{F}} N_I^{\mathrm{F}} \dot{\boldsymbol{v}} - N_I^{\mathrm{F}} \rho^{\mathrm{F}} \boldsymbol{b}\right) \mathrm{d}\Omega \tag{3.68}$$

as shown in Figure 3.3, the evaluation of the above right hand side involves integral over a domain with a boundary that is not coincident with the element edges. These integrals can be efficiently integrated for low order elements by the procedure developed by Ventura [**90**]; otherwise, the elements through which the boundary passes must be broken into sub-elements as described in [**69**] to evaluate these integrals.

The discrete momentum equation (3.63) can be written as

$$\left(\boldsymbol{M}_{IJ}^{\mathrm{F}} + \boldsymbol{M}_{IJ}^{\mathrm{S}} - \boldsymbol{M}_{IJ}^{\mathrm{FS}}\right) \dot{\boldsymbol{v}}_J - \boldsymbol{f}_I^{\mathrm{F}} - \boldsymbol{f}_I^{\mathrm{S}} + \boldsymbol{f}_I^{\mathrm{FS}} = 0 \tag{3.69}$$

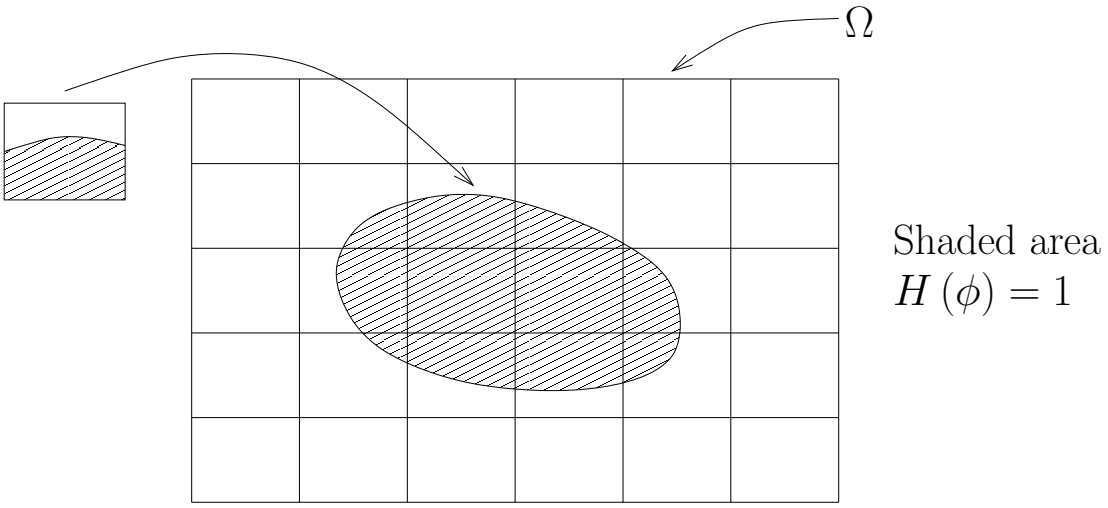

Figure 3.3. Example of a solid in a structured fluid mesh showing that only that portion of some elements that contribute to integrals of the form $\int_\Omega H(\phi) f(\boldsymbol{x}) \, \mathrm{d}\Omega$.

where

$$M_{IJ}^{\mathrm{F}} = \int_{\Omega^{\mathrm{F}}} \rho^{\mathrm{F}} N_I^{\mathrm{F}} N_J^{\mathrm{F}} \mathrm{d}\Omega \tag{3.70}$$

$$\begin{aligned} M_{IJ}^{\mathrm{S}} &= N_I(\boldsymbol{x}_K) N_J(\boldsymbol{x}_L) \int_{\Omega^{\mathrm{S}}} \rho^{\mathrm{S}} N_K^{\mathrm{S}} N_L^{\mathrm{S}} \mathrm{d}\Omega \\ &= N_I(\boldsymbol{x}_K) N_J(\boldsymbol{x}_L) \int_{\Omega_0^{\mathrm{S}}} \rho_0^{\mathrm{S}} N_K^{\mathrm{S}} N_L^{\mathrm{S}} \mathrm{d}\Omega_0 \end{aligned} \tag{3.71}$$

$$M_{IJ}^{\mathrm{FS}} = \int_{\Omega^{\mathrm{F}}} H(-\phi) \rho^{\mathrm{F}} N_I^{\mathrm{F}} N_J^{\mathrm{F}} \mathrm{d}\Omega \tag{3.72}$$

$$\boldsymbol{f}_I^{\mathrm{F}} = \int_{\Gamma_\tau^{\mathrm{F}}} N_I^{\mathrm{F}} \boldsymbol{\tau} \mathrm{d}\Gamma + \int_{\Omega^{\mathrm{F}}} \left(-\nabla N_I^{\mathrm{F}} \cdot \boldsymbol{\sigma}^{\mathrm{F}} + N_I^{\mathrm{F}} \rho^{\mathrm{F}} \boldsymbol{b} \right) \mathrm{d}\Omega - \int_{\Omega^{\mathrm{F}}} N_I^{\mathrm{F}} \rho^{\mathrm{F}} \boldsymbol{v} \cdot \nabla \boldsymbol{v} \mathrm{d}\Omega \tag{3.73}$$

$$\begin{aligned} \boldsymbol{f}_I^{\mathrm{S}} &= N_I^{\mathrm{F}}(\boldsymbol{x}_J)\int_{\Gamma_\tau^{\mathrm{S}}} N_J^{\mathrm{S}}\boldsymbol{\tau}\mathrm{d}\Gamma + N_I(\boldsymbol{x}_J)\int_{\Omega^{\mathrm{S}}}\left(-\nabla N_J^{\mathrm{S}}\cdot\boldsymbol{\sigma}^{\mathrm{S}} + N_J^{\mathrm{S}}\rho^{\mathrm{S}}\boldsymbol{b}\right)\mathrm{d}\Omega \\ &= N_I^{\mathrm{F}}(\boldsymbol{x}_J)\int_{\Gamma_{\tau 0}^{\mathrm{S}}} N_J^{\mathrm{S}}\boldsymbol{\tau}^0\mathrm{d}\Gamma + N_I^{\mathrm{F}}(\boldsymbol{x}_J)\int_{\Omega_0^{\mathrm{S}}}\left(-\nabla_0 N_J\cdot\boldsymbol{P}^{\mathrm{S}} + N_J^{\mathrm{S}}\rho_0^{\mathrm{S}}\boldsymbol{b}\right)\mathrm{d}\Omega \end{aligned} \tag{3.74}$$

$$\boldsymbol{f}_I^{\mathrm{FS}} = \int_{\Omega^{\mathrm{F}}} H(-\phi)\left(-\nabla N_I^{\mathrm{F}}\cdot\boldsymbol{\sigma}^{\mathrm{F}} + N_I^{\mathrm{F}}\rho^{\mathrm{F}}\boldsymbol{b}\right)\mathrm{d}\Omega - \int_{\Omega^{\mathrm{F}}} H(-\phi)\, N_I^{\mathrm{F}}\rho^{\mathrm{F}}\boldsymbol{v}\cdot\nabla\boldsymbol{v}\mathrm{d}\Omega \tag{3.75}$$

For convenience, we rewrite (3.69) as

$$\boldsymbol{M}\dot{\boldsymbol{v}} = \boldsymbol{f} \tag{3.76}$$

where

$$\boldsymbol{M} = \boldsymbol{M}_{IJ}^{\mathrm{F}} + \boldsymbol{M}_{IJ}^{\mathrm{S}} - \boldsymbol{M}_{IJ}^{FS} \tag{3.77}$$

$$\boldsymbol{f} = \boldsymbol{f}_I^{\mathrm{F}} + \boldsymbol{f}_I^{\mathrm{S}} - \boldsymbol{f}_I^{\mathrm{FS}} \tag{3.78}$$

On examining (3.61), (3.71) and (3.74), it can be seen that the solid nodes are treated as slave-nodes in a master/slave procedure, see [**12**, p. 183].

It is also possible to treat the fluid nodes that are within Ω^{S} as slave nodes. In that case, we let

$$\boldsymbol{v}^{\mathrm{F}}(\boldsymbol{x},t) = \boldsymbol{v}_I^{\mathrm{F}}(t)\, N_I^{\mathrm{F}}(\boldsymbol{x}) \quad \text{if} \quad \boldsymbol{x}_I \in \Omega^{\mathrm{F}}/\Omega^{\mathrm{S}} \tag{3.79}$$

$$\boldsymbol{v}^{\mathrm{F}}(\boldsymbol{x},t) = \boldsymbol{v}_I^{\mathrm{S}}(t)\, N_I^{\mathrm{S}}(\boldsymbol{x}_K)\, N_K^{\mathrm{F}}(\boldsymbol{x}) \tag{3.80}$$

$$\boldsymbol{v}^{\mathrm{S}}(\boldsymbol{X},t) = \boldsymbol{v}_I^{\mathrm{S}}(t)\, N_I^{\mathrm{S}}(\boldsymbol{X}) \tag{3.81}$$

3.5.3. Solution procedure

Equations (3.76) and (3.69) can be solved by explicit or implicit methods [**14, 64, 55, 54**]. For example, for explicit integration of (3.63), we can use the central difference method,

which relates the acceleration to the velocities by

$$\dot{\boldsymbol{v}}_J^n = \frac{\boldsymbol{v}^{n+1/2} - \boldsymbol{v}^{n-1/2}}{\Delta t} \tag{3.82}$$

The update equation is then

$$\boldsymbol{v}_I^{n+1/2} = \boldsymbol{v}^{n-1/2} + \left(\boldsymbol{M}_{IJ}^n\right)^{-1} \boldsymbol{f}_J^n \Delta t \tag{3.83}$$

The displacement of the solid nodes $\boldsymbol{u}$ is then obtained by

$$\boldsymbol{u}_I^{n+1} = \boldsymbol{u}_I^n + \Delta t \boldsymbol{v}^{n+1/2} \tag{3.84}$$

For implicit integration by the trapezoidal rule, then the equation is

$$\boldsymbol{v}^{n+1} = \boldsymbol{v}^n - \boldsymbol{A}^{-1} \left(\boldsymbol{M}\boldsymbol{v}^n - \boldsymbol{f}^n\right) \tag{3.85}$$

where $\boldsymbol{A} = \frac{\partial \boldsymbol{r}}{\partial \boldsymbol{v}_I}$ and $\boldsymbol{r} = \boldsymbol{M}\boldsymbol{v} - \boldsymbol{f}$ is the system residual.

CHAPTER 4

Fluid-Structure Interaction By The Constraint Method

4.1. INTRODUCTION

4.1.1. Weak form

Define the test and trial function spaces

$$\mathscr{U}_0 = \{\boldsymbol{w} | \boldsymbol{w} \in \mathscr{H}^1, \boldsymbol{w} = 0 \text{ on } \Gamma_u\} \tag{4.1}$$

$$\mathscr{U} = \{\boldsymbol{v} | \boldsymbol{v} \in \mathscr{H}^1, \boldsymbol{v} = v_0 \text{ on } \Gamma_u\} \tag{4.2}$$

$$\mathscr{U}^\lambda = \{\boldsymbol{\lambda} | \boldsymbol{\lambda} \in \mathscr{L}_2\} \tag{4.3}$$

the weak form is: find $\left(\boldsymbol{v}^{\mathrm{F}}, \boldsymbol{v}^{\mathrm{S}}, \boldsymbol{\lambda}\right) \in \left(\mathscr{U} \times \mathscr{U} \times \mathscr{U}^\lambda\right)$

$$\begin{aligned} &\int_{\Omega^{\mathrm{F}}} \left(\boldsymbol{w}^{\mathrm{F}} \cdot \rho^{\mathrm{F}} \boldsymbol{b}^{\mathrm{F}} - \boldsymbol{w}^{\mathrm{F}} \cdot \dot{\boldsymbol{v}}^{\mathrm{F}} \rho^{\mathrm{F}} - \nabla \boldsymbol{w}^{\mathrm{F}} : \boldsymbol{\sigma}^{\mathrm{F}}\right) H(\phi) \, \mathrm{d}\Omega + \int_{\Gamma_\tau^{\mathrm{F}}} \boldsymbol{w}^{\mathrm{F}} \cdot \boldsymbol{\tau}^{\mathrm{F}} \mathrm{d}\Gamma \\ &+ \int_{\Omega^{\mathrm{F}}} \left(\boldsymbol{w}^{\mathrm{S}} \cdot \rho^{\mathrm{S}} \boldsymbol{b}^{\mathrm{S}} - \boldsymbol{w}^{\mathrm{S}} \cdot \dot{\boldsymbol{v}}^{\mathrm{S}} \rho^{\mathrm{S}} - \nabla \boldsymbol{w}^{\mathrm{S}} : \boldsymbol{\sigma}^{\mathrm{S}}\right) H(-\phi) \, \mathrm{d}\Omega + \int_{\Gamma_\tau^{\mathrm{S}}} \boldsymbol{w}^{\mathrm{S}} \cdot \boldsymbol{\tau}^{\mathrm{S}} \mathrm{d}\Gamma \\ &+ s_1 \delta \int_{\Gamma^{\mathrm{I}}} \boldsymbol{\lambda} \cdot \left(\boldsymbol{v}^{\mathrm{F}} - \boldsymbol{v}^{\mathrm{S}}\right) \mathrm{d}\Gamma + s_2 \frac{\beta}{2} \delta \int_{\Gamma^{\mathrm{I}}} \left(\boldsymbol{v}^{\mathrm{F}} - \boldsymbol{v}^{\mathrm{S}}\right)^2 \mathrm{d}\Gamma \\ &= 0 \end{aligned} \tag{4.4}$$

$\forall \left(\boldsymbol{w}^{\mathrm{F}}, \boldsymbol{w}^{\mathrm{S}}, \delta\boldsymbol{\lambda}\right) \in \left(\mathscr{U}_0 \times \mathscr{U}_0 \times \mathscr{U}^\lambda\right)$ where s_1 and s_2 are two switches to choose different constraint methods. Their meanings are listed in Table 4.1. Another possible constraint method is Nitsche's method [**72**].

Table 4.1. Switches for choice of constraint method.

switch s_1	switch s_2	constraint method
1	0	Lagrange multiplier
0	1	penalty
1	1	augmented Lagrangian

In Cartesian's component form, the weak form is

$$I + C = F^{\mathrm{F}} + F^{\mathrm{S}} \tag{4.5}$$

where

$$I = \int_{\Omega^{\mathrm{F}}} \delta v_i^{\mathrm{F}} \rho^{\mathrm{F}} v_{i,t}^{\mathrm{F}} H(\phi) \mathrm{d}\Omega + \int_{\Omega^{\mathrm{F}}} \delta v_i^{\mathrm{S}} \rho^{\mathrm{S}} \dot{v}_i^{\mathrm{S}} H(-\phi) \mathrm{d}\Omega \tag{4.6}$$

$$\begin{aligned} C &= -s_1 \int_{\Gamma^{\mathrm{I}}} \delta\lambda_i (v_i^{\mathrm{F}} - v_i^{\mathrm{S}}) \mathrm{d}\Gamma - s_1 \int_{\Gamma^{\mathrm{I}}} \lambda_i (\delta v_i^{\mathrm{F}} - \delta v_i^{\mathrm{S}}) \mathrm{d}\Gamma \\ &\quad -s_2 \beta \int_{\Gamma^{\mathrm{I}}} (\delta v_i^{\mathrm{F}} - \delta v_i^{\mathrm{S}})(v_i^{\mathrm{F}} - v_i^{\mathrm{S}}) \mathrm{d}\Gamma \end{aligned} \tag{4.7}$$

$$\begin{aligned} F^{\mathrm{F}} &= -\int_{\Omega^{\mathrm{F}}} \delta v_i^{\mathrm{F}} \rho^{\mathrm{F}} v_j^{\mathrm{F}} v_{i,j}^{\mathrm{F}} H(\phi) \mathrm{d}\Omega - \int_{\Omega^{\mathrm{F}}} \delta v_{i,j}^{\mathrm{F}} \sigma_{ij}^{\mathrm{F}} H(\phi) \mathrm{d}\Omega \\ &\quad + \int_{\Omega^{\mathrm{F}}} \delta v_i^{\mathrm{F}} \rho^{\mathrm{F}} b_i^{\mathrm{F}} H(\phi) \mathrm{d}\Omega + \int_{\Gamma_\tau^{\mathrm{F}}} \delta v_i^{\mathrm{F}} \tau_i^{\mathrm{F}} \mathrm{d}\Gamma \end{aligned} \tag{4.8}$$

$$F^{\mathrm{S}} = -\int_{\Omega^{\mathrm{S}}} \delta v_{i,j}^{\mathrm{S}} \sigma_{ij}^{\mathrm{S}} H(-\phi) \mathrm{d}\Omega + \int_{\Omega^{\mathrm{S}}} \delta v_i^{\mathrm{S}} \rho^{\mathrm{S}} b_i^{\mathrm{S}} H(-\phi) \mathrm{d}\Omega + \int_{\Gamma_\tau^{\mathrm{S}}} \delta v_i^{\mathrm{S}} \tau_i^{\mathrm{S}} \mathrm{d}\Gamma \tag{4.9}$$

The equivalence to the strong form is briefly shown below. To distinguish the domains occupied respectively by the solid and fluid, Ω^{CD} is used to denote the whole computational

domain. Note first that

$$\begin{aligned}\int_{\Omega^{\mathrm{CD}}} \delta v_{i,j}^{\mathrm{F}} \sigma_{ij}^{\mathrm{F}} H(\phi) \mathrm{d}\Omega &= \int_{\Omega^{\mathrm{F}}} \delta v_{i,j}^{\mathrm{F}} \sigma_{ij}^{\mathrm{F}} \mathrm{d}\Omega \\ = \int_{\Gamma_\tau^{\mathrm{F}}} \delta v_i^{\mathrm{F}} \sigma_{ij}^{\mathrm{F}} n_j^{\mathrm{F}} \mathrm{d}\Gamma &+ \int_{\Gamma^{\mathrm{I}}} \delta v_i^{\mathrm{F}} \sigma_{ij}^{\mathrm{F}} n_j^{\mathrm{F}} \mathrm{d}\Gamma - \int_{\Omega^{\mathrm{F}}} \delta v_i^{\mathrm{F}} \sigma_{ij,j}^{\mathrm{F}} \mathrm{d}\Omega \end{aligned} \tag{4.10}$$

$$\begin{aligned}\int_{\Omega^{\mathrm{CD}}} \delta v_{i,j}^{\mathrm{S}} \sigma_{ij}^{\mathrm{S}} H(-\phi) \mathrm{d}\Omega &= \int_{\Omega^{\mathrm{S}}} \delta v_{i,j}^{\mathrm{S}} \sigma_{ij}^{\mathrm{S}} \mathrm{d}\Omega \\ = \int_{\Gamma_\tau^{\mathrm{S}}} \delta v_i^{\mathrm{S}} \sigma_{ij}^{\mathrm{S}} n_j^{\mathrm{S}} \, \mathrm{d}\Gamma &+ \int_{\Gamma^{\mathrm{I}}} \delta v_i^{\mathrm{S}} \sigma_{ij}^{\mathrm{S}} n_j^{\mathrm{S}} \, \mathrm{d}\Gamma - \int_{\Omega^{\mathrm{S}}} \delta v_i^{\mathrm{S}} \sigma_{ij,j}^{\mathrm{S}} \, \mathrm{d}\Omega \end{aligned} \tag{4.11}$$

Substituting equations (4.10) and (4.11) into the weak form (4.4), we obtain

$$\begin{aligned} 0 = & \int_{\Omega^{\mathrm{CD}}} \delta v_i^{\mathrm{F}} (\rho^{\mathrm{F}} b_i^{\mathrm{F}} - \rho^{\mathrm{F}} \dot{v}_i^{\mathrm{F}}) H(\phi) \mathrm{d}\Omega + \int_{\Omega^{\mathrm{CD}}} \delta v_i^{\mathrm{S}} (\rho^{\mathrm{S}} b_i^{\mathrm{S}} - \rho^{\mathrm{S}} \dot{v}_i^{\mathrm{S}}) H(-\phi) \mathrm{d}\Omega \\ & - \left(\int_{\Gamma_\tau^{\mathrm{F}}} \delta v_i^{\mathrm{F}} \sigma_{ij}^{\mathrm{F}} n_j^{\mathrm{F}} \mathrm{d}\Gamma + \int_{\Gamma^{\mathrm{I}}} \delta v_i^{\mathrm{F}} \sigma_{ij}^{\mathrm{F}} n_j^{\mathrm{F}} \mathrm{d}\Gamma - \int_{\Omega^{\mathrm{F}}} \delta v_i^{\mathrm{F}} \sigma_{ij,j}^{\mathrm{F}} \mathrm{d}\Omega \right) \\ & - \left(\int_{\Gamma_\tau^{\mathrm{S}}} \delta v_i^{\mathrm{S}} \sigma_{ij}^{\mathrm{S}} n_j^{\mathrm{S}} \mathrm{d}\Gamma + \int_{\Gamma^{\mathrm{I}}} \delta v_i^{\mathrm{S}} \sigma_{ij}^{\mathrm{S}} n_j^{\mathrm{S}} \mathrm{d}\Gamma - \int_{\Omega^{\mathrm{S}}} \delta v_i^{\mathrm{S}} \sigma_{ij,j}^{\mathrm{S}} \mathrm{d}\Omega \right) \\ & + \int_{\Gamma_\tau^{\mathrm{F}}} \delta v_i^{\mathrm{F}} \tau_i^{\mathrm{F}} \mathrm{d}\Gamma + \int_{\Gamma_\tau^{\mathrm{S}}} \delta v_i^{\mathrm{S}} \tau_i^{\mathrm{S}} \mathrm{d}\Gamma + s_1 \int_{\Gamma^{\mathrm{I}}} \delta \lambda_i (v_i^{\mathrm{F}} - v_i^{\mathrm{S}}) \mathrm{d}\Gamma \\ & + \int_{\Gamma^{\mathrm{I}}} (\delta v_i^{\mathrm{F}} - \delta v_i^{\mathrm{S}}) \left(s_1 \lambda_i + s_2 \beta (v_i^{\mathrm{F}} - v_i^{\mathrm{S}}) \right) \mathrm{d}\Gamma \end{aligned} \tag{4.12}$$

Reorganizing (4.12) by collecting the integrals on the same domain, we obtain

$$
\begin{aligned}
0 \;=\; & \int_{\Omega^{\mathrm{CD}}} \delta v_i^{\mathrm{F}} (\rho^{\mathrm{F}} b_i^{\mathrm{F}} - \rho^{\mathrm{F}} \dot{v}_i^{\mathrm{F}} + \sigma_{ij,j}^{\mathrm{F}}) H(\phi) \mathrm{d}\Omega - \int_{\Gamma_\tau^{\mathrm{F}}} \delta v_i^{\mathrm{F}} (\sigma_{ij}^{\mathrm{F}} n_j^{\mathrm{F}} - \tau_i^{\mathrm{F}}) \mathrm{d}\Gamma \\
& + \int_{\Omega^{\mathrm{CD}}} \delta v_i^{\mathrm{S}} (\rho^{\mathrm{S}} b_i^{\mathrm{S}} - \rho^{\mathrm{S}} \dot{v}_i^{\mathrm{S}} + \sigma_{ij,j}^{\mathrm{S}}) H(-\phi) \mathrm{d}\Omega - \int_{\Gamma_\tau^{\mathrm{S}}} \delta v_i^{\mathrm{S}} (\sigma_{ij}^{\mathrm{S}} n_j^{\mathrm{S}} - \tau_i^{\mathrm{S}}) \mathrm{d}\Gamma \\
& + \int_{\Gamma^{\mathrm{I}}} \delta v_i^{\mathrm{F}} \left(-\sigma_{ij}^{\mathrm{F}} n_j^{\mathrm{F}} - s_1 \lambda_i + s_2 \beta (v_i^{\mathrm{F}} - v_i^{\mathrm{S}}) \right) \mathrm{d}\Gamma \\
& + \int_{\Gamma^{\mathrm{I}}} \delta v_i^{\mathrm{S}} \left(-\sigma_{ij}^{\mathrm{S}} n_j^{\mathrm{S}} - s_1 \lambda_i - s_2 \beta (v_i^{\mathrm{F}} - v_i^{\mathrm{S}}) \right) \mathrm{d}\Gamma \\
& + s_1 \int_{\Gamma^{\mathrm{I}}} \delta \lambda_i (v_i^{\mathrm{F}} - v_i^{\mathrm{S}}) \mathrm{d}\Gamma
\end{aligned} \tag{4.13}
$$

From the arbitrariness of the test function and the density theorem, it follows that

$$
\begin{aligned}
\rho^{\mathrm{F}} \dot{v}_i^{\mathrm{F}} - b_i^{\mathrm{F}} - \sigma_{ij,j}^{\mathrm{F}} &= 0 \quad \text{in} \quad \Omega^{\mathrm{F}} \\
\sigma_{ij}^{\mathrm{F}} n_j^{\mathrm{F}} &= \tau_i^{\mathrm{F}} \quad \text{on} \quad \Gamma_\tau^{\mathrm{F}} \\
\rho^{\mathrm{S}} \dot{v}_i^{\mathrm{S}} - b_i^{\mathrm{S}} - \sigma_{ij,j}^{\mathrm{S}} &= 0 \quad \text{in} \quad \Omega^{\mathrm{S}} \\
\sigma_{ij}^{\mathrm{S}} n_j^{\mathrm{S}} &= \tau_i^{F} \quad \text{on} \quad \Gamma_\tau^{\mathrm{S}} \\
v_i^{\mathrm{F}} - v_i^{S} &= 0 \quad \text{on} \quad \Gamma^{\mathrm{I}} \\
-\sigma_{ij}^{\mathrm{F}} n_j^{\mathrm{F}} + s_1 \lambda_i + s_2 \beta (v_i^{\mathrm{F}} - v_i^{\mathrm{S}}) &= 0 \quad \text{on} \quad \Gamma^{\mathrm{I}} \\
\sigma_{ij}^{\mathrm{S}} n_j^{\mathrm{S}} + s_1 \lambda_i + s_2 \beta (v_i^{\mathrm{F}} - v_i^{\mathrm{S}}) &= 0 \quad \text{on} \quad \Gamma^{\mathrm{I}}
\end{aligned} \tag{4.14}
$$

The last 3 equations of (4.14) are the continuity condition and the balance of the momentum on the interface.

$$
v_i^{\mathrm{F}} - v_i^{S} = 0 \tag{4.15}
$$

$$
\sigma_{ij}^{\mathrm{S}} n_j^{\mathrm{S}} = -\sigma_{ij}^{\mathrm{F}} n_j^{\mathrm{F}} \tag{4.16}
$$

Although the no-slip interface is developed here, the derivation is similar for a slip interface.

4.1.2. Level set description of the interface

The interface Γ^{I} between the two domains is defined by the level set function (or implicit function):

$$\Gamma^{\mathrm{I}} = \left\{ \boldsymbol{x} \in \Omega^{\mathrm{CD}} | \phi\left(\boldsymbol{x}, t\right) = 0 \right\} \tag{4.17}$$

Thus $\phi\left(\boldsymbol{x}, t\right) = 0$ corresponds to the interface as shown in Figure 3.1. Furthermore, we specify that:

$$\begin{aligned} \phi\left(\boldsymbol{x}, t\right) &> 0 \qquad \text{in the fluid domain,} \\ \phi\left(\boldsymbol{x}, t\right) &< 0 \qquad \text{in the solid domain.} \end{aligned} \tag{4.18}$$

and that $\phi\left(\boldsymbol{x}, t\right)$ is a signed distance function. The signed distance is defined by:

$$\phi\left(\boldsymbol{x}, t\right) = \min_{\bar{\boldsymbol{x}}(t) \in \Gamma^{\mathrm{I}}} \parallel \boldsymbol{x} - \bar{\boldsymbol{x}}\left(t\right) \parallel \operatorname{sign}\left(\boldsymbol{n}^{\mathrm{S}} \cdot \left(\boldsymbol{x} - \bar{\boldsymbol{x}}\left(t\right)\right)\right) \tag{4.19}$$

so it is the distance to the orthogonal projection of $\boldsymbol{x}$ on Γ^{I}. Level set functions other than the signed distance function can also be used. The normal to the solid is given by:

$$n_i^{\mathrm{S}} = \phi_{,i} \quad \text{or} \quad \boldsymbol{n}^{\mathrm{S}} = \nabla \phi \tag{4.20}$$

where the notation $\bullet_{,j}$ denotes a derivative with respect to x_j; the above relation is not normalized in a theoretical description since the gradient of a signed distance function is

a unit normal; in computations, it must be normalized since it seldom equals the gradient precisely. The normal to the fluid is given by $\boldsymbol{n}^{\mathrm{F}} = -\boldsymbol{n}^{\mathrm{S}}$.

4.1.3. Discretization

Define

$$\boldsymbol{f}^{\mathrm{F-adv}} = \int_{\Omega^{\mathrm{F}}} \delta v_i^{\mathrm{F}} \rho^{\mathrm{F}} v_j^{\mathrm{F}} v_{i,j}^{\mathrm{F}} H(\phi) \mathrm{d}\Omega \tag{4.21}$$

$$\boldsymbol{f}^{\mathrm{F-ext}} = \int_{\Omega^{\mathrm{F}}} \delta v_i^{\mathrm{F}} b_i^{\mathrm{F}} H(\phi) \mathrm{d}\Omega + \int_{\Gamma_\tau^{\mathrm{F}}} \delta v_i^{\mathrm{F}} \tau_i^{\mathrm{F}} \mathrm{d}\Gamma \tag{4.22}$$

$$\boldsymbol{f}^{\mathrm{F-int}} = \int_{\Omega^{\mathrm{F}}} \delta v_{i,j}^{\mathrm{F}} \sigma_{ij}^{\mathrm{F}} H(\phi) \mathrm{d}\Omega \tag{4.23}$$

$$\boldsymbol{f}^{\mathrm{F}} = \boldsymbol{f}^{\mathrm{F-ext}} - \boldsymbol{f}^{\mathrm{F-adv}} - \boldsymbol{f}^{\mathrm{F-int}} \tag{4.24}$$

$$\boldsymbol{f}^{\mathrm{S}} = \int_{\Omega^{\mathrm{F}}} \delta v_i^{\mathrm{S}} b_i^{\mathrm{S}} H(-\phi) \mathrm{d}\Omega + \int_{\Gamma_\tau^{\mathrm{S}}} \delta v_i^{\mathrm{S}} \tau_i^{\mathrm{S}} \mathrm{d}\Gamma - \int_{\Omega^{\mathrm{F}}} \delta v_{i,j}^{\mathrm{S}} \sigma_{ij}^{\mathrm{S}} H(-\phi) \mathrm{d}\Omega \tag{4.25}$$

$$M_{IJ}^{\mathrm{F}} = \int_{\Omega^{\mathrm{F}}} \rho^{\mathrm{F}}\left(\boldsymbol{x}, t\right) N_I^{\mathrm{F}}\left(\boldsymbol{x}\right) N_J^{\mathrm{F}}\left(\boldsymbol{x}\right) H\left(\phi\right) \mathrm{d}\Omega \tag{4.26}$$

$$M_{IJ}^{\mathrm{S}} = \int_{\Omega_0^{\mathrm{F}}} \rho_0^{\mathrm{S}}\left(\boldsymbol{X}, t\right) N_I^{\mathrm{S}}\left(\boldsymbol{X}\right) N_J^{\mathrm{S}}\left(\boldsymbol{X}\right) H\left(\phi\right) \mathrm{d}\Omega_0 \tag{4.27}$$

$$M_{IJ}^{\mathrm{FF}} = \int_{\Gamma^{\mathrm{I}}} N_I^{\mathrm{F}} N_J^{\mathrm{F}} \mathrm{d}\Gamma \tag{4.28}$$

$$M_{IJ}^{\mathrm{SS}} = \int_{\Gamma^{\mathrm{I}}} N_I^{\mathrm{S}} N_J^{\mathrm{S}} \mathrm{d}\Gamma \tag{4.29}$$

$$M_{IJ}^{\mathrm{FS}} = \int_{\Gamma^{\mathrm{I}}} N_I^{\mathrm{F}} N_J^{\mathrm{S}} \mathrm{d}\Gamma \qquad \boldsymbol{M}^{\mathrm{SF}} = \left(\boldsymbol{M}^{\mathrm{FS}}\right)^T \tag{4.30}$$

$$M_{IJ}^{\lambda\mathrm{S}} = \int_{\Gamma^{\mathrm{I}}} N_I^{\lambda} N_J^{\mathrm{S}} \mathrm{d}\Gamma \qquad \boldsymbol{M}^{\mathrm{S}\lambda} = \left(\boldsymbol{M}^{\lambda\mathrm{S}}\right)^T \tag{4.31}$$

$$M_{IJ}^{\lambda\mathrm{F}} = \int_{\Gamma^{\mathrm{I}}} N_I^{\lambda} N_J^{\mathrm{F}} \mathrm{d}\Gamma \qquad \boldsymbol{M}^{\mathrm{F}\lambda} = \left(\boldsymbol{M}^{\lambda\mathrm{F}}\right)^T \tag{4.32}$$

where $(\bullet)^T$ is the transpose operation. If the forward Euler scheme is used along time, the final discretized equation is

$$\begin{pmatrix} -s_2\beta \bigtriangleup t\, \boldsymbol{M}^{\mathrm{FF}} & s_2\beta \bigtriangleup t\, \boldsymbol{M}^{\mathrm{FS}} & -s_1 \bigtriangleup t\, \boldsymbol{M}^{\mathrm{F}\lambda} \\ s_2\beta \bigtriangleup t\, \boldsymbol{M}^{\mathrm{SF}} & -s_2\beta \bigtriangleup t\, \boldsymbol{M}^{\mathrm{SS}} & s_1 \bigtriangleup t\, \boldsymbol{M}^{\mathrm{S}\lambda} \\ -s_1 \bigtriangleup t\, \boldsymbol{M}^{\lambda\mathrm{F}} & s_1 \bigtriangleup t\, \boldsymbol{M}^{\lambda\mathrm{S}} & \mathbf{0} \end{pmatrix} \begin{pmatrix} \boldsymbol{v}^{\mathrm{F},n+1} \\ \boldsymbol{v}^{\mathrm{S},n+1} \\ \boldsymbol{\lambda} \end{pmatrix} + \begin{pmatrix} \boldsymbol{M}^{\mathrm{F}} & \mathbf{0} & \mathbf{0} \\ \mathbf{0} & \boldsymbol{M}^{\mathrm{S}} & \mathbf{0} \\ \mathbf{0} & \mathbf{0} & \mathbf{0} \end{pmatrix} \begin{pmatrix} \boldsymbol{v}^{\mathrm{F},n+1} - \boldsymbol{v}^{\mathrm{F},n} \\ \boldsymbol{v}^{\mathrm{S},n+1} - \boldsymbol{v}^{\mathrm{S},n} \\ \boldsymbol{\lambda} \end{pmatrix} = \begin{pmatrix} \bigtriangleup t\, \boldsymbol{f}^{\mathrm{F}} \\ \bigtriangleup t\, \boldsymbol{f}^{\mathrm{S}} \\ \mathbf{0} \end{pmatrix} \tag{4.33}$$

Note the terms M_{IJ}^{FF}, M_{IJ}^{SS}, M_{IJ}^{FS}, $M_{IJ}^{\lambda\mathrm{S}}$, $M_{IJ}^{\lambda\mathrm{F}}$ in the first term in equation (4.33) are integrals on the interface which is a curve in 2D and a surface in 3D.

4.1.4. Interface integration

A possible interface integration for 2D problems is described here. The interface in 2D is a curve defined by the boundary of the solid, the solid field on the interface will be piece-wise linear on each line segment. Since the position of the solid is independent to the fluid, the loci of the interface relative to a fluid element will be arbitrary.

Figure 4.1 shows one possible configuration. A, B, C, D are nodes in the fluid mesh which compose one fluid element while E, F, G, H are nodes in the solid mesh. The segments $\overline{EF}$, $\overline{FG}$ and $\overline{GH}$ represent the interface which are line elements forming part of the solid boundary. The points P_i represent the intersection points between the line elements and the edges of the quadrilaterals for the fluid. q_i represent the quadrature points used in the curve quadrature. We need first find those intersection points P_i.

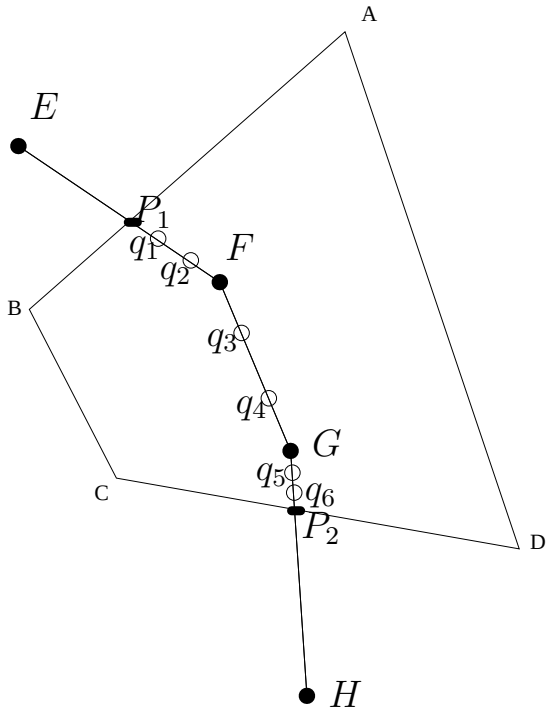

Figure 4.1. Curve integration in 2D.

Then the interface is divided into small segments among the solid nodes, i.e. E, F, G, H and those intersection points like P_1, P_2. On each segment, the quadrature points, i.e. q_i are located. For each q_i, the specific elements of the fluid and solid are identified which supplies the interpolation information for the quadrature point q_i. After obtaining the parent coordinates for the quadrature point q_i for its corresponding fluid and solid elements, the numerical integration is carried out. For 3D problems, the procedure will be similar.

4.2. WEAK FORM

A key step in the following development is the characterization of the interface by a regularized step function and its derivative, the Dirac delta function. This is the same

methodology presented in SXFEM by Belytschko et al [**16, 17**]. In this approach, a weak form is developed on the domain that is completely equivalent to the strong form as shown in section 4.1.1. The derivative of the step function is the Dirac delta function D. The Dirac function $D(\boldsymbol{x})$ has the property that for an arbitrary function $f(\boldsymbol{x})$:

$$\int_{\Omega} f(\boldsymbol{x}) D(\phi(\boldsymbol{x})) \mathrm{d}\Omega = \int_{\Gamma^{\mathrm{I}}} f(\boldsymbol{x}) \mathrm{d}\Gamma \tag{4.34}$$

Therefore we have the identity

$$\int_{\Omega} f(\boldsymbol{x}) \nabla H(\phi) \mathrm{d}\Omega = \int_{\Omega} f(\boldsymbol{x}) D(\phi) n_i \mathrm{d}\Omega = \int_{\Gamma^{\mathrm{I}}} f(\boldsymbol{x}) n_i \mathrm{d}\Gamma \tag{4.35}$$

Note here we have used $\nabla H(\phi(\boldsymbol{x})) = H_{,\phi} \nabla\phi = D(\phi) n_i$. The Dirac function is then regularized for numerical implementation.

The weak form is given by

$$\text{for } u \in \mathscr{U}, \text{ and } \lambda \in C^0,$$

$$\begin{aligned} 0 \;=\; & \int_{\Omega^{\mathrm{F}}} \left(\nabla\delta\boldsymbol{v}^{\mathrm{F}} : \boldsymbol{\sigma}^{\mathrm{F}} + \delta\boldsymbol{v}^{\mathrm{F}} \cdot \left(\dot{\boldsymbol{v}}^{\mathrm{F}} - \boldsymbol{b} \right) \rho^{\mathrm{F}} \right) H(\phi) \mathrm{d}\Omega + \int_{\Gamma^{\mathrm{F}}_{\tau}} \delta\boldsymbol{v}^{\mathrm{F}} \cdot \boldsymbol{\tau}^{\mathrm{F}} \mathrm{d}\Gamma \\ & + \int_{\Omega^{\mathrm{S}}} \left(\nabla\delta\boldsymbol{v}^{\mathrm{S}} : \boldsymbol{\sigma}^{\mathrm{S}} + \delta\boldsymbol{v}^{\mathrm{S}} \cdot \left(\dot{\boldsymbol{v}}^{\mathrm{S}} - \boldsymbol{b} \right) \rho^{\mathrm{S}} \right) \mathrm{d}\Omega + \int_{\Gamma^{\mathrm{S}}_{\tau}} \delta\boldsymbol{v}^{\mathrm{S}} \cdot \boldsymbol{\tau}^{\mathrm{S}} \mathrm{d}\Gamma \\ & + \delta \int_{\Omega^{\mathrm{F}}} D(\phi) \boldsymbol{\lambda} \cdot \left(\boldsymbol{v}^{\mathrm{F}} - \boldsymbol{v}^{\mathrm{S}} \right) \mathrm{d}\Omega, \qquad \forall \delta\boldsymbol{v} \in \mathscr{U}_0, \delta\lambda \in C^0 \end{aligned} \tag{4.36}$$

It has been shown that the above yields the strong form.

For application of the weak form, we regularize the Dirac delta function by using the following

$$D(\phi) \sim w(\phi) \tag{4.37}$$

where $w(\phi)$ is a smooth weight function (we can also call it a window function) that is normalized so that

$$\int_{-\infty}^{\infty} w(x)\, dx = 1 \tag{4.38}$$

Several examples of the regularized function are shown in Figure 4.2. We have used spline for the weight functions. The cubic symmetric weight function is given by

$$w(r) = \begin{cases} \frac{2}{3} - 4r^2 + 4r^3 & \text{for } 0 \le r \le \frac{1}{2} \\ \frac{4}{3} - 4r + 4r^2 - \frac{4}{3}r^3 & \text{for } \frac{1}{2} < r \le 1 \\ 0 & \text{for } 1 < r \end{cases} \tag{4.39}$$

$$r = \frac{1}{d_{\text{reg}}} \|\boldsymbol{x} - \bar{\boldsymbol{x}}(t)\| \quad , \bar{\boldsymbol{x}}(t) \in \Gamma^{\text{I}} \tag{4.40}$$

where d_{reg} is the width of the regularization domain and $\bar{\boldsymbol{x}}$ is the projection of $\boldsymbol{x}$ on Γ^{I}. A similar method was used in Belytschko et al [**16, 8**].

4.3. DISCRETIZATION

The discretization is performed with standard finite element interpolants N_I by

$$\boldsymbol{v}^{\text{F}}(\boldsymbol{x}, t) = N_I^{\text{F}}(\boldsymbol{x})\, \boldsymbol{v}_I^{\text{F}}(t)\, H(\phi) \tag{4.41}$$

$$\boldsymbol{u}^{\text{S}}(\boldsymbol{X}, t) = N_I^{\text{S}}(\boldsymbol{X})\, \boldsymbol{u}_I^{\text{S}}(t) \tag{4.42}$$

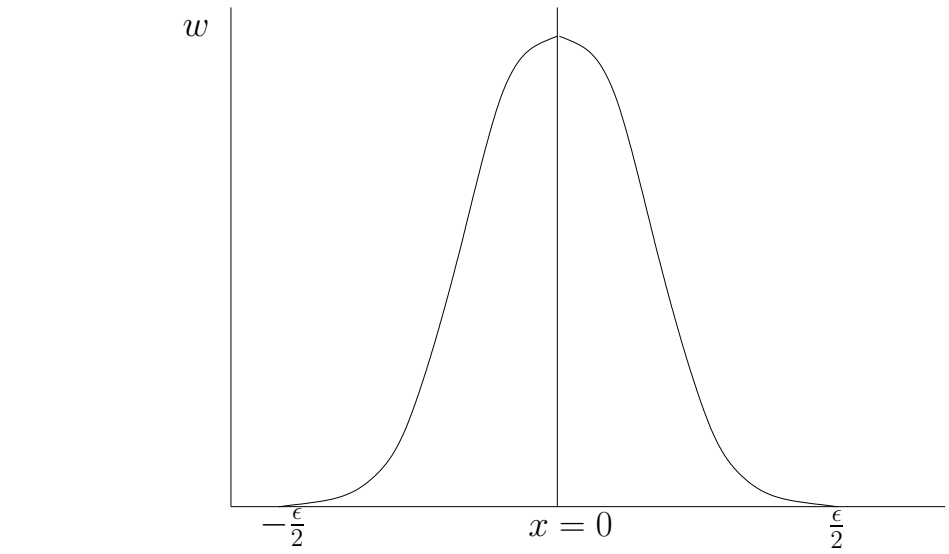

(a) Symmetric.

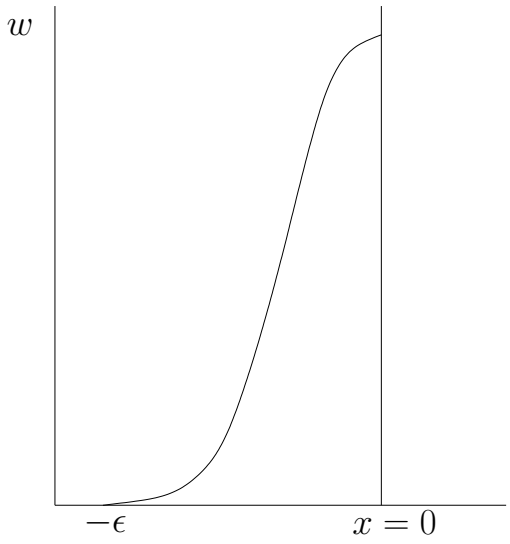

(b) Structure biased.

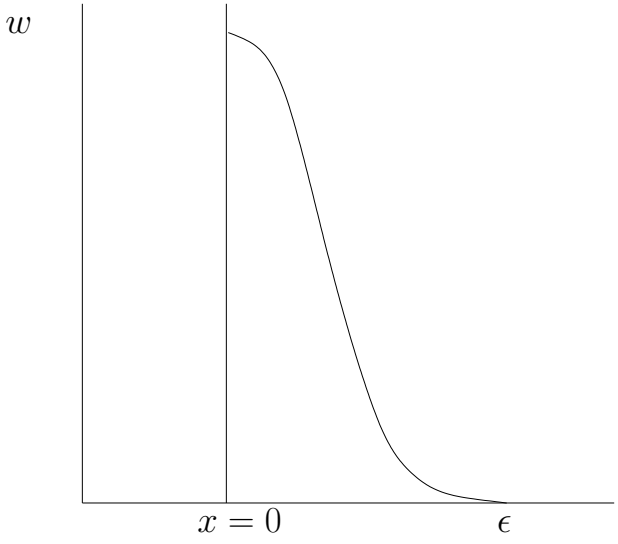

(c) Fluid biased.

Figure 4.2. Cubic spline functions for the regularization of the Dirac delta function.

where repeated upper case indices in the above and henceforth are summed over the appropriate set of nodes. Note that the motion of the solid is described by the displacement field in terms of the Lagrangian coordinates, whereas the motion of the fluid is described

by the velocity field in terms of the Eulerian (spatial) coordinates. The test functions, or variations, are approximated by the same interpolants

$$\delta \boldsymbol{v}^{\mathrm{F}}(\boldsymbol{x}) = N_I^{\mathrm{F}}(\boldsymbol{x})\, \delta \boldsymbol{v}_I^{\mathrm{F}} H(\phi) \tag{4.43}$$

$$\delta \boldsymbol{u}^{\mathrm{S}}(\boldsymbol{X}) = N_I^{\mathrm{S}}(\boldsymbol{X})\, \delta \boldsymbol{u}_I^{\mathrm{S}} \tag{4.44}$$

The fluid density is approximated by

$$\rho^{\mathrm{F}}(\boldsymbol{x}, t) = N_I^{\mathrm{F}}(\boldsymbol{x})\, \rho_I^{\mathrm{F}}(t)\, H(\phi) \tag{4.45}$$

The discrete momentum equations are

$$\begin{aligned} \int_{\Omega^{\mathrm{F}}} \left(-N_{I,j}^{\mathrm{F}}(\boldsymbol{x})\, \sigma_{ij}^{\mathrm{F}} - \rho^{\mathrm{F}} \left(N_I^{\mathrm{F}}(\boldsymbol{x})\, \dot{v}_i^{\mathrm{F}}(\boldsymbol{x}, t) - b_i\right)\right) H(\phi)\, \mathrm{d}\Omega & \\ + \int_{\Gamma_\tau^{\mathrm{F}}} N_I^{\mathrm{F}}(\boldsymbol{x})\, \tau_i^{\mathrm{F}} \mathrm{d}\Gamma + \int_{\Omega^{\mathrm{F}}} N_I^{\mathrm{F}}(\boldsymbol{x})\, \lambda w(\phi)\, \mathrm{d}\Omega &= 0 \end{aligned} \tag{4.46}$$

$$\begin{aligned} \int_{\Omega_0^{\mathrm{S}}} \left(-N_{I,j}^{\mathrm{S}}(\boldsymbol{X})\, \sigma_{ij}^{\mathrm{S}} - \rho_0 \left(N_I^{\mathrm{S}}(\boldsymbol{X})\, N_J^{\mathrm{S}}(\boldsymbol{X})\, \dot{v}_{Ji}^{\mathrm{S}} - b_i\right)\right) \mathrm{d}\Omega_0 & \\ + \int_{\Gamma_\tau^{\mathrm{S}}} N_I^{\mathrm{S}}(\boldsymbol{X})\, \tau_i^{\mathrm{S}} \mathrm{d}\Gamma - \int_{\Omega^{\mathrm{F}}} N_I^{\mathrm{S}}(\boldsymbol{X})\, \lambda w(\phi)\, \mathrm{d}\Omega &= 0 \end{aligned} \tag{4.47}$$

with the weak form for Lagrange multiplier

$$\int_{\Omega^{\mathrm{F}}} \delta\lambda \left(v_i^{\mathrm{F}} - v_i^{\mathrm{S}}\right) w(\phi)\, \mathrm{d}\Omega = 0 \tag{4.48}$$

The discrete mass conservation equation is

$$\int_{\Omega^{\mathrm{F}}} N_I^{\mathrm{F}} N_J^{\mathrm{F}} \rho_{J,t}^{\mathrm{F}} H(\phi)\,\mathrm{d}\Omega + \int_{\Omega^{\mathrm{F}}} N_I^{\mathrm{F}} \left(\rho^{\mathrm{F}} v_i^{\mathrm{F}}\right)_{,i} H(\phi)\,\mathrm{d}\Omega = 0 \tag{4.49}$$

which can be written as

$$M_{IJ}^{\rho} \rho_{J,t} = f_I^{\rho} \tag{4.50}$$

where

$$M_{IJ}^{\rho} = \int_{\Omega^{\mathrm{F}}} N_I^{\mathrm{F}} N_J^{\mathrm{F}} H(\phi)\,\mathrm{d}\Omega \tag{4.51}$$

$$f_I^{\rho} = \int_{\Omega^{\mathrm{F}}} N_I^{\mathrm{F}} \rho^{\mathrm{F}} \left(v_i^{\mathrm{F}}\right)_{,i} H(\phi)\,\mathrm{d}\Omega \tag{4.52}$$

where $H(\bullet)$ is the Heaviside step function. The step function in this case can be either the exact step function or a regularization.

The Lagrange multiplier field and its test function (variation) are approximated by Dirac functions on a set of points inside the structure. Let this set of points be denoted by $\boldsymbol{x}_K$, $K = 1 \,\mathrm{to}\, n_\lambda$. Then

$$\boldsymbol{\lambda} = \boldsymbol{\lambda}_K D(\boldsymbol{x} - \boldsymbol{x}_K) \quad , \quad \delta\boldsymbol{\lambda} = \delta\boldsymbol{\lambda}_K D(\boldsymbol{x} - \boldsymbol{x}_K) \tag{4.53}$$

This approximation is of course not C^0.

If we use the usual definition of internal and external nodal forces and the mass matrix, we obtain

$$\boldsymbol{M}_{IJ}^{\mathrm{F}} \dot{\boldsymbol{v}}_J^{\mathrm{F}} + \boldsymbol{f}_I^{\mathrm{intF}} - \boldsymbol{f}_I^{\mathrm{extF}} + \boldsymbol{f}_I^{\lambda\mathrm{F}} + \boldsymbol{f}_I^{\mathrm{convF}} = 0 \tag{4.54}$$

$$\boldsymbol{M}_{IJ}^{\mathrm{S}} \dot{\boldsymbol{v}}_J^{\mathrm{S}} + \boldsymbol{f}_I^{\mathrm{intS}} - \boldsymbol{f}_I^{\mathrm{extS}} + \boldsymbol{f}_I^{\lambda\mathrm{S}} = 0 \tag{4.55}$$

where

$$M_{IJ}^{\mathrm{F}} = \int_{\Omega^{\mathrm{F}}} \rho^{\mathrm{F}}\left(\boldsymbol{x},t\right) N_I^{\mathrm{F}}\left(\boldsymbol{x}\right) N_J^{\mathrm{F}}\left(\boldsymbol{x}\right) H\left(\phi\right) \mathrm{d}\Omega \tag{4.56}$$

$$M_{IJ}^{\mathrm{S}} = \int_{\Omega_0^{\mathrm{S}}} \rho_0^{\mathrm{S}}\left(\boldsymbol{X}\right) N_I^{\mathrm{S}}\left(\boldsymbol{X}\right) N_J^{\mathrm{S}}\left(\boldsymbol{X}\right) \mathrm{d}\Omega_0 \tag{4.57}$$

$$\boldsymbol{f}_I^{\mathrm{intF}} = \int_{\Omega^{\mathrm{F}}} N_{I,j}^{\mathrm{F}}\left(\boldsymbol{x}\right) \sigma_{ij}^{\mathrm{F}}\left(\boldsymbol{x},t\right) H\left(\phi\right) \mathrm{d}\Omega \tag{4.58}$$

$$\boldsymbol{f}_I^{\mathrm{extF}} = \int_{\Omega^{\mathrm{F}}} \rho^{\mathrm{F}}\left(\boldsymbol{x},t\right) N_I^{\mathrm{F}}\left(\boldsymbol{x}\right) b_i\left(\boldsymbol{x},t\right) H\left(\phi\right) \mathrm{d}\Omega + \int_{\Gamma_\tau^{\mathrm{F}}} N_I^{\mathrm{F}}\left(\boldsymbol{x}\right) \tau_i \mathrm{d}\Gamma \tag{4.59}$$

$$\boldsymbol{f}_I^{\mathrm{convF}} = \int_{\Omega^{\mathrm{F}}} N_I^{\mathrm{F}}\left(\boldsymbol{x}\right) \rho^{\mathrm{F}}\left(\boldsymbol{x},t\right) v_j^{\mathrm{F}}\left(\boldsymbol{x},t\right) v_{i,j}^{\mathrm{F}}\left(\boldsymbol{x},t\right) H\left(\phi\right) \mathrm{d}\Omega \tag{4.60}$$

$$\boldsymbol{f}_I^{\mathrm{intS}} = \int_{\Omega_0^{\mathrm{S}}} N_{I,j}^{\mathrm{S}}\left(\boldsymbol{X}\right) \sigma_{ij}^{\mathrm{S}}\left(\boldsymbol{X},t\right) \mathrm{d}\Omega \tag{4.61}$$

$$\boldsymbol{f}_I^{\mathrm{extS}} = \int_{\Omega_0^{\mathrm{S}}} \rho^{\mathrm{S}}\left(\boldsymbol{x},t\right) N_I^{\mathrm{S}}\left(\boldsymbol{x}\right) b_i\left(\boldsymbol{x},t\right) \mathrm{d}\Omega + \int_{\Gamma_\tau^{\mathrm{S}}} N_I^{\mathrm{S}}\left(\boldsymbol{x}\right) \tau_i \mathrm{d}\Gamma \tag{4.62}$$

$$\boldsymbol{f}_I^{\lambda\mathrm{F}} = \sum_K N_I^{\mathrm{F}}\left(\bar{\boldsymbol{x}}_K\right) w\left(\phi\left(\bar{\boldsymbol{x}}_K\right)\right) \lambda_K \tag{4.63}$$

$$\boldsymbol{f}_I^{\lambda\mathrm{S}} = -\sum_K N_I^{\mathrm{S}}\left(\bar{\boldsymbol{x}}_K\right) w\left(\phi\left(\bar{\boldsymbol{x}}_K\right)\right) \lambda_K \tag{4.64}$$

In addition we have the discretized constraint equation for (4.48) which are the coefficients of $\delta\lambda_K$:

$$\boldsymbol{v}_J^{\mathrm{F}} N_J^{\mathrm{F}}\left(\bar{\boldsymbol{x}}_K\right) w\left(\phi\left(\bar{\boldsymbol{x}}_K\right)\right) - \boldsymbol{v}_J^{\mathrm{S}} N_J^{\mathrm{S}}\left(\bar{\boldsymbol{x}}_K\right) w\left(\phi\left(\bar{\boldsymbol{x}}_K\right)\right) = 0 \quad \text{no sum on } K, \text{ sum on } J \tag{4.65}$$

In the above, the points $\bar{\boldsymbol{x}}_K$ are the set of points selected as interaction point. Note in equation (4.54), $\dot{\boldsymbol{v}}_J^{\mathrm{F}} = \frac{\partial \boldsymbol{v}_J^{\mathrm{F}}(\boldsymbol{x},t)}{\partial t}$ and the convection force appears. Compared to the mass matrix (3.71) on page 64 which changes with time, (4.57) is constant.

The nodal forces $\boldsymbol{f}_I^{\lambda\mathrm{S}}$ and $\boldsymbol{f}_I^{\lambda\mathrm{F}}$ are the fluid-structure interaction force. While the forces appear somewhat different, the total forces on the interfaces are equal and opposite, in

agreement with momentum balance. This is shown as follows. From the weak form (4.36) and the property of the Dirac delta function (4.34), we can get

$$\begin{aligned} 0 \;=\; & \int_{\Gamma_\tau^{\mathrm{F}}} \delta \boldsymbol{v}^{\mathrm{F}} \cdot \boldsymbol{\tau}^{\mathrm{F}} \mathrm{d}\Gamma - \int_{\Omega^{\mathrm{F}}} \delta \boldsymbol{v}^{\mathrm{F}} \cdot \left(\nabla \cdot \boldsymbol{\sigma}^{\mathrm{F}}\right) H(\phi)\, \mathrm{d}\Omega - \int_{\Omega^{\mathrm{F}}} \delta \boldsymbol{v}^{\mathrm{F}} \cdot \rho^{\mathrm{F}} \left(\dot{\boldsymbol{v}}^{\mathrm{F}} - \boldsymbol{b}\right) H(\phi)\, \mathrm{d}\Omega \\ & + \int_{\Gamma_\tau^{\mathrm{S}}} \delta \boldsymbol{v}^{\mathrm{S}} \cdot \boldsymbol{\tau}^{\mathrm{S}} \mathrm{d}\Gamma - \int_{\Omega^{\mathrm{S}}} \delta \boldsymbol{v}^{\mathrm{S}} \cdot \left(\nabla \cdot \boldsymbol{\sigma}^{\mathrm{S}}\right) \mathrm{d}\Omega - \int_{\Omega^{\mathrm{S}}} \delta \boldsymbol{v}^{\mathrm{S}} \cdot \rho^{\mathrm{S}} \left(\dot{\boldsymbol{v}}^{\mathrm{S}} - \boldsymbol{b}\right) \mathrm{d}\Omega \\ & + \int_{\Gamma^{\mathrm{I}}} \delta \boldsymbol{v}^{\mathrm{F}} \cdot \boldsymbol{\sigma}^{\mathrm{F}} \cdot \boldsymbol{n}^{\mathrm{F}} \mathrm{d}\Gamma + \int_{\Gamma^{\mathrm{I}}} \delta \boldsymbol{v}^{\mathrm{S}} \cdot \boldsymbol{\sigma}^{\mathrm{S}} \cdot \boldsymbol{n}^{\mathrm{S}} \mathrm{d}\Gamma \\ & + \int_{\Gamma^{\mathrm{I}}} \delta \boldsymbol{\lambda} \cdot \left(\boldsymbol{v}^{\mathrm{F}} - \boldsymbol{v}^{\mathrm{S}}\right) \mathrm{d}\Gamma + \int_{\Gamma^{\mathrm{I}}} \boldsymbol{\lambda} \cdot \left(\delta \boldsymbol{v}^{\mathrm{F}} - \delta \boldsymbol{v}^{\mathrm{S}}\right) \mathrm{d}\Gamma \end{aligned} \tag{4.66}$$

Note the last 4 integrations reflect the coupling on the interface. Since $\delta \boldsymbol{v}^{\mathrm{F}}$ and $\delta \boldsymbol{v}^{\mathrm{S}}$ are arbitrary on the interface, we have

$$\boldsymbol{\sigma}^{\mathrm{F}} \cdot \boldsymbol{n}^{\mathrm{F}} = -\boldsymbol{\lambda} \tag{4.67}$$

$$\boldsymbol{\sigma}^{\mathrm{S}} \cdot \boldsymbol{n}^{\mathrm{S}} = \boldsymbol{\lambda} \tag{4.68}$$

So

$$\boldsymbol{\sigma}^{\mathrm{F}} \cdot \boldsymbol{n}^{\mathrm{F}} = -\boldsymbol{\sigma}^{\mathrm{S}} \cdot \boldsymbol{n}^{\mathrm{S}} \tag{4.69}$$

Considering $\delta \boldsymbol{\lambda}$ is also arbitrary on the interface, we have

$$\int_{\Gamma^{\mathrm{I}}} \delta \boldsymbol{\lambda} \cdot \left(\boldsymbol{v}^{\mathrm{F}} - \boldsymbol{v}^{\mathrm{S}}\right) \mathrm{d}\Gamma = \int_{\Omega^{\mathrm{F}}} D(\phi)\, \delta \boldsymbol{\lambda} \cdot \left(\boldsymbol{v}^{\mathrm{F}} - \boldsymbol{v}^{\mathrm{S}}\right) \mathrm{d}\Omega = 0 \tag{4.70}$$

If we regularize the Dirac delta function as $w(\phi)$, we obtain

$$\int_{\Omega^{\mathrm{F}}} w(\phi)\, \delta \boldsymbol{\lambda} \cdot \left(\boldsymbol{v}^{\mathrm{F}} - \boldsymbol{v}^{\mathrm{S}}\right) \mathrm{d}\Omega = 0 \tag{4.71}$$

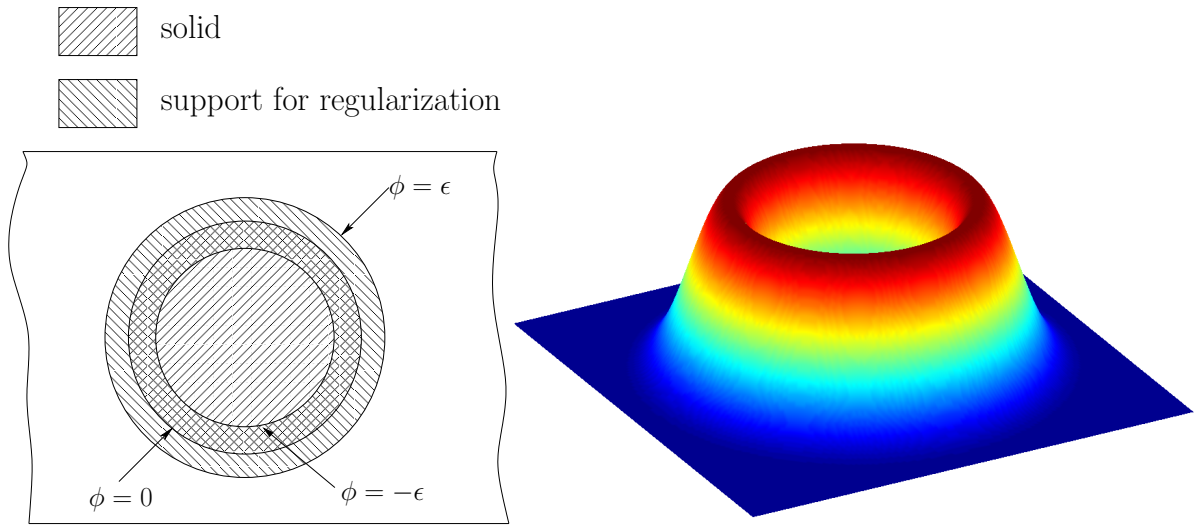

(a) Support of regularized Dirac delta function.

(b) A 3D depiction of regularized Dirac delta function.

Figure 4.3. Regularized Dirac delta function.

Substituting 4.43 and 4.44 and considering the Lagrange multiplier discretization 4.53, we obtain

$$\sum_K N_I^{\mathrm{F}}\left(\bar{\boldsymbol{x}}_K\right) w\left(\phi\left(\bar{\boldsymbol{x}}_K\right)\right) \lambda_K = \sum_K N_I^{\mathrm{S}}\left(\bar{\boldsymbol{x}}_K\right) w\left(\phi\left(\bar{\boldsymbol{x}}_K\right)\right) \lambda_K \tag{4.72}$$

Note that since we decrease monotonically with ϕ, the interaction forces tend to decrease with the distance of the interaction point from the interface. For fluid and structural nodes that are not on the interface, this tendency diminishes somewhat because the shape function for those nodes increases as we move away from the interface. Notice that the interaction forces are applied only at points within a specified distance of the fluid-structure interface, namely the support of the regularized Dirac delta function. The support depends on which of the regularizations. For example, the support and the regularized Dirac delta function for a symmetric regularization (see Figure 4.2(a)) are shown in Figure 4.3 for a cylinder in a fluid.

4.3.1. Updating

Forward-Euler scheme is employed for updating. To ensure equation (3.40), Backward-Euler is exerted for the interaction forces (4.63), (4.64) and the constraint equation (4.65) (refer to (4.48)). The momentum equation system is

$$\begin{pmatrix} \mathbf{0} & \mathbf{0} & -\Delta t\, \boldsymbol{M}^{\mathrm{F}\lambda} \\ \mathbf{0} & \mathbf{0} & \Delta t\, \boldsymbol{M}^{\mathrm{S}\lambda} \\ -\Delta t\, \boldsymbol{M}^{\lambda\mathrm{F}} & \Delta t\, \boldsymbol{M}^{\lambda\mathrm{S}} & \mathbf{0} \end{pmatrix} \begin{pmatrix} \boldsymbol{v}^{F,n+1} \\ \boldsymbol{v}^{S,n+1} \\ \boldsymbol{\lambda} \end{pmatrix} + \begin{pmatrix} \boldsymbol{M}^{\mathrm{F}} & \mathbf{0} & \mathbf{0} \\ \mathbf{0} & \boldsymbol{M}^{\mathrm{S}} & \mathbf{0} \\ \mathbf{0} & \mathbf{0} & \mathbf{0} \end{pmatrix} \begin{pmatrix} \boldsymbol{v}^{F,n+1} - \boldsymbol{v}^{F,n} \\ \boldsymbol{v}^{S,n+1} - \boldsymbol{v}^{S,n} \\ \boldsymbol{\lambda} \end{pmatrix} = \begin{pmatrix} \Delta t\, \boldsymbol{f}^{\mathrm{F}} \\ \Delta t\, \boldsymbol{f}^{\mathrm{S}} \\ \mathbf{0} \end{pmatrix} \tag{4.73}$$

where

$$\boldsymbol{f}^{\mathrm{F}} = \boldsymbol{f}^{\mathrm{extF}} - \boldsymbol{f}^{\mathrm{intF}} - \boldsymbol{f}^{\mathrm{convF}} \tag{4.74}$$

$$\boldsymbol{f}^{\mathrm{S}} = \boldsymbol{f}^{\mathrm{extF}} - \boldsymbol{f}^{\mathrm{intF}} \tag{4.75}$$

$$\boldsymbol{M}^{\mathrm{F}\lambda} = N_I^{\mathrm{F}}\left(\bar{\boldsymbol{x}}_K\right) w\left(\phi\left(\bar{\boldsymbol{x}}_K\right)\right) \quad \text{no sum on } K \tag{4.76}$$

$$\boldsymbol{M}^{\mathrm{S}\lambda} = N_I^{\mathrm{S}}\left(\bar{\boldsymbol{x}}_K\right) w\left(\phi\left(\bar{\boldsymbol{x}}_K\right)\right) \quad \text{no sum on } K \tag{4.77}$$

$$\boldsymbol{M}^{\lambda\mathrm{F}} = \left(\boldsymbol{M}^{\mathrm{F}\lambda}\right)^T \tag{4.78}$$

$$\boldsymbol{M}^{\lambda\mathrm{S}} = \left(\boldsymbol{M}^{\mathrm{S}\lambda}\right)^T \tag{4.79}$$

and Δt is the time step.

The updating procedure is

(1) Update velocities for the fluid and solid by equation (4.73).

(2) Update solid displacement and the level set for interface by equation (4.19).

(3) Update the density by (4.50).

(4) Update the pressure by (3.29).

(5) Go into next time step

4.3.2. Fluid domain integration

Since the fluid domain integrations include the function $H(\phi)$ which will cut some fluid elements into two parts, the integration should only be performed within the part which contains fluid. The adaptive quadrature is conducted to represent the curvature of the interface. If the value of the level set function for a quadrature point is greater than zero, the variables on this point should be evaluated for the integration, otherwise this quadrature point is not within fluid domain.

Figure 4.4 shows the quadrature points obtained from the adaptive quadrature method. There is only one quadrilateral element in both cases, i.e. the biggest one. The curve in each of them represents the possible zero level set which is the approximation of the interface in fluid. The small quadrilaterals show the adaptive refinements around the curve. The $*$ denote the quadrature points obtained. We refine 4 times and use 2×2 Gauss quadrature rule for quadrilaterals in Figure 4.4(a) and refine 5 times and use 1 point Gauss quadrature rule in Figure 4.4(b). It can seen that those quadrature points can be adaptively aligned along the curve. Eight refinements and 3×3 Gauss quadrature rule are used in the numerical examples for better accuracy.

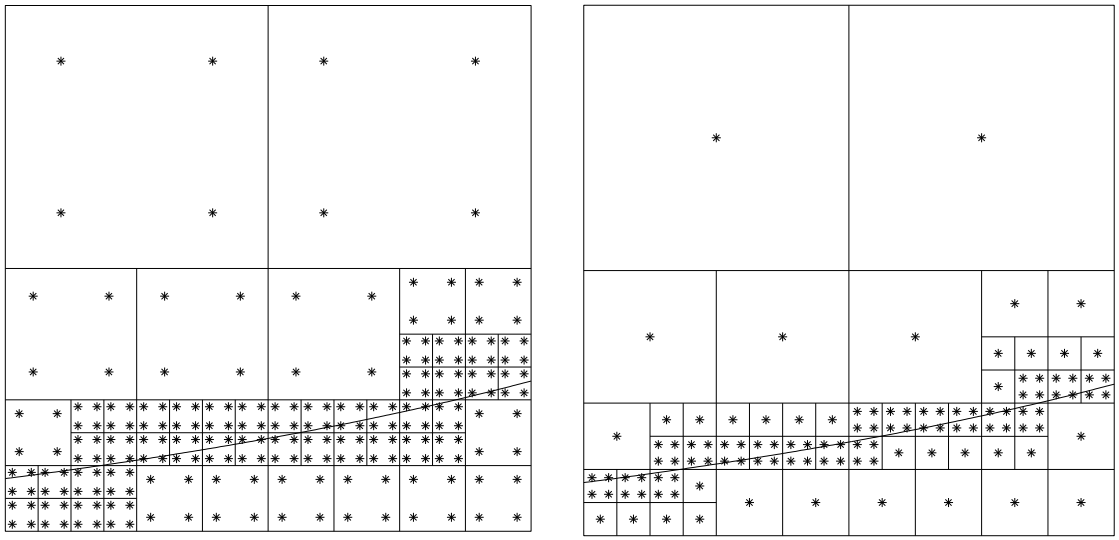

(a) Refine 4 times; 4-node quadrature rule

(b) Refine 5 times; 1-node quadrature rule

Figure 4.4. Adaptive quadrature for a fluid element

CHAPTER 5

Comparisons And Numerical Examples

5.1. SOLID OBSTACLE IN THE FLUID CHANNEL

The problem configuration is shown in Figure 5.1. We prescribe zero pressure on the right end of the fluid channel. On the left end of the fluid channel, we prescribe the pressure as shown in Figure 5.2. On the top and bottom of the fluid channel $v_y = 0$. The solid is the shaded part in Figure 5.1; the shape and the location are indicated in this figure. The bottom edge of the solid is completely fixed. The fluid is water with density $\rho_F = 1.0 \times 10^3\, kg/m^3$, bulk modulus $K_F = 2.102\, GPa$ and sound speed $c = 1450\, m/s$. The solid is an aluminum box beam with average density $\rho_S = 2.7 \times 10^3\, kg/m^3$, Young's

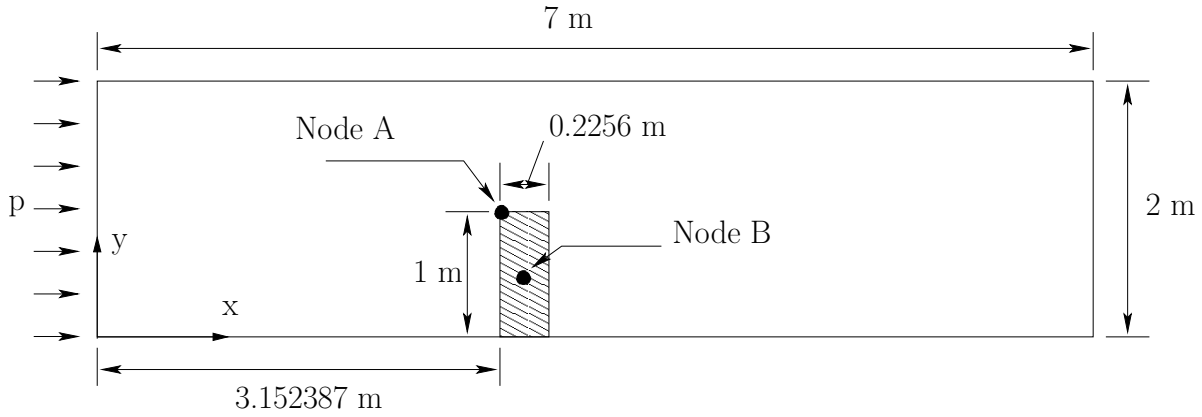

Figure 5.1. Solid obstacle in the fluid channel.

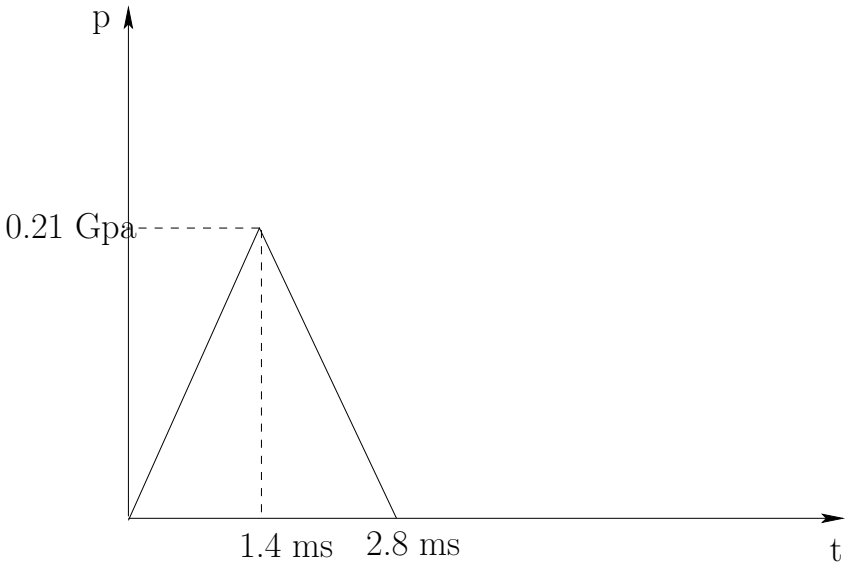

Figure 5.2. Prescribed pressure on the left end of the fluid channel for the solid obstacle problem.

modulus $E = 70\,GPa$ and Poisson ratio $\nu = 0.35$. The coordinates for points A and B are (3.152387, 1.0) and (3.265187, 0.5).

We used 3 meshes for this problem as listed in Table 5.1. Note that the meshes for the solid part of mesh m1 and mesh m2 are the same while the fluid mesh for mesh m2 is finer than mesh m1, so that we can examine the effects of the element size ratios between the solid and fluid on the results. For nodes A and B in Figure 5.1, we compare some physical variables computed by different meshes. A typical mesh m1 is shown in Figure 5.3. Note that the element edges of the meshes for the solid and the fluid are independent of each other.

Table 5.1. Meshes used for the solid obstacle problem.

	mesh m1	mesh m2	mesh m3
Total number of Elements	3923	6951	15595
Fluid number of Quadrilaterals	3379 (31×109)	6407(43×149)	13359(61×219)
Solid number of Triangles	544	544	2236
Total number of Nodes	3834	6914	14841
Fluid number of Nodes	3520	6600	13640
Solid number of Nodes	314	314	1201

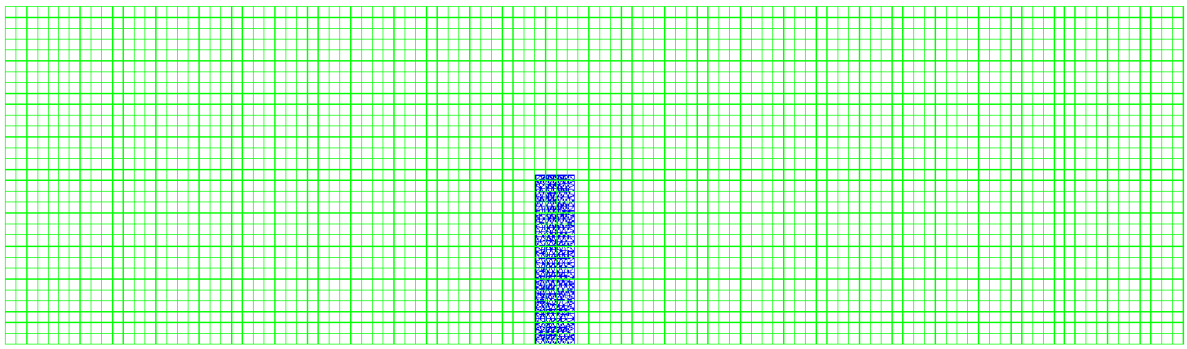

Figure 5.3. A typical mesh m1 for the solid obstacle problem.

5.1.1. Results from the immersed element method by lumped mass

The pressure contours are shown in Figure 5.4 along with the deformation of the solid. The results here are from mesh m3 with a lumped mass. At $t = 2.19\,ms$ as shown in Figure 5.4(a), we can clearly see the propagating triangular wave in the fluid channel. At $t = 3.17\,ms$ as shown in Figure 5.4(b) , we can see that the wave has propagated around the back of the solid. At $t = 4.80\,ms$ as shown in Figure 5.4(c), the free end of the solid reaches the maximum deflection. At $t = 7.00\,ms$ as shown in Figure 5.4(d), the calculation is stopped as the solid bounces back from its maximum deflection.

The fluid and solid velocities at different times around the solid are shown in Figure 5.5, Figure 5.6, and Figure 5.7. At $t = 3.46$ ms and $t = 4.51$ ms as in Figure 5.5(a) and

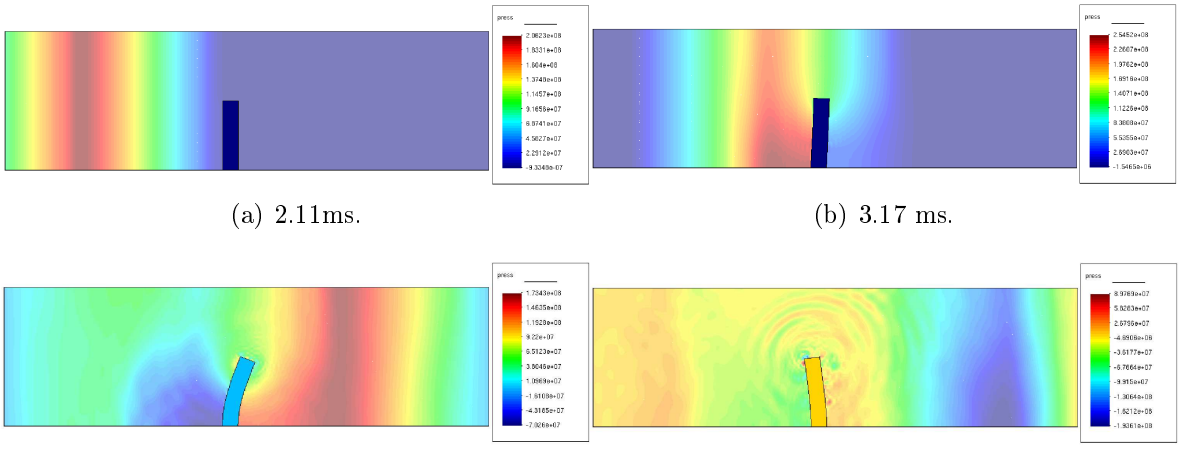

(a) 2.11ms. (b) 3.17 ms.

(c) 4.80 ms. (d) 7.00 ms.

Figure 5.4. Snapshots of pressure contours and deformations for the solid obstacle problem.

Figure 5.5(b) the fluid velocity distributions can be seen adapted to the shape of the solid and the free end of the solid gets bigger velocities and the solid bends as a beam. At $t = 4.65$ ms as in Figure 5.6(a), the solid almost reach the maximum deflection and its velocity is almost zero. At $t = 5.22$ms as in Figure 5.6(b) , since the solid is bounced back, the velocities are in the opposite directions from previous times and the fluid downstream behind the solid is dragged by the solid in the same direction. Further snapshots of the velocities are shown in Figure 5.7(a) and Figure 5.7(b)

We compare the velocity and the displacement time histories for points A and B in Figure 5.8. We can see that the different ratios of the element sizes between solid and fluid don't influence the results for the range of ratios considered. For both nodes A and B, the velocity and displacement time histories calculated by the three meshes match quite well.

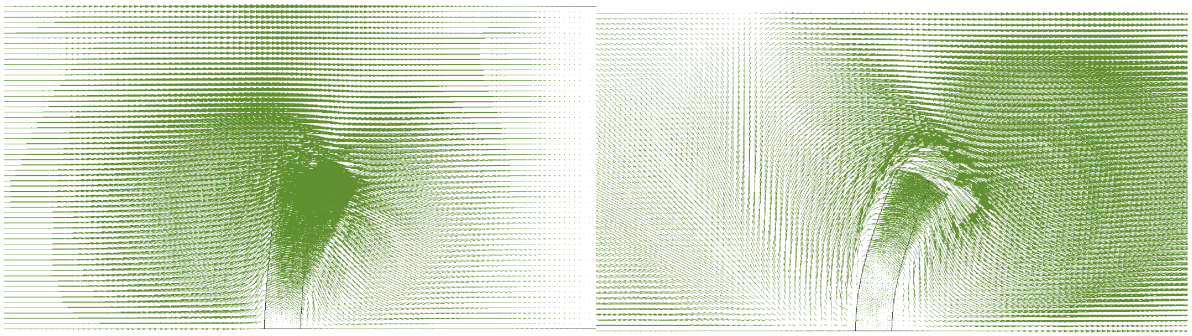

(a) 3.46 ms. (b) 4.51 ms.

Figure 5.5. Snapshots of the velocities for the fluid and solid in the solid obstacle problem.

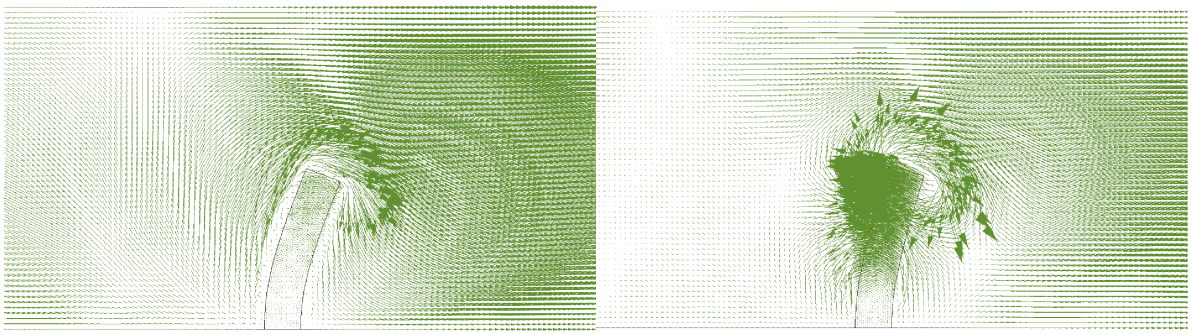

(a) 4.65 ms. (b) 5.22 ms.

Figure 5.6. Snapshots of the velocities for the fluid and solid in the solid obstacle problem.

5.1.2. Results from the immersed element method by consistent mass

As in previous section , the evolutions of the velocities and displacements for nodes A and B calculated on the 3 meshes are shown in Figures 5.9. Compared to Figures 5.8 which is obtained by the same method but with lumped mass, they are almost the same although the results from the consistent mass method show a little bit more oscillations

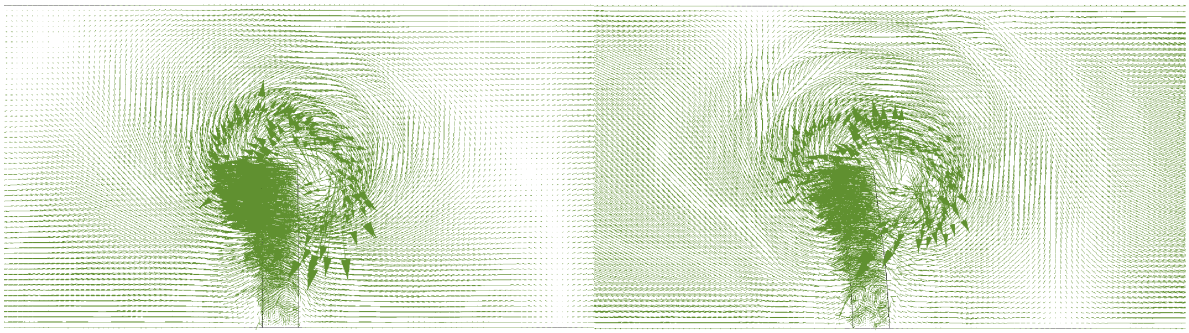

(a) 6.28 ms. (b) 7.00 ms.

Figure 5.7. Snapshots of the velocities for the fluid and solid in the solid obstacle problem.

than the results from the lumped mass method. Both results reflect the physical process quite well.

5.1.3. Results from the constraint Lagrange multiplier method

The evolution of the velocities and displacements for nodes A and B calculated on the 3 meshes are shown in Figures 5.10. Compared to Figures 5.8 and 5.9 which are obtained by the immersed element method with lumped and consistent mass, the results match each other quite well which shows the validation for both methods developed.

5.1.4. Comparisons

For the 3 methods, i.e. the immersed element lumped mass method, the immersed element consistent mass method and the Lagrange multiplier method, we compare the evolutions of the velocities and displacements for nodes A and B calculated on the same mesh m3 in Figures 5.11. From the velocities for nodes A and B, we can see that the values from the

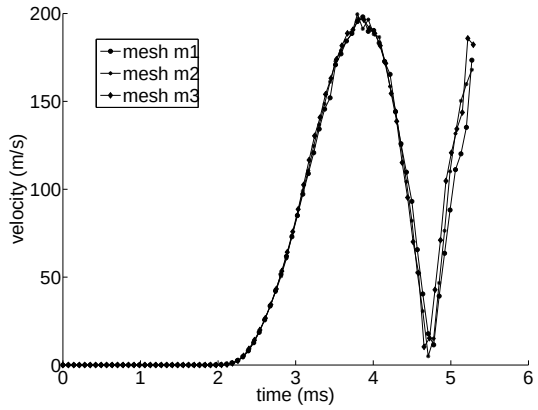

(a) Point A velocity.

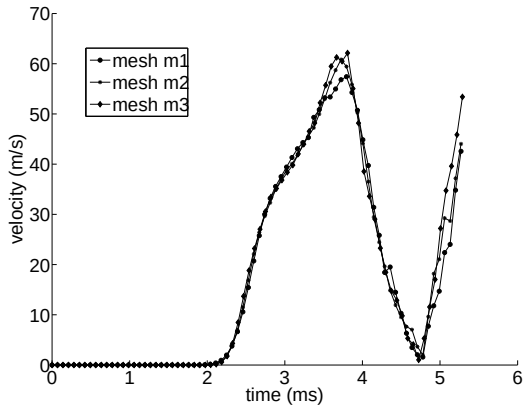

(b) Point B velocity.

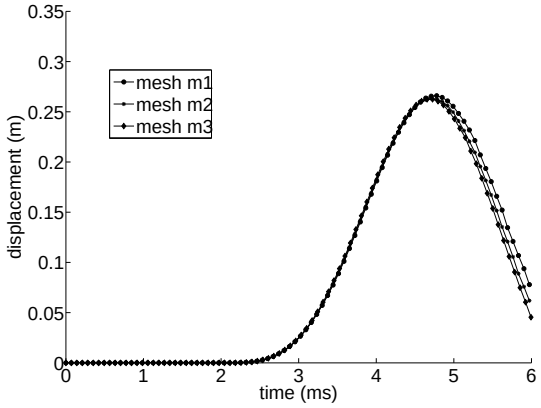

(c) Point A displacement.

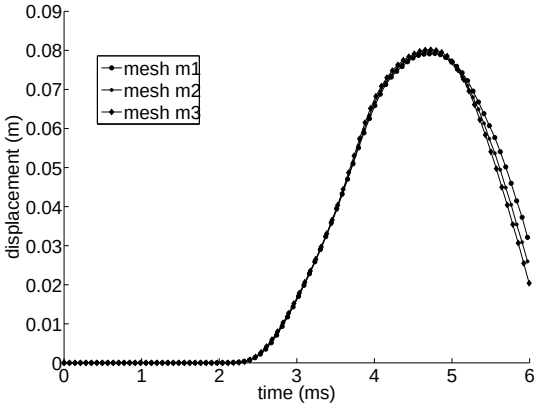

(d) Point B displacement

Figure 5.8. Velocity and displacement evolutions for nodes A and B in the solid obstacle problem by the immersed element method (lumped mass used).

Lagrange multiplier method are a little bit lower before the maximum deflection and a little bit higher after the maximum deflection than both of the immersed element methods. This is reflected in the displacements for nodes A and B. The displacement predicted by the Lagrange multiplier method before the maximum deflection is smaller while after the

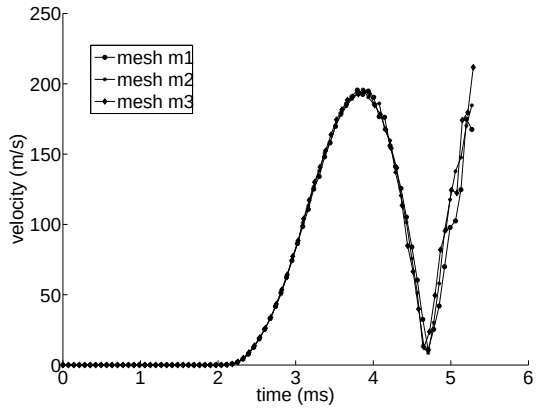

(a) Point A velocity.

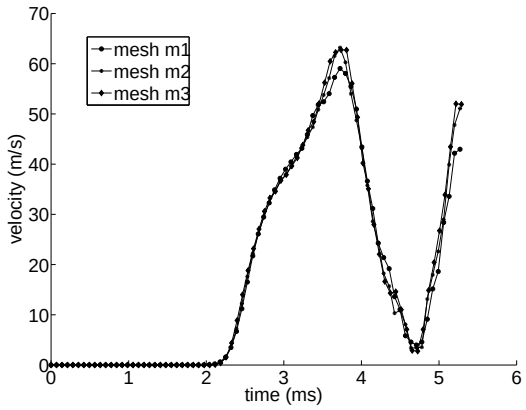

(b) Point B velocity.

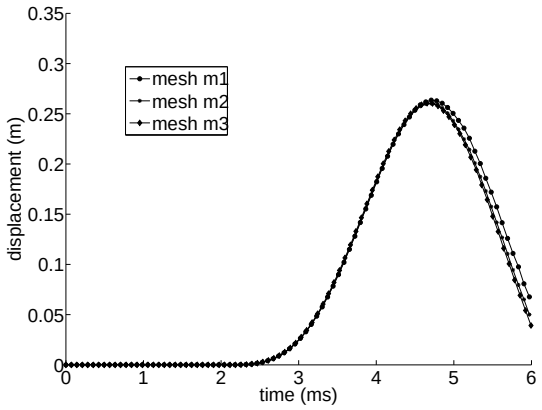

(c) Point A displacement.

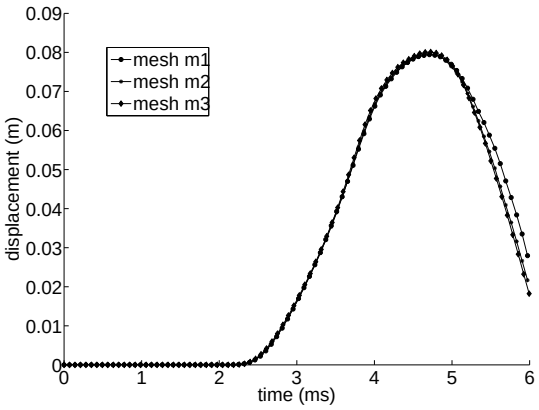

(d) Point B displacement

Figure 5.9. Velocity and displacement evolutions for nodes A and B in the solid obstacle problem by the immersed element method (consistent mass used).

maximum deflection, the displacement by the Lagrange multiplier method is larger. The Lagrange multiplier method gives a little bit more resistance for the system to change than the immersed element method.

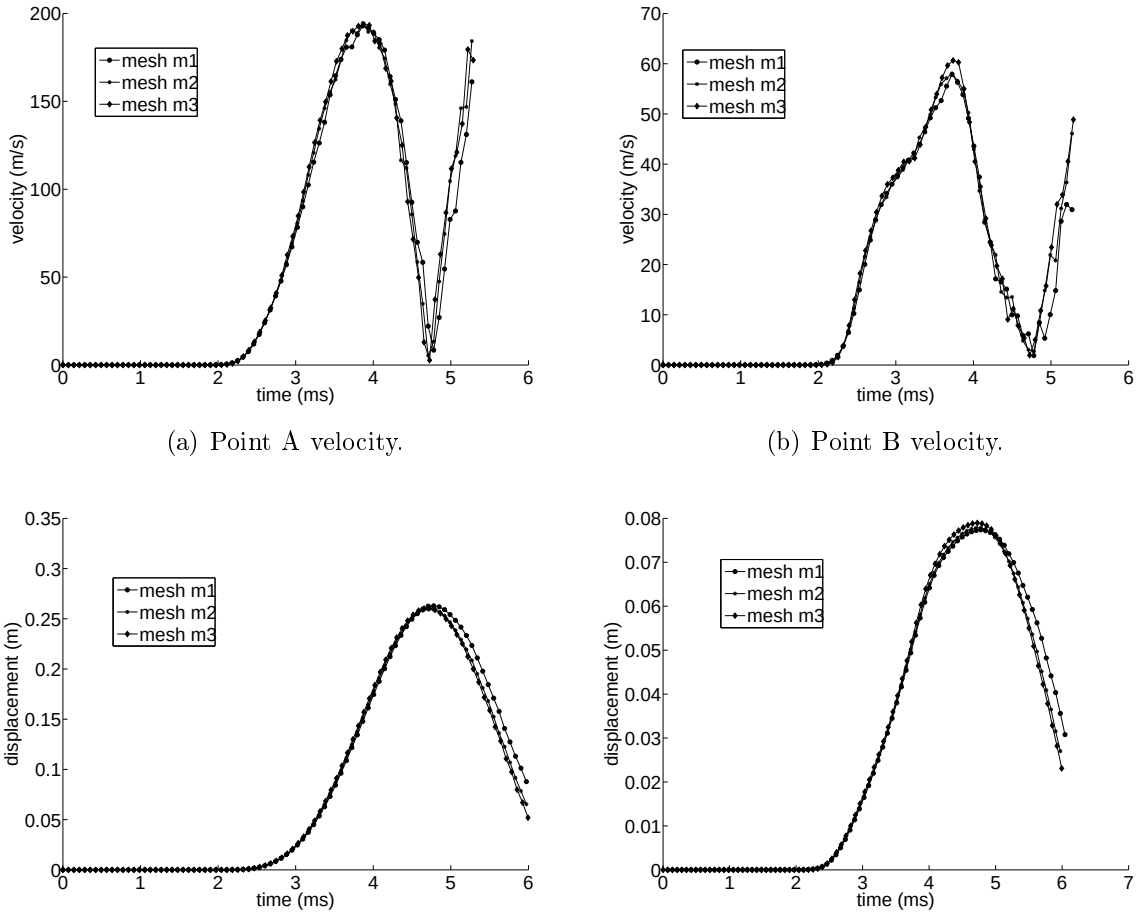

(a) Point A velocity.

(b) Point B velocity.

(c) Point A displacement.

(d) Point B displacement

Figure 5.10. Velocity and displacement evolutions for nodes A and B in the solid obstacle problem by the constraint Lagrange multiplier method.

5.2. SOFT SOLID IN THE FLUID CHANNEL

The problem setup is shown in Figure 5.12. We prescribe zero pressure on both the right and left sides of the fluid channel. On the top and bottom of the fluid channel, we fix the y component of the fluid velocity. The solid is the shaded part in Figure 5.12, the shape and the location of the solid are indicated in this figure. An impulse is applied to

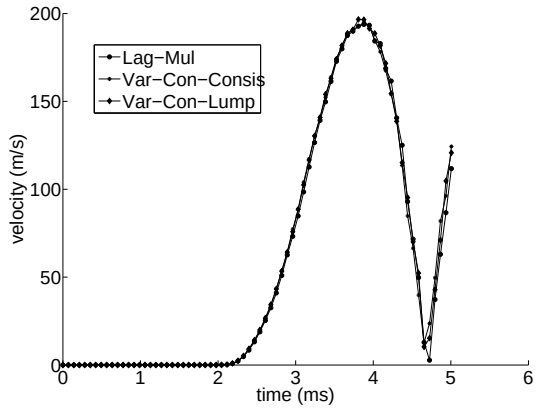

(a) Point A velocity.

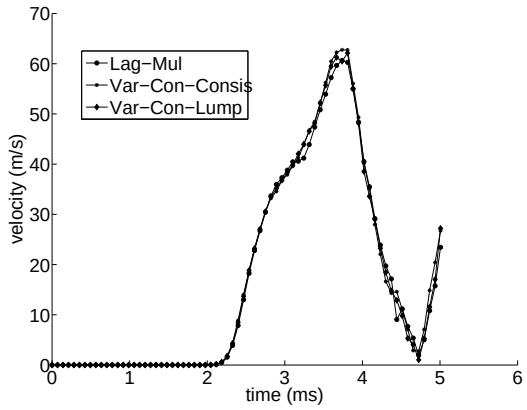

(b) Point B velocity.

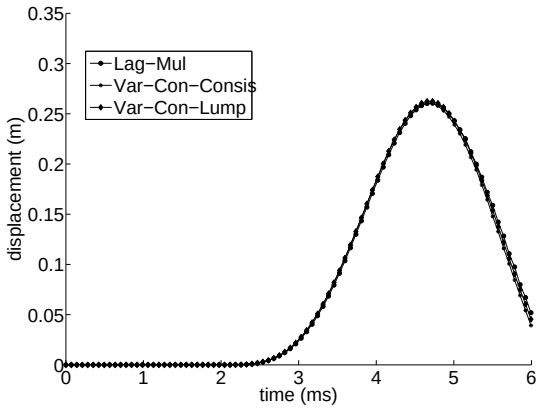

(c) Point A displacement.

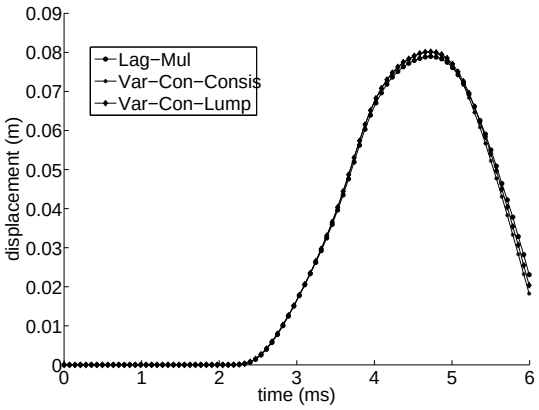

(d) Point B displacement

Figure 5.11. Comparisons of velocity and displacement time histories for nodes A and B in the solid obstacle problem by the immersed element lumped mass method (denoted as "Var-Con-Lump"), the immersed element consistent mass method (denoted as "Var-Con-Consis") and the Lagrange multiplier method (denoted as "Lag-Mul"),.

the solid by applying a force over a time interval $T = 5\Delta t$ where Δt is the initial time step in the numerical simulation. The impulse results in a velocity of the body given

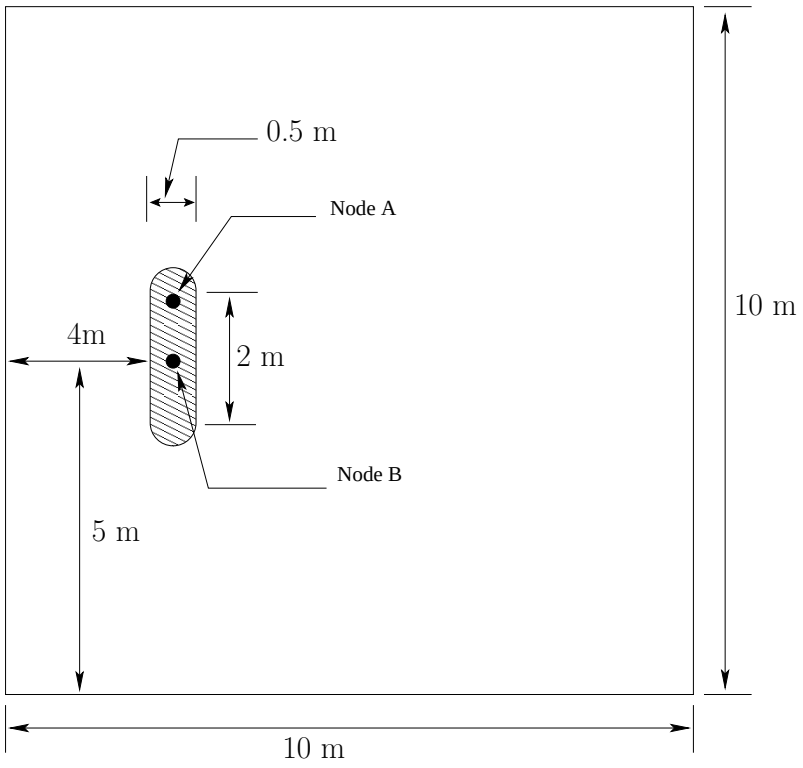

Figure 5.12. Solid floating in the fluid.

by $\int_0^T f(t)\ \mathrm{d}t = mv$, where T is the duration time for the load, $f(t)$ is the force, m is the mass of the body and v is the velocity for the body. If we assume $f(t) = kt$, we get $k = \frac{2mv}{T^2}$ and $f(t) = \frac{2mv}{T^2}t$. For this problem, we set k so that $v = 100\,m/s$. The fluid is water with density $\rho_F = 1.0 \times 10^3\ kg/m^3$, bulk modulus $K_F = 2.102\,GPa$, viscosity $\mu = 1 \times 10^{-3}\ Ns/m^2$ and sound speed $c = 1450\,m/s$. For the solid, density $\rho_S = 7.8 \times 10^3\ kg/m^3$, Young's modulus $E = 0.6\,GPa$, Poisson ratio $\nu = 0.3$. The coordinates for points A and B are (4.24015, 5.907980) and (4.237464, 5.013881).

We have two sets of meshes as shown in Table 5.2. . Here, we will also compare the results obtained by consistent mass and lumped mass.

Table 5.2. Meshes used for the floating solid problem.

	mesh ms1	mesh ms2
Total number of Elements	1137	4585
Fluid number of Quadrilaterals	961(31×31)	3721(61×61)
Solid number of Triangles	176	864
Total number of Nodes	1141	4348
Fluid number of Nodes	1024	3844
Solid number of Nodes	117	504

Several snapshots of the pressure and deformed solid are shown in Figure 5.13. The results shown here are for the lumped mass with mesh ms2. Figure 5.13(a) shows the contours of the pressure wave which reflect the shape of the solid. Figure 5.13(c) shows the fluid pressure and the solid deformation at the end of the calculation. Figure 5.13(d) shows the initial and final configurations ($t = 20.00$ ms) of the solid.

5.2.1. Comparisons between the immersed element method and the Lagrange multiplier method

Figure 5.14 shows the absolute velocity comparisons for node A and node B for the consistent and lumped mass immersed element method and the Lagrange multiplier method for mesh ms2. We emphasize that lumped mass speeds up the simulation since it doesn't need to solve a linear equation system. Figure 5.15 compares velocity for nodes A and B by the consistent mass method for meshes ms1 and ms2. Figure 5.16 compares the velocity for nodes A and B for the lumped mass method for meshes ms1 and ms2. Figure 5.17 compares the velocity for nodes A and B by the Lagrange multiplier methods for meshes ms1 and ms2. For the immersed element method, the lumped mass gives smoother results which match the skeleton of the results from the consistent mass. The Lagrange

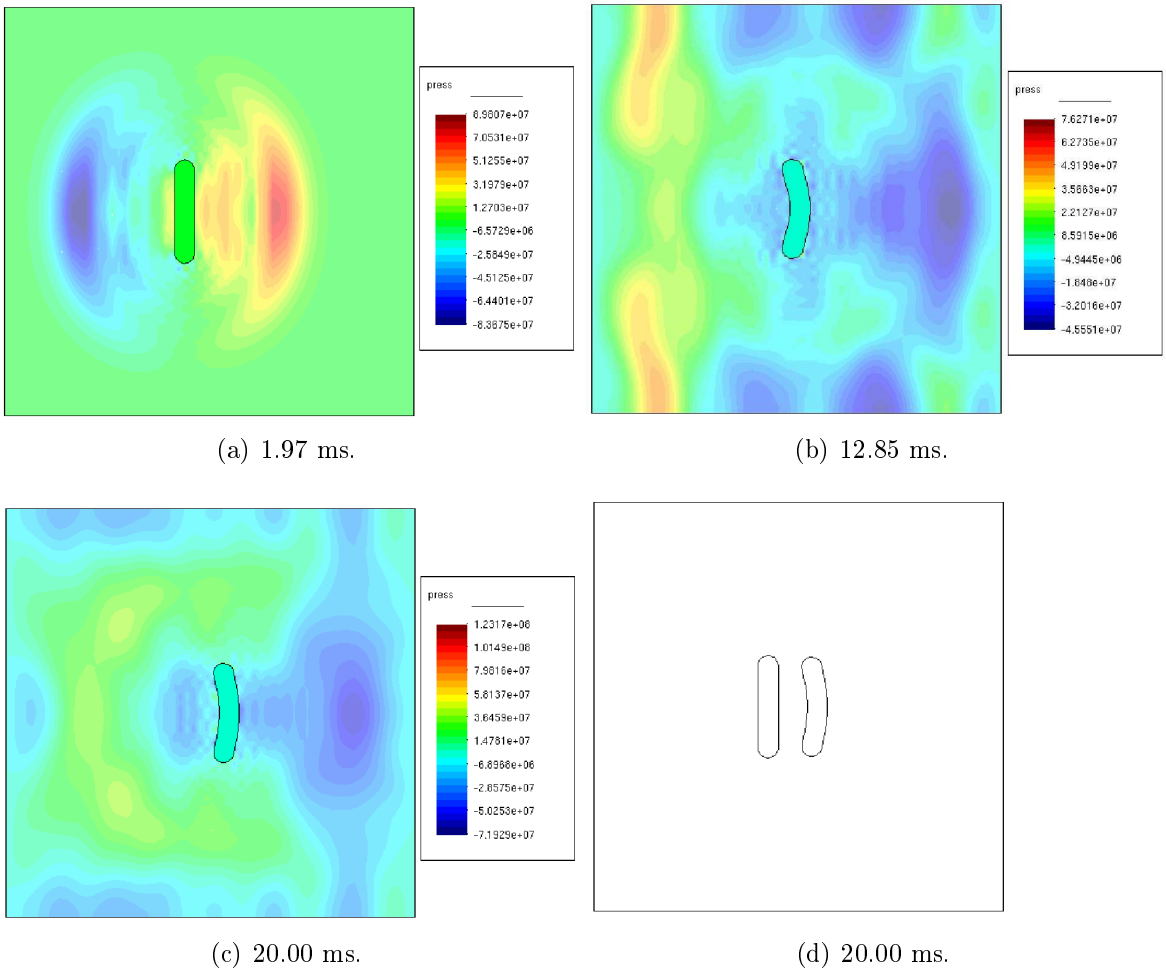

(a) 1.97 ms. (b) 12.85 ms.

(c) 20.00 ms. (d) 20.00 ms.

Figure 5.13. Snapshots of pressure and deformation for the floating solid problem.

multiplier method seems apparently oscillating much more than the results obtained from either the consistent or lumped mass immersed element method. However, We can see all results from the 3 methods here have the same trends although there are some differences in the details of the response.

5.3. FALLING BALL IN FLUID

We consider a solid ball freely dropped in a fluid as shown in Figure 5.18. We prescribe

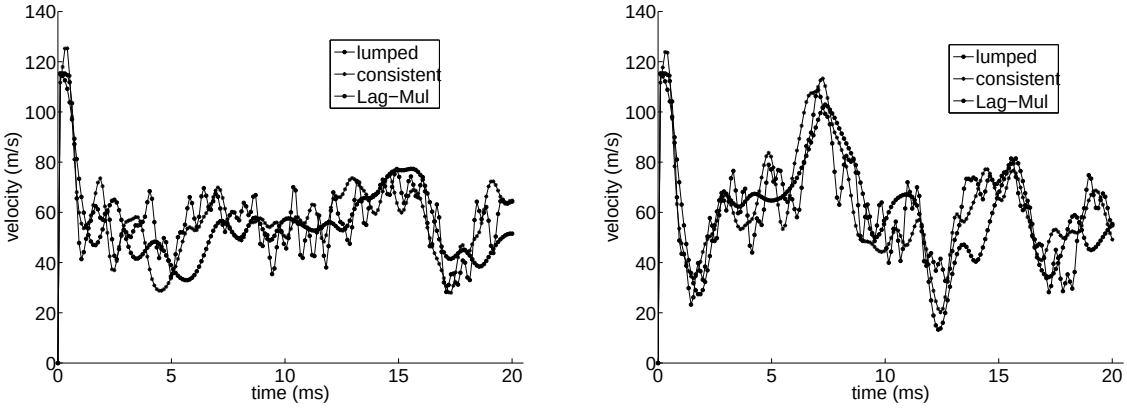

(a) Node A. (b) Node B.

Figure 5.14. Velocities of nodes A and B by mesh ms2 for the floating solid problem by the consistent and lumped mass immersed element method and the Lagrange multiplier method.

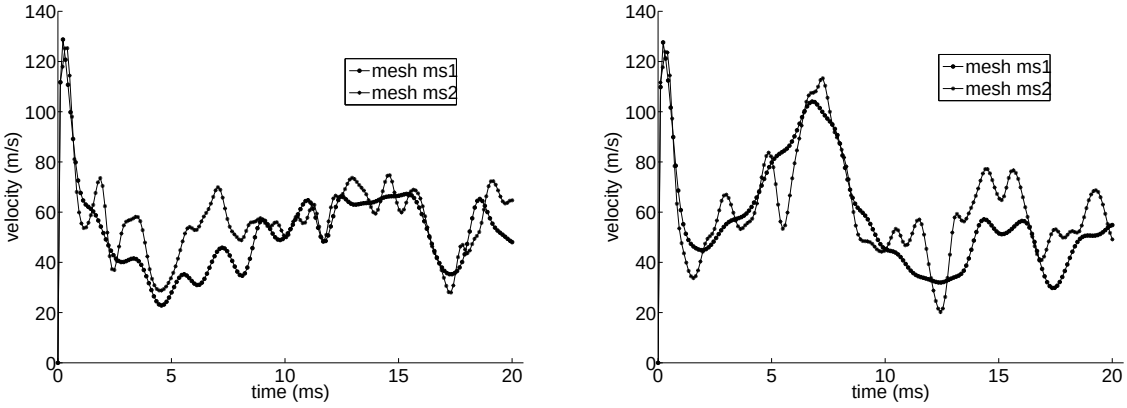

(a) Node A. (b) Node B.

Figure 5.15. Velocities of nodes A and B by the consistent mass immersed element method for meshes ms1 and ms2 for the floating solid problem.

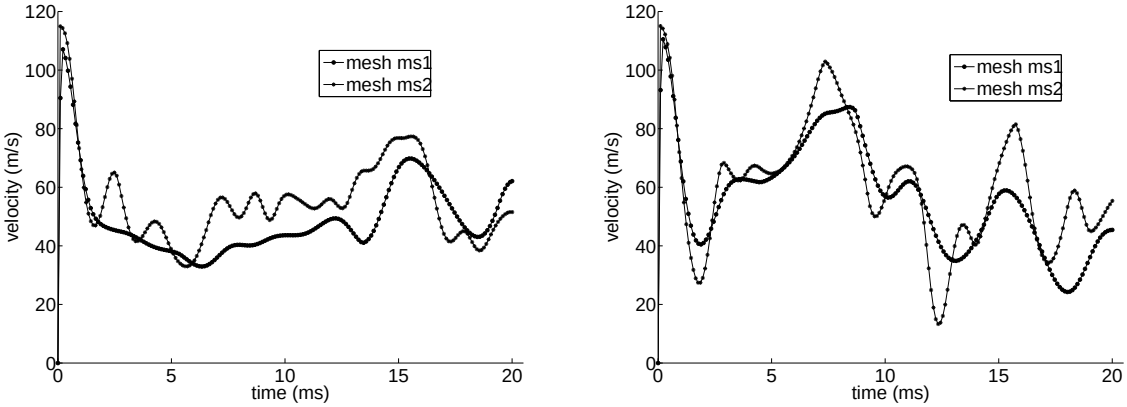

(a) Node A. (b) Node B.

Figure 5.16. Velocities of nodes A and B by lumped mass immersed element method for meshes ms1 and ms2 for the floating solid problem.

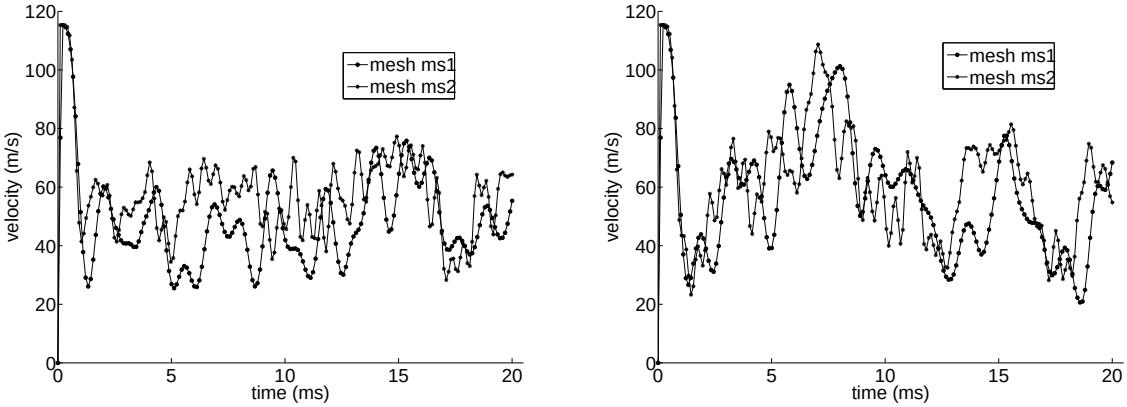

(a) Node A. (b) Node B.

Figure 5.17. Velocities of nodes A and B by the Lagrange multiplier method for meshes ms1 and ms2 for the floating solid problem.

zero pressure on the top and bottom ends of the fluid channel. On the left and right sides of the fluid channel, the x component of the fluid velocity is set to zero. The solid is the

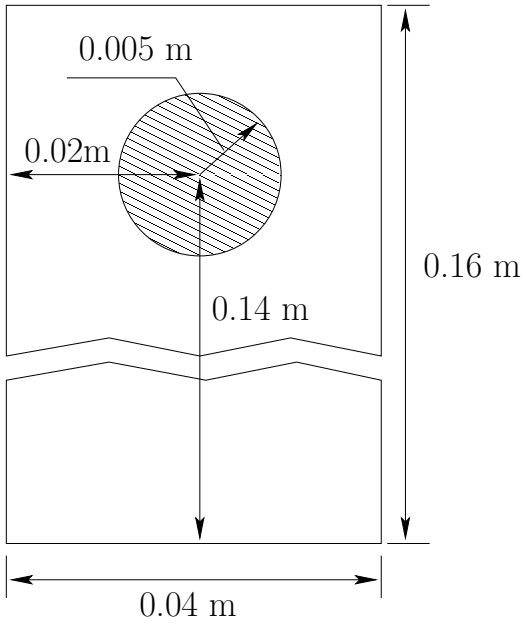

Figure 5.18. Problem setup for the freely falling ball problem.

shaded part in Figure 5.18, the shape and the location are indicated in the figure. The fluid is water with density $\rho_F = 1.0 \times 10^3 kg/m^3$, bulk modulus $K_F = 2.102 GPa$, viscosity $\mu = 0.1 Ns/m^2$ and sound speed $c = 1450 m/s$. For the solid, density $\rho_S = 2.0 \times 10^3 kg/m^3$, Young's modulus $E = 0.1\, GPa$, Poisson ratio $\nu = 0$. A gravitational force ρg with $g = 8.8\, m/s^2$ is applied to only the solid; it is not applied to the fluid so that we don't need to consider buoyancy.

The mesh is described in Table 5.3. Figure 5.19(a) shows the positions of the ball at different times while Figure 5.19(b) shows the velocity field of the fluid and the solid at the end of the calculation. We can see the vorticity forming in the fluid. Figure 5.20 shows the computed average y component of the velocity compared with the analytical terminal velocity by the lumped and consistent mass immersed element method and the

Table 5.3. Mesh used for the falling ball problem.

	mesh
Total Elements	1265
Fluid number of Quadrilaterals	1105(17×65)
Solid number of Triangles	160
Total number of Nodes	1294
Fluid number of Nodes	1188
Solid number of Nodes	106

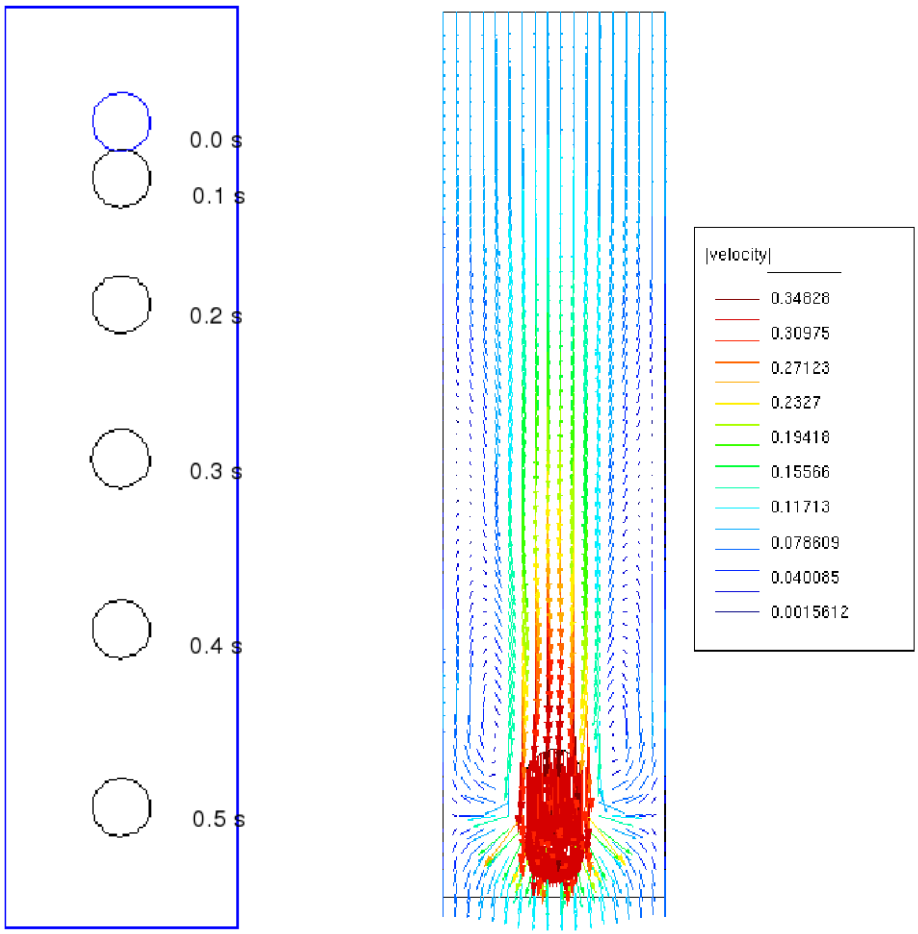

(a) Different positions at different time.

(b) Velocity at t=0.5 s.

Figure 5.19. Numerical results for the falling ball problem.

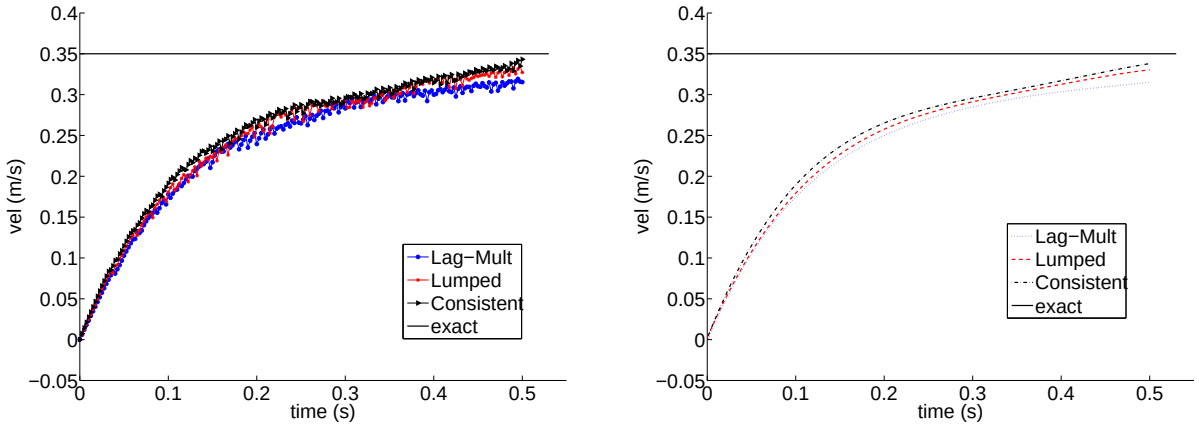

(a) Raw data.

(b) 5th order polynomial fits to data.

Figure 5.20. Velocity of falling ball; "exact" is the exact terminal velocity.

Lagrange multiplier method. The terminal velocity satisfies the formula [**92**]:

$$v = \frac{(\rho_s - \rho_f)\, g r^2}{4\mu} \left(\ln\left(\frac{L}{r}\right) - 0.9157 + 1.7244 \left(\frac{r}{L}\right)^2 - 1.7302 \left(\frac{r}{L}\right)^4 \right) = 0.35 \text{ m/s} \quad (5.1)$$

Figure 5.20(a) shows the computed data and Figure 5.20(b) shows the curve fit to the computed data by a 5th order polynomial. We can see that all the three simulations are close to the exact solution. The small oscillations in Figure 5.20(a) are probably caused by the long wavelength waves in the fluid channel since our simulation is dynamic. The result obtained from the Lagrange multiplier method is observably less than the results obtained from the other two methods.

CHAPTER 6

Conclusions

The proposed variationally consistent immersed element fluid-structure interaction method is concise in the derivation and is easy to implement. There is no need to modify the current program for fluid or solid. They are ready to use for this method. The coupling is achieved by the uniform variation. The method permits independent meshing for the fluid domain and the solid domain respectively. Eulerian description for the fluid and Lagrangian description for the solid are exerted. There is no limit on the extent of the deformation of the solid. Lumped mass can expediate the computation.

The awkward line integration in 2D and surface integration in 3D are avoided by regularization for the constraint fluid-structure interaction method which makes it easy to extend this method to 3D. This method shares the common features listed in Chapter 1 as the variationally consistent immersed element method. For Lagrange multiplier method, the system unknowns are augmented. The Lagrange multiplier entails a consistent mass for this method which may be more costly in computation than the lumped immersed element method.

From the numerical examples, we can see that both the methods produce good results. Mesh dependence is not observed. The lumped mass for the immersed element method generates as satisfactory results as the consistent mass. In the 3 examples, all the results given by the variationally consistent immersed element method and the constraint method match quite well.

APPENDIX

Solving Parent Coordinates In An Element From The Physical Coordinates For A Node

Here given a node with the coordinates $\bar{\boldsymbol{x}}$ which in 2D are $(\bar{x}, \bar{y})$, we solve its parent coordinates $\boldsymbol{\xi}$ which in 2D are (ξ, η) in an element. The procedure here is a Newton-Raphson method and it can be applied to any type of element. The mapping between the parent and physical domains is

$$\bar{\boldsymbol{x}} = N_I(\boldsymbol{\xi})\,\boldsymbol{x}_I \tag{.1}$$

where I denotes the index for the nodes of a specific element type. The dummy summation is assumed here and in the following. Then the residual is

$$\boldsymbol{r} = \bar{\boldsymbol{x}} - N_I(\boldsymbol{\xi})\,\boldsymbol{x}_I \tag{.2}$$

The Jacobian for this equation is

$$\boldsymbol{J} = \frac{\partial \boldsymbol{r}}{\partial \boldsymbol{\xi}} = N_{I,\boldsymbol{\xi}}(\boldsymbol{\xi})\,\boldsymbol{x}_I = \frac{\partial \boldsymbol{x}}{\partial \boldsymbol{\xi}} \tag{.3}$$

which in 2D is

$$\boldsymbol{J} = \begin{bmatrix} \cdots & x_I & \cdots \\ \cdots & y_I & \cdots \end{bmatrix} \begin{bmatrix} \vdots & \vdots \\ N_{I,\xi} & N_{I,\eta} \\ \vdots & \vdots \end{bmatrix} = \begin{bmatrix} \frac{\partial x}{\partial \xi} & \frac{\partial x}{\partial \eta} \\ \frac{\partial y}{\partial \xi} & \frac{\partial y}{\partial \eta} \end{bmatrix} \tag{.4}$$

which is also the Jacobian for the element relative to its parent domain. So the updating procedure finally comes out as

$$\boldsymbol{\xi}^{\nu+1} = \boldsymbol{\xi}^{\nu} - \boldsymbol{J}^{-1}\boldsymbol{r} \tag{.5}$$

until the convergence criteria is satisfied. The detailed procedure is

(1) given a node with the physical coordinates $\bar{\boldsymbol{x}}$ and an element with its local nodes $\boldsymbol{x}_I$, start from $\boldsymbol{\xi}_0$.

(2) evaluate the residual by equation (.2).

(3) evaluate the Jacobian by equation (.3).

(4) update the new parent coordinates by equation (.5).

(5) check the convergence criteria; if not satisfied, go back to step 2; if satisfied, stop.

Bibliography

[1] F.P.T. Baaijens. A fictitious domain/mortar element method for fluid-structure interaction. *International Journal for Numerical Methods in Fluids*, 35:743–761, 2001.

[2] I. Babuska, G. Caloz, and J.E. Osborn. Special finite-element methods for a class of 2nd-order elliptic problems with rough coefficients. *SIAM, Journal on Numerical Analysis*, 31(4):945–981, 1994.

[3] I. Babuska and J.M. Melenk. The partition of unity method. *International Journal for Numerical Methods in Engineering*, 40:727–758, 1997.

[4] T. Belytschko. Methods and programs for analysis of a fluid-structure systems. *Nuclear Engineering and Design*, 42:41–52, 1977.

[5] T. Belytschko. Fluid-structure interaction. *Computers and Structures*, 12:459–469, 1980.

[6] T. Belytschko and T. Black. Elastic crack growth in finite elements with minimal remeshing. *International Journal for Numerical Methods in Engineering*, 45(5):601–620, 1999.

[7] T. Belytschko, Hao Chen, Jingxiao Xu, and Goangseup Zi. Dynamic crack propagation based on loss of hyperbolicity and a new discontinuous enrichment. *International Journal for Numerical Methods in Engineering*, 58:1873–1905, 2003.

[8] T. Belytschko, W.J.T. Daniel, and G. Ventura. A monolithic smoothing-gap algorithm for contact-impact based on the signed distance function. *International Journal for Numerical Methods in Engineering*, 55:101–125, 2002.

[9] T. Belytschko and J.M. Kennedy. A fluid-structure finite element method for the analysis of reactor safty problems. *Nuclear Engineering and Design*, 38:71–81, 1976.

[10] T. Belytschko and J.M. Kennedy. Computer models for subassembly simulation. *Nuclear Engineering and Design*, 49:17–38, 1978.

[11] T. Belytschko, J.M. Kennedy, and D.F. Schoeberle. Quasi-Eulerian finite-element formulation for fluid-structure interaction. *Journal of pressure vessel technology-transactions of the ASME*, 102(1):62–69, 1980.

[12] T. Belytschko, W.K. Liu, and B. Moran. *Nonlinear Finite Elements for Continua Structures*. John Wiley & Sons, LTD, 2001.

[13] T. Belytschko, N. Moës, S. Usui, and C. Parimi. Arbitrary discontinuities in finite elements. *International Journal for Numerical Methods in Engineering*, 50(4):993–1013, 2001.

[14] T. Belytschko and R. Mullen. Stability of explicit-implicit mesh partitions in time integration. *International Journal for Numerical Methods in Engineering*, 12(10):1575–1586, 1978.

[15] T. Belytschko and R. Mullen. Two-dimensional fluid-structure impact computations with regularization. *Computer Methods in Applied Mechanics and Engineering*, 27(2):139–154, 1981.

[16] T. Belytschko, C. Parimi, N. Moës, N. Sukumar, and S. Usui. Structured extended finite element methods for solids defined by implicit surfaces. *International Journal for Numerical Methods in Engineering*, 56:609–635, 2003.

[17] T. Belytschko, S.P. Xiao, and C. Parimi. Topology optimization with implicit functions and regularization. *International Journal for Numerical Methods in Engineering*, 57:1177–1196, 2003.

[18] D.J. Benson. An efficient, accurate, simple ALE method for nonlinear finite element programs. *Computer Methods in Applied Mechanics and Engineering*, 72:305–350, 1989.

[19] H. Braess and P. Wriggers. Arbitrary Lagrangian Eulerian finite element analysis of free surface flow. *Computer Methods in Applied Mechanics and Engineering*, 190:95–106, 2000.

[20] N. Brooks and T.J.R. Hughes. Streamline upwind/Petrov-Galerkin formulation for convection dominated flows with particular emphasis on the incompressible Navier-Stokes equations. *Computer Methods in Applied Mechanics and Engineering*, 32:199–259, 1982.

[21] J.M. Carcione. A 2d chebyshev differential operator for the elastic wave equation. *Computer Methods in Applied Mechanics and Engineering*, 130:33–45, 1996.

[22] J. Chessa. *The Extended Finite Element Method for Free Surface and Two-Phase Flow Problems*. Ph.d. thesis, Northwestern University, 2003.

[23] J. Chessa and T. Belytschko. An enriched finite element method and level sets for axisymmetric two-phase flow with surface tension. *International Journal for Numerical Methods in Engineering*, 58(13):2041–2064, 2003.

[24] J. Chessa and T. Belytschko. An extended finite element method for two-phase fluids. *Journal of Applied Mechanics-Transactions of the ASME*, 70(1):10–17, 2003.

[25] J. Chessa, P. Smolinski, and T. Belytschko. The extended finite element method (XFEM) for solidification problems. *International Journal for Numerical Methods in Engineering*, 53(8):1957–1977, 2002.

[26] J. Chessa, H.W. Wang, and T. Belytschko. On the construction of blending elements for local partition of unity enriched finite elements. *International Journal for Numerical Methods in Engineering*, 57:1015–1038, 2003.

[27] D.L. Chopp and N. Sukumar. Fatigue crack propagation of multiple coplanar cracks with the coupled extended finite element/fast marching method. *International Journal of Engineering Science*, 41(8):845–869, 2003.

[28] A.J. Chorin. Numerical solutions of the Navier-Stokes equations. *Mathematics of Computation*, 22(104):745–762, 1968.

[29] Fehmi Cirak and Raúl Radovitzky. A Lagrangian-Eulerian shell-fluid coupling algorithm based on level sets. *Computers and Structures*, 83:491–498, 2005.

[30] R. Codina. A discontinuity-capturing crosswind - dissipation for the finite element solution of the convection-diffusion equation. *Computer Methods in Applied Mechanics and Engineering*, 110:325–342, 1993.

[31] R. Codina. Comparison of some finite element methods for solving the diffusion-convection-reation equation. *Computer Methods in Applied Mechanics and Engineering*, 156:185–210, 1998.

[32] R. Codina. Numerical solution of the incompressible Navier-Stokes equations with coriolis forces based on the discretization of the total time derivative. *Journal of Computational Physics*, 148:467–496, 1999.

[33] R. Codina. CBS versus GLS stabilization of the incompressible Navier-Stokes equations and the role of the time step as stabilization parameter. *Communications in Numerical Methods in Engineering*, 18:99–112, 2002.

[34] C. Daux, N. Moës, J. Dolbow, N. Sukumar, and T. Belytschko. Arbitrary branched and intersecting cracks with the extended finite element method. *International Journal for Numerical Methods in Engineering*, 48(12):1741–1760, 2000.

[35] J. Donea. A Taylor-Galerkin method for convection transport problems. *International Journal for Numerical Methods in Engineering*, 20:101–119, 1984.

[36] J. Donea and A. Huerta. *Finite element methods for flow problems*. John Wiley & Sons, LTD, 2003.

[37] J. Douglas. Numerical methods for convection dominated problems based on combining the method of charasteristics with fininte elements or finite difference procedures. *SIAM Journal on Numerical Analysis*, 19:871–885, 1982.

[38] C.A. Duarte and J.T. Oden. An h-p adaptive method using clouds. *Computer Methods in Applied Mechanics and Engineering*, 139:237–262, 1996.

[39] C. Farhat, P. Geuzaine, and G. Brown. Application of a three-field nonlinear fluid-structure formulation to the prediction of the aeroelastic parameters of an f-16 fighter. *Computers and Fluids*, 32:3–29, 2003.

[40] C. Farhat, P. Geuzaine, and C. Grandmont. The discrete geometric conservation law and the nonlinear stability of ALE schemes for the solution of flow problems on moving grids. *Journal of Computational Physics*, 174:669–694, 2001.

[41] R.P. Fedkiw. Coupling an Eulerian fluid calculation to a Lagrangian solid calculation with the ghost fluid method. *Journal of Computational Physics*, 175:200–224, 2002.

[42] R.P. Fedkiw, T. Aslam, B. Merriman, and S. Osher. A nonoscillatory Eulerian approach to interfaces in multimaterial flows (the ghost fluid method). *Journal of Computational Physics*, 152:457–492, 1999.

[43] R.P. Fedkiw, A. Marquina, and B. Merriman. An isobaric fix for the overheating problem in multimaterial compressible flows. *Journal of Computational Physics*, 148:545–578, 1999.

[44] R. Glowinski, T.W. Pan, T.I. Hesla, and D.D. Joseph. A distributed Lagrange multiplier/fictitious domain method for particulate flows. *International Journal of Multiphase Flow*, 24:755–794, 1999.

[45] R. Glowinski, T.W. Pan, T.I. Hesla, D.D. Joseph, and J. Périaus. A fictitious domain approach to the direct numerical simulation of incompressible viscous flow past moving rigid bodies: Application to particular flow. *Journal of Computational Physics*, 169:363–426, 2001.

[46] R. Glowinski, T.W. Pan, and J. Périaus. Numerical simulation of a multi-store separation phenomenon: A fictitious domain approach. *Computer Methods in Applied Mechanics and Engineering*, 195:5566–5581, 2006.

[47] A. Hansbo and P. Hansbo. A finite element method for the simulation of strong and weak discontinuities in solid mechanics. *Computer Methods in Applied Mechanics and Engineering*, 193:3523–3540, 2004.

[48] J.D. Hart, F.P.T. Baaijens, G.W.M Peters, and P.J.G Schreurs. A computational fluid-structure interaction analysis of a fiber-reinforced stentless aortic valve. *Journal of Biomechanics*, 36:699–712, 2003.

[49] A. Harten. ENO schemes with subcell resolution. *Journal of Computational Physics*, 83:148–184, 1989.

[50] E.J. Holm and H.P. Langtangen. A unified element model for the injection molding process. *Computer Methods in Applied Mechanics and Engineering*, 178:413–429, 1999.

[51] H.H. Hu, N.A. Patankar, and M.Y. Zhu. Direct numerical simulations of fluid-solid systems using Arbitrary-Lagrangian-Eulerian technique. *Journal of Computational Physics*, 169, 2001.

[52] T.J.R. Hughes. Simple scheme for developing upwind finite elements. *International Journal for Numerical Methods in Engineering*, 12(9):1359–1365, 1978.

[53] T.J.R. Hughes, L.P. Franca, and G.M. Hulbert. A new finite element formulation for computational fluid dynamics : VIII. the Galerkin/least-squares method for advective-diffusive equations. *Computer Methods in Applied Mechanics and Engineering*, 73:173–189, 1989.

[54] T.J.R. Hughes and W.K. Liu. Implicit-explicit finite-elements in transient analysis-implementation and numerical examples. *Journal of Applied Mechanics-Transactions of the ASME*, 45(2):375–378, 1978.

[55] T.J.R. Hughes and W.K. Liu. Implicit-explicit finite-elements in transient analysis-stability theory. *Journal of Applied Mechanics-Transactions of the ASME*, 45(2):371–374, 1978.

[56] T.J.R. Hughes, W.K. Liu, and T.K. Zimmermann. Lagrangian-Eulerian finite element formulation for viscous flows. *Computer Methods in Applied Mechanics and Engineering*, 29:329–349, 1981.

[57] H. Ji, D.L. Chopp, and J.E. Dolbow. A hybrid extended finite element/level set method for modeling phase transformations. *International Journal for Numerical Methods in Engineering*, 54(8):1209–1233, 2001.

[58] G.E. Karniadakis and S.J. Sherwin. *Spectral/hp Element Methods for CFD*. Oxford University Press, Inc., 1999.

[59] Y. Krongauz and T. Belytschko. Efg approximation with discontinuous derivatives. *International Journal for Numerical Methods in Engineering*, 41(7):1215–1233, 1998.

[60] E. Kuhl, S. Hulshoff, and R. de Borst. An arbitrary Lagrangian Eulerian finite-element approach for fluid-structure interaction phenomena. *International Journal for Numerical Methods in Engineering*, 57:117–142, 2003.

[61] A. Legay, J. Chessa, and T. Belytschko. An Eulerian-Lagrangian method for fluid-structure interaction based on level sets. *Computer Methods in Applied Mechanics and Engineering*, 195:2070–2087, 2006.

[62] A. Legay, H.W. Wang, and T. Belytschko. Strong and weak arbitrary discontinuities in spectral finite element. *International Journal for Numerical Methods in Engineering*, 64:991–1008, 2005.

[63] P. LeTallec and J. Mouro. Fluid structure interaction with large structural displacements. *Computer Methods in Applied Mechanics and Engineering*, 190:3039–3067, 2001.

[64] W.K. Liu and T. Belytschko. Mixed-time implicit-explicit finite-elements for transient analysis. *Computers and Structures*, 15(4):445–450, 1982.

[65] W.K. Liu, D.W. Kim, and S. Tang. Mathematical foundations of the immersed finite element method. *Computational Mechanics*, 39(3):211–222, 2005.

[66] R. Löhner, K. Morgan, and O.C. Zienkiewicz. The solution of non-linear hyperbolic equations system by the finite element method. *International Journal for Numerical Methods in Fluids*, 4:1043–1063, 1984.

[67] L.G. Margolin. Introduction to "An Arbitrary Lagrangian-Eulerian Computing Method for All Flow Speeds. *Journal of Computational Physics*, 135:198–202, 1997.

[68] J.M. Melenk and I. Babuska. The partition of unity finite element method: Basic theory and applications. *Computer Methods in Applied Mechanics and Engineering*, 139:289–314, 1996.

[69] N. Moës, J. Dolbow, and T. Belytschko. A finite element method for crack growth without remeshing. *International Journal for Numerical Methods in Engineering*, 46(1):131–150, 1999.

[70] W. Mulder, S. Osher, and J.A. Sethian. Computing interface motion in compressbile gas dynamics. *Journal of Computational Physics*, 100:209–228, 1992.

[71] P. Nithiarasu, O.C. Zienkiewicz, B.V.K. Satya Sai, K. Morgan, R. Codina, and M. Vázquez. Shock capturing viscosities for the general fluid mechanics algorithm. *International Journal for Numerical Methods in Fluids*, 28:1325–1353, 1998.

[72] J. Nitsche. über ein Variationsprinzip zur Lösung von Dirichlet -Problemen bei Verwendung von Teilräumen, die keinen Randbedingungen unterworfen sind. *Abhandungin aus dem Mathematischen Seminar der Universitat Hamburg*, 36:9–15, 1970.

[73] T. Nomura and T.J.R. Hughes. An arbitrary Lagrangian-Eulerian finite element method for interaction of fluid and a rigid body. *Computer Methods in Applied Mechanics and Engineering*, 95:115–138, 1992.

[74] K.C. Park, C.A. Felippa, and R. Ohayon. Partitioned formulation of internal fluid structure interaction problems by localized Lagrange multipliers. *Computer Methods in Applied Mechanics and Engineering*, 190:2989–3007, 2001.

[75] N.A. Patankar, P. Singh, D.D. Joseph, R. Glowinski, and T.W. Pan. A new formulation of the distributed Lagrange multiplier/fictitious domain method for particulate flows. *International Journal of Multiphase Flow*, 26:1509–1524, 2000.

[76] A.T. Patera. A spectral method for fluid dynamics: Laminar flow in a channel expansion. *Journal of Computational Physics*, 54:468–488, 1984.

[77] C.S. Peskin. Numerical analysis of blood flow in the heart. *Journal of Computational Physics*, 25:220–252, 1977.

[78] C.S. Peskin. The immersed boundary method. In *Acta Numerica*, volume 11, pages 479–517. Cambridge University Press, 2002.

[79] O. Pironneau. On the transport-diffusion algorithm and its application to the Navier-Stokes equations. *Numerische Mathematik*, 38:309–332, 1982.

[80] R. Radovitzky and M. Ortiz. Lagrangian finite element analysis of Newtonian fluid flows. *International Journal for Numerical Methods in Fluids*, 28:1325–1353, 1998.

[81] J.A. Sethian. *Level Set Methods and Fast Marching Methods: Evolving Interfaces Computational Geometry, Fluid Mechanics, Computer Vision, and Materials Science*. Cambridge University Press, 1999.

[82] C.W. Shu. Numerical experiments on the accuracy of ENO and modified ENO schemes. *J. Sci. Computations*, 5:127–149, 1990.

[83] M. Souli, A. Ouahsine, and L. Lewin. ALE formulation for fluid-structure interaction problems. *Computer Methods in Applied Mechanics and Engineering*, 190:659–675, 2000.

[84] M. Stolarska, D.L. Chopp, N. Moës, and T. Belytschko. Modelling crack growth by level sets in the extended finite element method. *International Journal for Numerical Methods in Engineering*, 51(8):943–960, 2001.

[85] N. Sukumar, D.L. Chopp, N. Moës, and T. Belytschko. Modeling holes and inclusions by level sets in the extended finite-element method. *Computer Methods in Applied Mechanics and Engineering*, 190:6183–6200, 2001.

[86] N. Sukumar, N. Moës, B. Moran, and T. Belytschko. extended finite element method for three-dimensional crakc modelling. *International Journal for Numerical Methods in Engineering*, 48:1549–1570, 2000.

[87] M. Sussman, P. Smereka, and S. Osher. A level set approach for computing solutions to incompressible two-phase flow. *Journal of Computational Physics*, 114:146–159, 1994.

[88] D. Tam, Raúl Radovitzky, and R. Samtaney. An algorithm for modelling the interaction of a flexible rod with a two-dimensional high-speed flow. *International Journal for Numerical Methods in Engineering*, 64:1057–1077, 2005.

[89] B.L. Vaughan, B.G. Smith, and D.L. Chopp. A comparison of the extended finite element method with the immersed interface method for elliptic equations with discontinuous coefficients and singular sources. *Communications in Applied Mathematics and Computational Science*, 1(1):207–228, 2006.

[90] G. Ventura, B. Moran, and T. Belytschko. Dislocations by partition of unity. *International Journal for Numerical Methods in Engineering*, 62:1463–1487, 2005.

[91] G.J. Wagner, N. Moës, W.K. Liu, and T. Belytschko. The extended finite element method for rigid particles in Stokes flow. *International Journal for Numerical Methods in Engineering*, 51:293–313, 2001.

[92] X. Wang and W.K. Liu. Extended immersed boundary method using FEM and RKPM. *Computer Methods in Applied Mechanics and Engineering*, 193:1305–1321, 2004.

[93] B.I. Wohlmuth. *Discretization Methods and Iterative Solvers Based on Domain Decomposition*. Springer, 2001.

[94] L. Zhang. *Multi-scale analysis on fluid and fluid-structure interactions using meshfree and finite element methods*. Ph.d. thesis, Northwestern University, 2003.

[95] L. Zhang, A. Gerstenberger, X. Wang, and W.K. Liu. Immersed finite element method. *Computer Methods in Applied Mechanics and Engineering*, 193:2051–2067, 2004.

[96] Q. Zhang and T. Hisada. Studies of the strong coupling and weak coupling methods in FSI analysis. *International Journal for Numerical Methods in Engineering*, 60:2013–2029, 2004.

[97] O.C. Zienkiewicz and R. Codina. A general algorithm for compressible and incompressible flow - part I. the split, characteristic-based sheme. *International Journal for Numerical Methods in Fluids*, 20:869–885, 1995.

[98] O.C. Zienkiewicz, K. Morgan, B.V.K. Satya Sai, R. Codina, and M. Vázquez. A general algorithm for compressible and incompressible flow - part II. tests on the explicit form. *International Journal for Numerical Methods in Fluids*, 20:887–913, 1995.